

UC Riverside

UC Riverside Electronic Theses and Dissertations

Title

Electrical Properties of Trilayer Graphene

Permalink

<https://escholarship.org/uc/item/7td1v4m6>

Author

Lee, Yongjin

Publication Date

2014

Peer reviewed|Thesis/dissertation

UNIVERSITY OF CALIFORNIA
RIVERSIDE

Electrical Properties of Trilayer Graphene

A Dissertation submitted in partial satisfaction
of the requirements for the degree of

Doctor of Philosophy

in

Physics

by

Yong Jin Lee

December 2014

Dissertation Committee:

Dr. Chun Ning(Jeanie) Lau, Chairperson

Dr. Jing Shi

Dr. Nathaniel Gabor

Copyright by
Yong Jin Lee
2014

The Dissertation of Yong Jin Lee is approved:

Committee Chairperson

University of California, Riverside

Acknowledgement

Pursuing my graduate studies in the Jeanie Lau group gave me a great opportunity to explore the unraveling physical phenomena at the nano-systems to be under the talented professors and my colleagues. First and foremost, I feel indebted to my advisor Professor Chun Ning (Jeanie) Lau for the unbounded patience and kindness in regard to this dissertation. I would like to express my gratitude to her for successfully mentoring me through my graduate studies with her great scientific insight, propitious assistance and devoted support. Here I would also thank the members of my defense and candidacy exam committees, Prof. Marc Bockrath, Prof. Jing Shi, Prof. Nathaniel Gabor and Prof. Shan Wei Tsai for their interest and precious time.

I would also like to thank my former group members and current group members. I benefited tremendously from the previous work of setting up the lab, equipments and development of fabrication recipes by Jairo Velasco Jr, Wenzhong Bao, Hang Zhang, Lei Jing and Zheng Zhao. I especially want to acknowledge Jairo Velasco Jr. who taught me fabrication and measurements. His passion and great leadership lead to my growth as a hard working graduate student. I also want to acknowledge David tran and Kevin Myhro and thank them for their help with my trilayer projects. Because of their enthusiastic work and friendly disposition, we produced a lot of good works together in the lab and NHMFL. I would also like to thanks all current group memebers: Fenglin Wang, Jhao-wun Huang, Yanmeng Shi, Nathaniel Gillgren, Petr Stepanov, Shi Che and Son tran. Their passion and hard work make this group stronger, enjoyable and stimulating.

Because of their collaborating work, we produced a lot of nice results as discussed in my thesis; Proc SPIE 8725 and Solid state comm 2012 152:1301-1305 in chapter 4, *Nano Lett* 2013, 13:1627-1631 in chapter 5, *Nature Comm.* 2014,5 5656 in chapter 6 and *Nature Comm.* 2014,5 4550 and *Nano Letters* 2014, 14:1324-1328 in chapter 8 are used.

I acknowledge Professor Allan Macdonald, Dr Yafis Balars, Dr. Fan Zhang and Dr. Jeil Jung for their theoretical support on the trilayer projects during my graduate life. I especially want to acknowledge Dr. Dmitry Smirnov and Dr Juhyun Park at the National High Magnetic Field Laboratory in Tallahassee for their valuable assistance during my trips there. Their advice about operating cryostats enabled me to successfully perform the high field measurement.

I thank my first year house mates, Mike Beaumier, Chris Heidt, Patrick Odenthal, and Behnam Darvish for their friendship, which taught English as well as America culture. I especially thank my close church friends; Pastor Lee Heungrok, John Park, Younghoon, Bada and East-Sarang church small group members.

Lastly and most importantly, I am grateful to all my family members for their constant support and love through my entire life. Especially I would like to thank my wife, JungSun Lee for full support and prayer on my research work, and for her love. Thank God and I hope my aim of research is only for God's grace.

ABSTRACT OF THE DISSERTATION

Electrical Properties of Trilayer Graphene

by

Yong Jin Lee

Doctor of Philosophy, Graduate Program in Physics
University of California, Riverside, December 2014
Dr. Chun Ning(Jeanie) Lau, Chairperson

Graphene is a two-dimensional (2D) honeycomb lattice of carbon atoms. Since its experimental isolation in 2004, this 2D system has become an important platform for condensed matter research. For few-layer graphene, the band structures differ dramatically with each additional layer, and with different stacking orders. In this dissertation, we present comprehensive transport studies on dual-gated trilayer graphene, where the relative strengths of single particle physics and interaction effects are tunable via external parameters such as gate voltage and magnetic field.

Chapter 1 briefly introduces graphene electron configuration, Fermi energy and quantum Hall effect. Chapter 2 presents the band structure of single, bi-, trilayer graphene within the tight binding model, and chapter 3 describes the fabrication and annealing procedures of dual-gated suspended graphene devices.

Detailed transport studies of ABA and ABC-stacked trilayer graphene are presented in chapter 4 through chapter 8. Chapter 4 discusses the external electric effect on dual-gated bilayer and trilayer graphene. We observe a tunable band gap in bilayer graphene and a tunable band overlap in trilayer graphene. We observe an intrinsic gap in ABC trilayer graphene at the charge neutrality point, which can be partially suppressed by an electric field of either polarity, temperature and parallel magnetic field. This insulating state of ABC trilayer is identified to be layer antiferromagnet, and is described in Chapter 6. In the quantum Hall regime, symmetry-broken states at the lowest Landau level are studied as a function of magnetic field and out-of-plane electric field, and transitions between QH plateaus are observed. Different sequences and transitions are observed for ABA and ABC-stacked trilayer graphene, reflecting the different competing underlying symmetries in these systems. These results are discussed in chapter 5 and 7, respectively. Chapter 8 presents the Landau level gaps in bilayer and ABC trilayer graphene by using transport spectroscopy measurement. We find two distinct states that have two quantum units of Hall conductivity. Our results underscore insight into both single particle physics and many-body interaction in graphene and low-dimensional materials. Finally, chapter 9 concludes with a briefly summary and outlook for the field of graphene and 2D materials research.

Table of Contents

TABLE OF CONTENTS	VIII
LIST OF FIGURES	XII
LIST OF TABLES	XX
CHAPTER 1 : INTRODUCTION.....	1
1-1 : Still Carbon.....	2
1-2: 2D electron system	4
1-3: Quantum Hall effect	7
1-4: Thesis Outlines	8
Reference	11
CHAPTER 2 : TIGHT BINDING MODEL FOR MONO-, BI- AND TRILAYER GRAPHENE.....	12
2.1: Tight Binding Method	12
2.2: Tight binding model of single layer graphene	15
2.3: Tight binding model of bilayer layer graphene	20
2.4: Asymmetry gap in the band structure of bilayer graphene	24
2.5: Tight binding model of trilayer layer graphene	26
2.6: Asymmetry gap in the band structure of trilayer graphene	31
Reference	35
CHAPTER 3 : DEVICE FABRICATION.....	37
3.1: Identification of number of layers and stacking order	37
3.2: Stacking Order	39

3.3 Device Fabrication	41
3.4: Suspend Top gate and the electrode fabrication	42
3.5: Characterization of Device	48
Reference	56
CHAPTER 4 : BAND GAP AND OVERLAP IN BILAYER AND TRILAYER GRAPHENE	57
4.1: Device characterization and experimental procedure	58
4.2: Gap in bilayer graphene	59
4.3: Transport data of BLG devices at B=0T	61
4.4: Transport data of TLG devices at B=0T	63
References	65
CHAPTER 5 : QUANTUM HALL STATE IN ABA TRILAYER GRAPHENE	68
5.1: Device characterization	69
5.2: Energy band structure in ABA TLG	70
5.3: Quantum Hall state of ABA TLG in single particle picture	71
5.4: Quantum Hall state of ABA TLG in electronic interaction	74
5.5: Quantum Hall state of ABA TLG in the effect of E_z	75
Conclusion	79
Reference	80
CHAPTER 6 : THE INTRINSIC GAP IN ABC TRILAYER GRAPHENE	84
6.1: Device characterization	85
6.2: Gapped insulating state at the CNP	86
6.3: Temperature dependence of the gapped state	89

6.4: $E \perp$ and B_{\parallel} field dependence of the gapped state	91
6.5: Discussion of screening length	96
6.6: Estimation of the Antiferromagnetic Gap.....	98
6.7: Discussion and Possible Phase Diagram	101
6.8: Conclusion and outlook	104
References.....	105
CHAPTER 7 : QUANTUM HALL STATE IN ABC TRILAYER GRAPHENE ..	109
7.1: Device characterization.....	110
7.2: Quantum Hall state of ABC TLG using a single gate	111
7.3: Quantum Hall state of ABC TLG using dual gate.....	114
7.4: Discussion of crossing between symmetry broken LL and energy gap	116
7.5: Discussion of the remote hopping term γ_4 effect	120
Conclusion	121
CHAPTER 8 : SPECTROSCOPY MEASUREMENT OF LANDAU LEVEL GAPS IN BILAYER AND TRILAYER GRAPHENE	126
8.1 Spontaneous quantum Hall states	127
8.2 Realization of two distinct $\nu=\pm 2$ QH states.....	129
8.3 Transport spectroscopy technique.....	131
8.3 Characterization of the two distinct $\nu=\pm 2$ QH states.	133
8.4 Discussion of nature of two $\nu=2$ QH states.....	135
8.5 Spectroscopy measurement of ABC trilayer graphene.....	139
8.6 Conclusion	141
Reference	142

CHAPTER 9 : CONCLUSION AND OUTLOOK	147
9.1:Conclusion	147
9.2:Outlook and Future Work.....	148
Reference	151
APPENDIX A	152
Procedure to clean needle of Oxford fridge.....	152
APPENDIX B	154
Calculation of density of state and Fermi energy in single, bi- and trilayer graphene. ..	154
APPENDIX C	157
Current annealing summary table.....	157

List of Figures

Figure 1.1: Images of (a) LHC accelerator in CERN and (b) Oxford fridge in UCR (c) Production of lambda particle.....	2
Figure 1.2: Formation of the sp hybridization electron state and various dimensionality in carbon.....	3
Figure 1.3: Electron energy level diagram of a GaAs-AlGaAs heterostructure device. Image from ref ⁸	5
Figure 1.4: Two-dimensional electron gas with (a) Hall bar geometry and (b) transport data.....	8
Figure 2.1: Schematic image for wavefunctions of electrons for two hydrogen atoms. ...	13
Figure 2.2: Crystal structure of SLG and Reciprocal lattice. (a) Honeycomb carbon lattice of graphene with A and B sublattices depicted as red and blue, respectively. Primitive lattice vectors a_1 and a_2 allow for translational invariant motion along lattice. δ_1 , δ_2 and δ_3 point out the position of the nearest neighbor from an A atom to surrounding B atoms (b) Reciprocal lattice vectors b_1 and b_2 are in the Brillouin zone.....	15

Figure 2.3: Energy band structure of single layer graphene. (a) Band structure of SLG from the tight binding calculation (b) Cross section along the line k_y from (a). image from ref. 3.	19
Figure 2.4: Crystal structure of BLG. (a) Top and side view of honeycomb carbon lattice of BLG in real space (b) The unit cell including four atoms: A and B atoms from the bottom layer and \tilde{A} and \tilde{B} from the top layer.....	21
Figure 2.5: Low-energy band structure of BLG. Band structure of BLG from the tight binding calculation with $\gamma_0 = 3.033 \text{ eV}$, $S_0 = 0.129$ and $\gamma_1 = 0.39 \text{ eV}$ Adapt from ref 6	24
Figure 2.6: Low-energy band structure of BLG for induced asymmetry gap. Band structure of BLG from the tight binding calculation with with $\gamma_0 = 3.033 \text{ eV}$, $S_0 = 0.129$ and $\gamma_1 = 0.39 \text{ eV} = \Delta$. Image from ref.3.	26
Figure 2.7: Schematics of Bernal stacked and Rhombohedral stacked trilayer graphene	27
Figure 2.8: Schematics of side view of Bernal-stacked and Rhombohedral-stacked trilayer graphene The unit cell includes 6 atoms considering the only the nearest intra-layer and interlayer hopping terms.....	28
Figure 2.9: Energy band structure of TLG. (a) Band structure of ABA trilayer and (b) ABC trilayer graphene from the tight binding calculation	31
Figure 2.10: Energy band structure of TLG in the layer asymmetry. (a) Band structure of ABA trilayer and (b) from the tight binding calculation considering $\Delta_1 = 0.5\gamma_1$ and $0.1\gamma_1$	34

Figure 3.1: Identification of the number of layers. (a) Optical images of SLG, BLG and TLG. (b) The values of relative green shift channel for SLG, BLG and TLG (c) The Raman spectroscopy of TLG (d) The intensity ratio (I_G/I_{2D}) of SLG, BLG and TLG.	38
Figure 3.2: Raman spectroscopy of (a) ABA-stacked TLG and (b) ABC-stacked TLG in the 2D mode using 532 nm laser.....	40
Figure 3.3:Alignment mark of the normal matrix and extra matrix (a) 1440 × 1440 (mm × mm) alignment matrices (b) the number matrices every 300mm (c) extra alignment nearby graphene (d) High resolution image of extra alignment	42
Figure 3.4:Top gate fabrication process (a) Spin coat LOR and PMMA(b) EBL pattern for step 1-e (c) Remove PMMA (d) Spin coat MMA and PMMA (e) EBL pattern for step 2-e (f) Deposit metal (g) Life-off metal (f) SEM image of the top gate	43
Figure 3.5: Schematic of etching proces.....	44
Figure 3.6 :Top gate protocol (a) Global top-gate design (b) Local top-gate design (c) Split two top-gate design	47
Figure 3.7: Schematic images of light bulb and graphene bulb.....	49
Figure 3.8: Schematic of current annealing circuit.....	50
Figure 3.9: Annealing result of TLG (a) $G(V_{bg})$ after each cycle of annealing (b) $I-V$ curve of annealing.....	51

Figure 3.10: Annealing result of BLG (a) I - V curve of annealing (b) $G(V_{bg})$ after each cycle of annealing. Note that initially, the overall conductance is low indicating that the contact is poor. However, the contact improves considerably during annealing, as evidenced by the sudden increase in current during 1st annealing. 53

Figure 3.11: Overannealed device (a) I - V curve of annealing (b) $G(V_{bg})$ after each cycle of annealing. After the 13th annealing cycle, the dirac point shifts away from 0V and the mobility decreases..... 54

Figure 4.1: (a) Ratio of the intensities of G and $2D$ bands in graphene's Raman spectrum as a function of number of layers. Inset: SEM image of a dual-gated suspended BLG device. (b). Atomic structures of BLG. Red atoms belong to the sublattice A of the top layer, and blue atoms to sublattice B of the bottom layer. The gray atoms are vertically stacked; they hybridize to form high energy bands and can be ignored in low energy approximation. (c-d). Band structure of BLG at zero and finite $E \perp$, respectively. 59

Figure 4.2: (a). $G(V_{bg}, V_{tg})$ of a device with mobility 10,000 cm²/Vs at $B=0$. (b). Same data as (a) plotted as $G(n)$. (c). Line trace $G(n)$ at $E \perp=0$. (d). Line trace $G(t \perp)$ at $n=0$ 62

Figure 4.3: Raman and transport data from a TLG pnp junction. (a). Raman spectrum of the TLG device. (b). $R(V_{bg}, V_{tg})$ of the TLG device at $B=0$. (c). Line traces through (a) at, from red to blue, $V_{tg}=13.5$ (CNP), 0, 10, 20, and 28V, respectively 64

Figure 5.1: (a) SEM image of a dual-gated suspended TLG device. (b) $G(V_{bg})$ before (black) and after (red) current annealing and $G(V_{tg})$ after (blue) current annealing. 70

Figure 5.2: (a) Low energy band structure of ABA-stacked TLG calculating using only γ_0 and γ_1 , (b) using $\gamma_0 - \gamma_5$. Inset: ABA-stacked TLG lattice with hopping parameters $\gamma_1 - \gamma_5$ 71

Figure 5.3: (a-b). $G(V_{bg}, B)$ and dG/dV_{bg} of a TLG device. Numbers indicate filling factors. The color scale in a indicate conductance in units of e^2/h . (c). $G(V_{bg})$ and $G(v)$ at $B=1.5, 2.2, 3.5$ and 4.2 T, respectively (from blue to red). (d). $G(V_{bg})$ and $G(v)$ at $B=4.5, 6, 7, 8$ and 10 T (from blue to red). (e). $G(V_{bg}, B)$ and $G(v)$ at $B=10, 12, 14, 16$ and 18 T (from blue to red). 72

Figure 5.4: (a-c). $G(n, E_{\perp})$ at $B=5.5, 14$ and 8 T. (a) and (b) has the same color scale, and color scale of c is shown in panel (d). The arrows in (b) indicate the asymmetry in E_{\perp} in electron- and hole-doped regimes. (d). $G(n)$ along the horizontal lines in (c) at $E_{\perp}=0$ (red), 43 (green dotted line) and 73 mV/nm (blue), respectively. Color scales: G in units of e^2/h . (e). $G(E_{\perp})$ along the vertical line in (c) at $n=0$. (f). $E_{ic}(B)$ from 3 different devices. The black and orange lines correspond to linear and $B^{1/2}$ fits, respectively. 77

Figure 5.5: (a). $G(n, E_{\perp})$ at $B=7$ T in units of e^2/h . (b). $G(n)$ at $E_{\perp}=0$ (red solid line), -17 (green dotted line) and 13.6 mV/nm (blue dashed line). 78

Figure 6.1: Raman spectroscopy, SEM image and current annealing (a) Raman spectroscopy of r-TLG sheet. (b) SEM image of a dual-gated suspended device. (c) Device conductance G vs V_{bg} before and after current annealing. 86

Figure 6.2: Transport data of ABC trilayer device. (a) $G(U_{\perp}, n)$ in units of e^2/h . Inset: Energy-momentum dispersion of r-TLG. (b) $G(n)$ at $U_{\perp}=0$. Note the logarithmic scale of G 87

Figure 6.3: Transport data at $\mathbf{B} \perp=0$ (a) $G(V)$ at $\mathbf{U} \perp=n=0$. (b) $G(V)$ at $\mathbf{U} \perp=0$ and different n 88

Figure 6.4: Transport data at $\mathbf{B} \perp=0$ (a) $G_{\min}(V)$ at $\mathbf{U} \perp=n=0$ and different temperatures. (b) G_{\min} at $V=0$ vs. T . (c) G_{\min} vs. $1/T$ in Arrhenius scale. The blue line is a fit to the equation $\mathbf{G}_{\min} = \mathbf{G}0e - \Delta/2k\mathbf{B}T$ for $30\text{K}<T<40\text{K}$. (d) Measured Δ as a function of T . The solid line is a fit to equation 6.1. 90

Figure 6.5: Transport data at $n=0$ and finite $\mathbf{U} \perp$ and B_{\parallel} . (a)-(b) $G(V, \mathbf{U} \perp)$ and $G(V, \mathbf{U} \perp s)$ in units of e^2/h from Device 1. (c) Line traces $G(V)$ at $\mathbf{U} \perp=0$ and $\mathbf{U} \perp=-50$ mV. (d) $G(V, B_{\parallel})$ in units of e^2/h from Device 2 95

Figure 6.6: Possible phase diagram and schematics of electronic configurations for r-TLG. The blue and red arrows indicate charges from K and K' valleys, respectively. (QVH: quantum valley Hall; LAF: layer antiferromagnet; CAF: canted antiferromagnet; F: Ferromagnet)..... 104

Figure 7.1: Device image and current annealing (a). SEM image of a dual-gated TLG device. (b) Device conductance G vs V_{bg} before and after current annealing. 111

Figure 7.2: Transport data and schematics of orders of symmetry breaking (a). $G(B, \nu)$ of a r-TLG device with only back gate engaged, while top gate is disconnected or grounded. (b). Line traces $G(\nu)$ at $B=4.5\text{T}$ and 5.5T , respectively. (c-d). Schematics of orders of symmetry breaking in r-TLG in the QH regime. 113

Figure 7.3: Transport data of ABC trilayer graphene device (a-c). $G(B, \nu)$ in units of e^2/h at $\mathbf{U} \perp=0$, and line traces $G(\nu)$ at $B=5\text{T}$. (b-d). Similar data at $\mathbf{U} \perp=-20$ mV. 115

Figure 7.4: Transport data of ABC trilayer graphene device (a-b). $G(\mathbf{U} \perp, \nu)$ in units of e^2/h at $B=7T$ and $5T$, respectively. The arrows indicate line traces along which Fig. 2c and 2d would be taken. (c). Line traces $G(\mathbf{U} \perp)$ at $B=5T$ and $\nu=-1, -2$, and -3 . The triangles and squares mark $\mathbf{U} \perp \mathbf{c}$ values at which G is not quantized. 116

Figure 7.5: The energy gap of LLs and Schematic diagram of LL (a). Experimentally measured $\mathbf{U} \perp \mathbf{c}$ values as a function of B for $\nu=-2$ and -3 states, respectively. Red line: a linear fit with a slope ~ 5.6 meV/T. Blue line: a fit to Eq. (3). (b). Schematic diagram of LL energies under $\mathbf{U} \perp$. The red (blue) numbers indicate the indices of LLs with top (bottom) quantum numbers. The highlighted numbers denote the expected conductance values. 118

Figure 8.1: SEM image of a dual-gated device. 129

Figure 8.2: Magnetotransport data (a) $G(E_x, n)$ of Device 1 at $B=3.5T$. (b) Line traces $G(\nu)$ at $B=3.5T$ and $E_x=0$ (red dotted line) and $E_x=-21$ mV/nm (blue solid line), respectively. (c) Line trace $G(E_x)$ at $B=3.5T$ and filling factor $\nu=2$ (density $n=1.7 \times 10^{10}$ cm⁻²). Inset: Critical electric field E_{cx} vs. B and linear fit to the data points with slope ~ 0.72 mV/nm/T. (d) $G(n)$ of device 2 at $E_x=0$ and $B=10T$ and $24T$, respectively. 131

Figure 8.3: Model of transport across the device in the quantum Hall regime (a) At $V=0$, Fermi levels of the source (S) and drain (D) electrodes are located between the highest occupied Landau level and an unoccupied level. The bulk is gapped and transport occurs via edge states. (b) Similar to (a), except that a bias V is applied between S and D. (c) At $V=0$, Fermi levels of the electrodes are aligned with the occupied Landau level. Transport occurs via the bulk. 133

Figure 8.4: Transport spectroscopy data from Device 1. (a-b) $G(V, n)$ at $E_{\perp}=0$ and -14.4 mV/nm, respectively. Both data are taken at $B=3.5$ T. (c) Line trace $G(V)$ at $\nu=-2$ and $B=3.5$ T. Blue and red traces are taken at $E_{\perp}=0$ and -14.4 mV/nm, respectively. (d) Similar data taken at $B=6$ T. 134

Figure 8.5: Transport spectroscopy data from Device 1 (a) Measured LL gap $\Delta(B)$ at $\nu=2$ and $E_{\perp}=0$ and -14.4 mV/nm, respectively. (b) Schematics of transitions between Phase I and Phase II at $\nu=2$. (T: top layer; B: bottom layer; S: symmetric state $|S\rangle=|T\rangle+|B\rangle$; |AS>:antisymmetric state $|T\rangle-|B\rangle$) 135

Figure 8.6: Spectroscopy data from Device 2 at $B=10$ T and $\nu=2$. (a) $G(V, E_{\perp})$ data. (b) Line traces $G(V)$ at $E_{\perp}=0$ (blue), 15 (green) and -35 mV/nm (red). (c) $G(E_{\perp})$ at $V=0$. (d). Gap of layer polarized $\nu=2$ state vs. E_{\perp} 139

Figure 8.7: Transport and spectroscopy data at $B=5$ T and $\nu=2$. (a) $G(\nu, \mathbf{U}_{\perp})$ data. (b) Line traces $G(\mathbf{U}_{\perp})$ at $\nu=-2$ (red) and (c) $G(V, \mathbf{U}_{\perp})$ at $\nu=-2$. (d) Line traces $G(V)$ at $\mathbf{U}_{\perp}=0$ (red) and -18mV. 140

List of Tables

Table 1.1: Dispersion relation, the density of states and the Fermi energy of SLG, BLG and TLG.....	6
Table 3.1: The fabrication procedure of extra alignment mark	41
Table 3.2 Procedure of the device fabrication	45
Table 8.1: Schematic diagram of electronic configurations of the states stabilized by electric field and magnetic field.....	128
Table 8.2: LL energy gap at different magnetic field and QH filling factor	141

Chapter 1 : Introduction

Background

One meeting changed my life. One meeting changed my entire PhD outlook.

When I first joined the University of California, Riverside (UCR) as a first-year graduate student, I aspired to research high-energy physics by continuing my master degree project and participating in the world famous Large Hadron Collider (LHC) experiment.

However, after attending a seminar at UCR in the department of Physics and Astronomy, I was introduced to a plethora of condensed matter research which piqued my interest. It was then that I learned from Prof. Jeanie Lau about the wonder material called graphene. I found it quite intriguing to think about the similarities and differences between graphene research and particle physics, and I decided to scale my research up to the nano level.

The first obvious and visible difference between the two types of research is the size of the equipment. As the world's largest particle accelerator, the LHC is one of the largest and most technologically-sophisticated man-made structures in the world with a 27 kilometer-long circumference, built 175 meters below the ground. The superconducting magnet ring has the incredible power to boost hadrons to close to the speed of light. In contrast, the superconducting cryostats used for electronic transport measurements in a typical condensed matter laboratory are about only 1 meter in diameter. This corresponds to a reduction in size by about four orders of magnitude when compared to the LHC. Indeed, this means that the LHC experiment requires much more funding than graphene research, due to its huge material, construction, personnel, and energy costs. The beauty

of graphene research is that the particles being studied, such as electrons and holes instead of hadrons, can travel with an effective relativistic speed inside \sim a few μm -sized carbon flat-land without the need of an expensive particle accelerator. This provides a convenient experimental playground for researchers to study relativistic physics in a condensed matter platform.

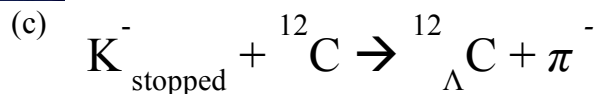
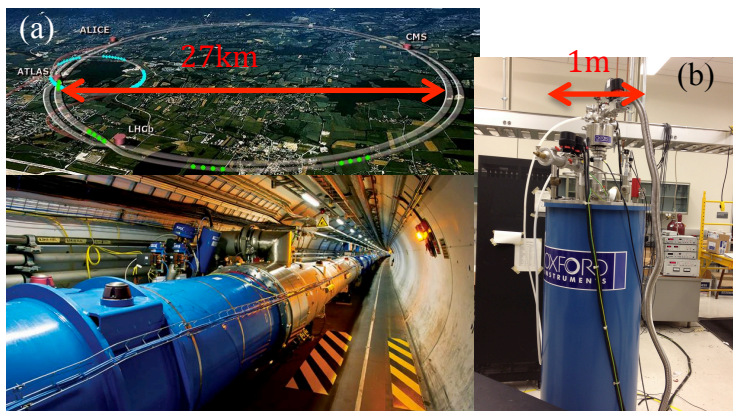


Figure 1.1: Images of (a) LHC accelerator in CERN and (b) Oxford fridge in UCR (c) Production of lambda particle

1-1 : Still Carbon

My master thesis¹ in the field of nuclear physics was titled: “Experimental study of ${}^{12}_{\Lambda}\text{C}$ proton weak decay with FINUDA”. The main procedure of the experiment was to hit a carbon target with a negative kaon beam² which was produced via the collision reaction between an electron and positron, so as to study the decay of hypernuclei³ as

shown in figure 1.1c. Thus I have had experience with the material carbon, albeit not as a two-dimensional electron gas, but rather as a reaction storage place to generate hypernuclei.

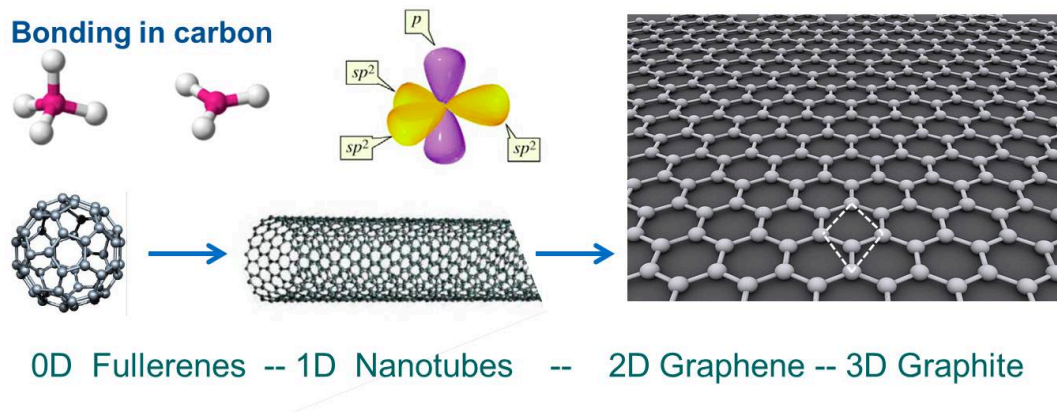


Figure 1.2: Formation of the sp hybridization electron state and various dimensionality in carbon

Now I will discuss the electronic configuration within the carbon atom. The carbon atom has a mere six electrons; two of them form a complete $1s^2$ orbital shell and the others fill $2s$ and $2p$ orbital states. The ground state configuration would be $2s^2 2p^2$ if we expect the carbon to be divalent. However, I discuss the carbon atoms which create a tetravalent bond with its neighbors due to the formation of the sp hybridization⁴ electron state.

Graphene is a flat monolayer of carbon atoms with a two-dimensional honeycomb lattice and is the mother of all carbon allotropes of other dimensionality, as shown in figure 1.2. For example, zero-dimensional fullerenes (C60) can be cut and wrapped from

graphene sheets, resembling a soccer ball with a carbon atom at the vertex of each polygon and with a σ bond along each polygon edge⁵. A 1D carbon nanotube is obtained by rolling up a graphene sheet and connecting the two edges. Layers of graphene can also be simply stacked onto one another to form 3D graphite.

In graphene, the electrons in each carbon atom form covalent σ bonds (i.e. hybridized sp^2 states) with three neighbors, establishing the hexagonal lattice structure of graphene, as shown in figure 1.2. The remaining out-of-plane p_z orbitals of the atoms form the π states which are weakly bonded. The focus of my PhD research has been to study the π electrons in 2D graphene.

1-2: 2D electron system

Before the emergence of graphene research, gallium arsenide (GaAs)/aluminum gallium arsenide (AlGaAs) heterojunctions⁶ provide the high-quality two-dimensional systems for transport experiments. At the interface between GaAs and AlGaAs, a 2D conducting layer is formed at the inversion layer near interface⁷, as shown in figure 1.3. This system itself is not truly a 2-dimension but has a finite thickness.

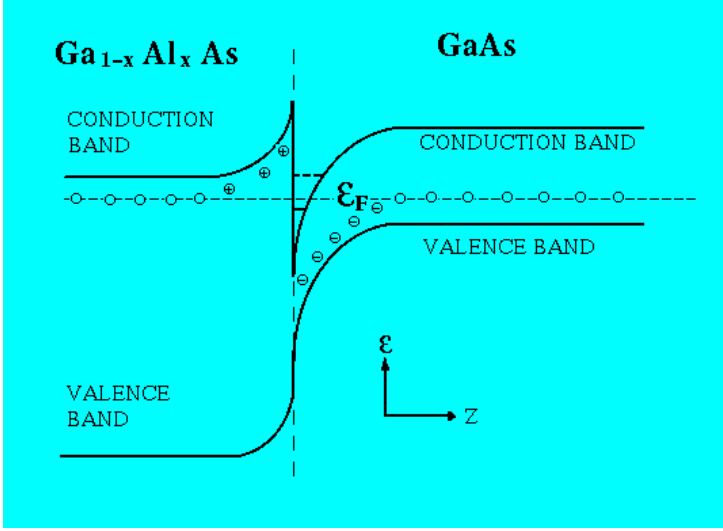


Figure 1.3: Electron energy level diagram of a GaAs-AlGaAs heterostructure device. Image from ref⁸

In contrast to GaAs/AlGaAs, single layer graphene is the thinnest possible 2D system. Interestingly, each additional layer dramatically alter graphene's electronic properties. Here I will discuss the differences of the density of states and Fermi energy of single-layer graphene(SLG), bilayer graphene(BLG) and trilayer graphene(TLG).

The density of states (DOS) of an electron gas is one of the most basic concepts in solid state physics. It describes the number of states per interval of energy at each energy level, and is strongly dependent on the dispersion relation and the dimensionality of the system. The density of states of a 2-dimensional system is given by

$$D(\varepsilon) = \int \frac{d^2k}{(2\pi)^2} \delta(\varepsilon - \varepsilon_k) \quad (1.1)$$

The energy dispersion relations with respect to wave vector of SLG, BLG and rhombohedral-stacked TLG (r-TLG) are simply linear, quadratic and cubic, respectively, in the low-energy approximation (see detail calculations in chapter 2). The density of

states of SLG, BLG and r-TLG are linear, constant and scale with the power of -1/3 in density, respectively. This remarkable discrepancy in density of states arises by simply adding layers. In particular, the DOS of r-TLG is divergent at the ground state energy, whereas the DOS of SLG approaches zero. A mathematical calculation of the density of states for SLG, BLG and r-TLG are shown in appendix B. Finally, from the relation between charge carrier density and the density of states, we can get the Fermi energy as a function of charge carrier density:

$$n = \frac{N}{A} = \int_0^{\varepsilon_f} D(\varepsilon) d\varepsilon \quad (1.2)$$

Table 1.1: Dispersion relation, the density of states and the Fermi energy of SLG, BLG and TLG.

	Dispersion relation	Density of state	Fermi energy
SLG	$H_{\text{mono}} = [\hbar \cdot V_F] k$	$D(\varepsilon) = 2 \cdot \frac{\varepsilon}{\pi [\hbar \cdot V_F]^2}$	$\varepsilon_F = \hbar \cdot V_F \sqrt{n\pi}$
BLG	$H_{\text{Bi}} = \frac{\hbar^2 V_F^2 k^2}{\gamma_1}$	$D(\varepsilon) = \frac{2m}{\pi \hbar^2}, m = \gamma_1 / 2v^2$	$\varepsilon_F = \frac{\pi \hbar^2}{2m} \cdot n$
TLG	$H_{\text{Tri}} = \frac{\hbar^3 V_F^3 k^3}{\gamma_1^2}$	$D(\varepsilon) = \frac{2\gamma_1^{4/3}}{3\pi(\hbar V_F)^2} \cdot \varepsilon^{-1/3}$	$\varepsilon_F = \frac{(\hbar V_F)^3}{\gamma_1^2} (n\pi)^{3/2}$

As graphite has been studied for decades, a natural question to ask is that when few-layer graphene ends and graphite begins. Theoretically, the energy band of 10 layers of graphene approaches that of graphite⁹. However, from an experimental point of view, it is interesting to construct graphite layer by layer, understand how electronic properties are modified with each addition and stacking orientation, and gain insight into 2D systems in the process.

1-3: Quantum Hall effect

In the classical Hall effect, for a conductor or semiconductor placed in a out-of-plane magnetic field, As shown in figure 1.4, a uniform current flows along the x-direction and results in a longitudinal voltage drop $V_{xx}=(V_1-V_2)$ in the x-direction and a Hall voltage drop, as shown in figure 1.4. $V_{xy}=(V_2-V_3)$ in the y-direction. The Hall and longitudinal conductivities are

$$\sigma_{xy} = \frac{\rho_{xy}}{\rho_{xx}^2 + \rho_{xy}^2} \quad \text{and} \quad \sigma_{xx} = \frac{\rho_{xx}}{\rho_{xx}^2 + \rho_{xy}^2}. \quad (1.3)$$

When a clean sample is placed in low temperature and a strong magnetic field, the quantum Hall effect emerges: The cyclotron orbits of the charged particles is quantized in the presence of strong out-of-plane magnetic field and the charged particles can occupy orbits with discrete energy levels which are called Landau levels. The hall conductivity undergoes a quantum Hall transition due to the vanishing of ρ_{xx} ; σ_{xx} becomes zero and the σ_{xy} exhibits well developed plateaus as a function of carrier density as shown in figure 1.4b. The quantization of Hall conductivity is

$$\sigma_{xy} = gN \frac{e^2}{h} \quad (1.4)$$

where g is the degeneracy of the system and h is Planck constant. N is the Landau level (LL) index. The dispersion of the LLs is a confining potential gives rise to conducting 1D channels propagating along the edges. These edge states counter-propagate on opposite

sides of the 2DEG system, and are topologically protected from back scattering, thus allowing dissipationless transport.

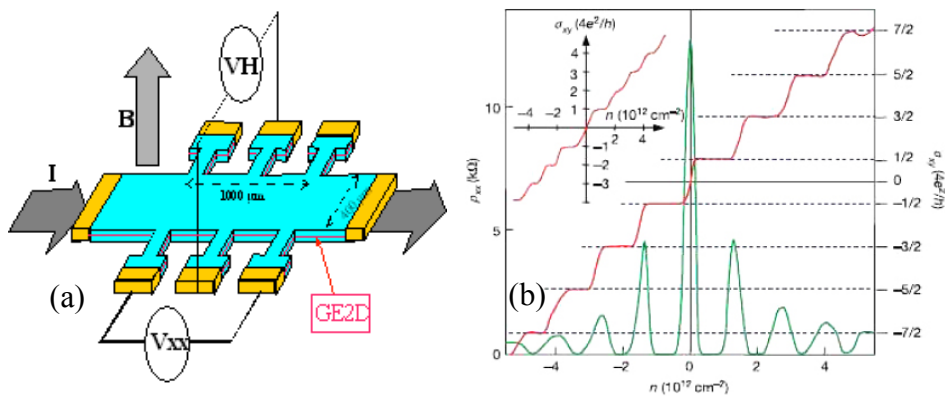


Figure 1.4: Two-dimensional electron gas with (a) Hall bar geometry and (b) transport data.

1-4: Thesis Outlines

The thesis is organized as follows. Chapter 2 presents the theoretical background of SLG, BLG and TLG by focusing on tight binding calculations. Chapter 3 describes the experimental techniques of identifying the number of layer and the stacking order of graphene sheets, as well as fabrication procedure of high quality graphene devices with suspended structures, including dual gated graphene devices that are suspended or

supported on substrates. In chapter 4, I will discuss the external electric effect on dual-gated bilayer and trilayer graphene. In zero magnetic fields, we observe formation of *pnp* junctions with tunable polarity and charge densities, as well as a tunable band gap in bilayer graphene and a tunable band overlap in trilayer graphene.

In chapter 5, we investigate ABA-stacked trilayer graphene that is a unique 2D electron system with mirror reflection symmetry and unconventional quantum Hall effect. We present low temperature transport measurements on dual-gated suspended trilayer graphene in the quantum Hall (QH) regime as a function of electric and magnetic field. We observe lifting of the 12-fold degeneracy of the lowest Landau levels, and degeneracy breaking and transitions between QH plateaus.

In chapter 6, we report observation of a giant intrinsic gap $\sim 42\text{meV}$ in rhombohedral-stacked trilayer graphene that can be partially suppressed by an interlayer potential, a parallel magnetic field or a critical temperature $\sim 36\text{K}$. Among the proposed correlated phases with spatial uniformity, our results are most consistent with a layer antiferromagnetic state with broken time reversal symmetry.

In chapter 7, we discuss QH state in dual-gated rhombohedral trilayer graphene (r-TLG) devices. We find that the sequence of symmetry-broken quantum Hall plateaus depends strongly on the interlayer potential bias U_{\perp} . In the phase space of U_{\perp} and filling factor ν , we observe an intriguing “hexagon” pattern, which can be accounted for by a model based on crossings between symmetry-broken LLs. Using this model, we determine that energy gaps for the $\nu=-2$ and -3 states scale with B and $B^{1/2}$, respectively,

reflecting the interplay between single particle remote hopping and interaction-induced symmetry breaking.

In chapter 8, we discuss the Landau level gaps in bilayer and ABC trilayer graphene by using transport spectroscopy measurement. We find two distinct states that have two quantum units of Hall conductivity, stabilized by large magnetic and electric fields, respectively. The majority spins of both phases form a quantum anomalous Hall state; the minority spins constitute a Kekulé state with spontaneous valley coherence for phase I, and a quantum valley Hall state for phase II.

Finally, in chapter 9, I conclude the thesis with a brief conclusion and outlook for future work.

Reference

- 1 Lee Yongjin. *Experimental study of ^{12}C and ^5He proton weak decay with FINUDA*, Seoul National University, (2008).
- 2 Agnello, M. *et al.* Correlated Δ d pairs from the reaction. *Physics Letters B* **654**, 80-86, doi:<http://dx.doi.org/10.1016/j.physletb.2007.08.051> (2007).
- 3 Agnello, M. *et al.* Measurement of the proton spectra from non-mesonic weak decay of ^5He , ^7Li and ^{12}C . *Nuclear Physics A* **804**, 151-161, doi:<http://dx.doi.org/10.1016/j.nuclphysa.2008.02.003> (2008).
- 4 Neto, A. H. C., Guinea, F., Peres, N. M. R., Novoselov, K. S. & Geim, A. K. The electronic properties of graphene. *Reviews of Modern Physics* **81**, 109-162, doi:10.1103/RevModPhys.81.109 (2009).
- 5 Geim, A. K. & Novoselov, K. S. The rise of graphene. *Nat Mater* **6**, 183-191 (2007).
- 6 Lommer, G., Malcher, F. & Rössler, U. factor of subband Landau levels in AlGaAs/GaAs heterostructures. *Physical Review B* **32**, 6965-6967 (1985).
- 7 Datta, S. *Electronic Transport in Mesoscopic Systems*. (Cambridge University Press, 1997).
- 8 Qiu, Y. *Two Dimensional Electron Systems*.
- 9 Partoens, B. & Peeters, F. M. From graphene to graphite: Electronic structure around point. *Physical Review B* **74**, 075404 (2006).

Chapter 2 : Tight binding model for mono-, bi- and trilayer graphene

In this chapter we will discuss the tight binding model and its application to mono-, bi- and trilayer graphene. This theoretical calculation, though relatively simple, is remarkably successful in explaining the electronic properties of these graphene systems. Section 2.1 presents the tight-binding model in a general system, and Section 2.2 its application to monolayer graphene. Section 2.3 and Section 2.4 discuss the tight-binding model of bilayer graphene and its asymmetry gap case. Lastly section 2.5 and section 2.6 present the energy band structure from the tight binding calculation of trilayer graphene without and with asymmetry gap, respectively.

2.1: Tight Binding Method

The tight binding(TB) method¹ is a general tool to calculate the energy band structure of materials. This method explores the energy bands which are modified when the electron atomic wave functions of the electrons at the isolated atoms become overlapped. For example, consider two spatially separated hydrogen atoms with ground state wavefunctions ψ_A and ψ_B . When the two atoms are approaching each other, their wavefunctions overlap, giving rise to $\psi_A \pm \psi_B$ in figure 2.1. The electron's energy of the bonding orbital $\psi_A + \psi_B$ is lower than that of the anti-bonding $\psi_A - \psi_B$ state, for the following reason. In the state $\psi_A + \psi_B$, the electron spend some time in the middle of the two atoms, and in this region the electron has the influence of the attractive potential of both protons at once, thereby increasing the binding energy. In the state $\psi_A - \psi_B$, there is no probability of the electron's density in the midway between two proton. It does not

involve an extra contribution to the binding. As a result, the energy level splits into two bands for each level of the isolated atom².

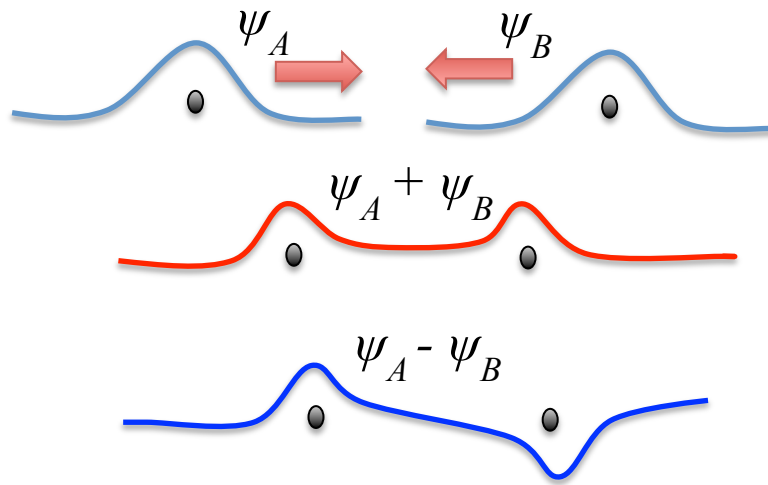


Figure 2.1:Schematic image for wavefunctions of electrons for two hydrogen atoms.

Generally speaking, if N atoms are included in the tight binding model, the electronic wave functions can be expressed a linear combination of Bloch functions.

$$\psi_i(k, r) = \sum_{j=1}^n a_{ij} \phi_j(k, r) \quad (2.1)$$

Here, a_{ij} and $\phi_j(k, r)$ are expansion coefficients and Bloch functions which can be expressed by

$$\phi_j(k, r) = \frac{1}{\sqrt{N}} \sum_{l=1}^N e^{ik \cdot R_{jl}} \phi_j(r - R_{jl}) \quad (2.2)$$

ϕ_j and R_{jl} are the atomic orbital per unit cell and position vector of the j th orbital in the l th unit cell, respectively. The eigenenergy $E_j(k)$ of the i th band, the inner product of the Schrodinger equation is given by

$$\begin{aligned} E_i(k) &= \frac{\langle \psi_i | H | \psi_i \rangle}{\langle \psi_i | \psi_i \rangle} \\ &= \frac{\sum_{jl}^n a_{ij}^* a_{il} \langle \phi_j | H | \phi_l \rangle}{\sum_{jl}^n a_{ij}^* a_{il} \langle \phi_j | \phi_l \rangle} = \frac{\sum_{jl}^n a_{ij}^* a_{il} H_{jl}}{\sum_{jl}^n a_{ij}^* a_{il} S_{jl}} \end{aligned} \quad (2.3)$$

where the transfer integral Matrix H and overlap integral matrix S are defined by

$$H_{jl} = \langle \phi_j | H | \phi_l \rangle \text{ and } S_{jl} = \langle \phi_j | \phi_l \rangle. \quad (2.4)$$

Energy band E_i can be determined by solving the secular equation,

$$\det(H - E_i S) = 0 \quad (2.5)$$

where the number of solutions is dependent on the number of orbitals per unit cell. In the next section, we will apply this generalized eigenvalue problem to the single layer graphene system.

2.2: Tight binding model of single layer graphene

The real space lattice of single layer graphene (SLG) is a honeycomb lattice shown in figure 2.2. The sublattices A and B are shown as blue and red. The Bravais lattice is given by the A-B pairs with primitive lattice vectors,

$$\vec{a}_1 = \frac{a}{2}(3, \sqrt{3}) \quad \vec{a}_2 = \frac{a}{2}(3, -\sqrt{3}) \quad (2.6)$$

where $a \approx 1.42 \text{ \AA}$ is the nearest-neighbor distance. The reciprocal lattice vectors is also a honeycomb lattice, with vectors,

$$\vec{b}_1 = \frac{2\pi}{3a}(1, \sqrt{3}) \quad \vec{b}_2 = \frac{2\pi}{3a}(1, -\sqrt{3}) \quad (2.7)$$

in the k_x - k_y plane.

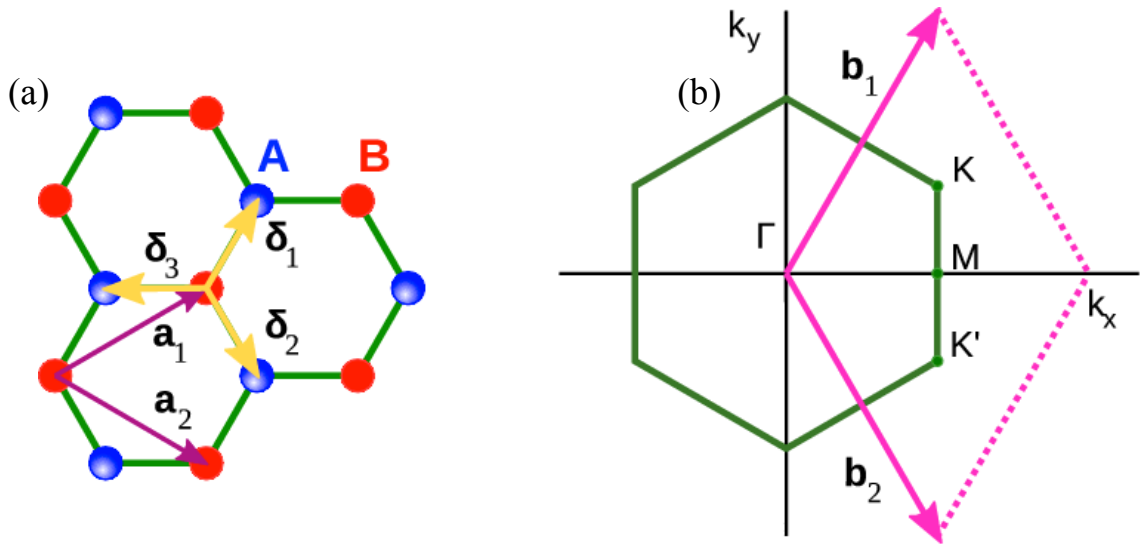


Figure 2.2: Crystal structure of SLG and Reciprocal lattice. (a) Honeycomb carbon lattice of graphene with A and B sublattices depicted as red and blue, respectively. Primitive lattice vectors a_1 and a_2 allow for translational invariant motion along lattice. δ_1 , δ_2 and δ_3 point out the position of the nearest neighbor from an A atom to surrounding B atoms (b) Reciprocal lattice vectors b_1 and b_2 are in the Brillouin zone.

For the tight binding calculation of the energy band structure of SLG, we will consider two Bloch functions from A and B sites which are used for the transfer Matrix H and overlap matrix S defined by equation (2.4).

$$\phi_A(k, r) = \frac{1}{\sqrt{N}} \sum_{l=1}^N e^{ik \cdot R_{Al}} \phi_A(r - R_{Al}) \quad (2.8)$$

$$\phi_B(k, r) = \frac{1}{\sqrt{N}} \sum_{m=1}^N e^{ik \cdot R_{Bm}} \phi_B(r - R_{Bm}) \quad (2.9)$$

$$\begin{aligned} H_{ij} &= \langle \phi_i | H | \phi_j \rangle \quad \text{at } i, j = A, B \\ &= \frac{1}{N} \sum_{lm} e^{ik \cdot (R_{jm} - R_{il})} \langle \phi_i(r - R_{il}) | H | \phi_j(r - R_{jm}) \rangle \end{aligned} \quad (2.10)$$

$$\begin{aligned} S_{ij} &= \langle \phi_i | \phi_j \rangle \quad \text{at } i, j = A, B \\ &= \frac{1}{N} \sum_{lm} e^{ik \cdot (R_{jm} - R_{il})} \langle \phi_i(r - R_{il}) | \phi_j(r - R_{jm}) \rangle \end{aligned} \quad (2.11)$$

The diagonal terms, H_{AA} and H_{BB} are identical since the A and B sites are both carbon atoms. Assuming that only the nearest neighbors hopping within the same sublattice have non-zero transfer matrix terms.

$$\begin{aligned}
H_{AA} = H_{BB} &= \frac{1}{N} \sum_{lm}^N e^{ik \cdot (R_{Am} - R_{Al})} \langle \varphi_A(r - R_{Al}) | H | \varphi_A(r - R_{Am}) \rangle \\
&= \frac{1}{N} \sum_l^N \langle \varphi_A(r - R_{Al}) | H | \varphi_A(r - R_{Al}) \rangle \\
&= \frac{1}{N} \sum_l^N \varepsilon = \varepsilon
\end{aligned} \tag{2.12}$$

where $\langle \varphi_A(r - R_{Al}) | H | \varphi_A(r - R_{Al}) \rangle = \varepsilon$. Similarly the diagonal element of the overlap matrix S_{AA} and S_{BB} are

$$S_{AA} = S_{BB} = \frac{1}{N} \sum_l^N e^{ik \cdot (R_{Al} - R_{Al})} \langle \varphi_A(r - R_{Al}) | \varphi_A(r - R_{Al}) \rangle = 1 \tag{2.13}$$

For the off-diagonal elements of the transfer matrix, we only consider the nearest neighbor terms. For example, an A atom is surrounded by three atoms depicted as $\delta 1$, $\delta 2$ and $\delta 3$ as shown in figure 2.2.

$$H_{AB} = \frac{1}{N} \sum_l^N \sum_{m=1}^3 e^{ik \cdot (R_{Al} - R_{Bm})} \langle \varphi_A(r - R_{Al}) | H | \varphi_B(r - R_{Bm}) \rangle \tag{2.14}$$

Each interaction term $\langle \varphi_A(r - R_{Al}) | H | \varphi_B(r - R_{Bm}) \rangle$ between the A atom and the three nearest neighbor B atoms is same equal to a constant $-\gamma_0$, where γ_0 is called the nearest neighbor hopping parameter.

$$\begin{aligned}
H_{AB} &= -\frac{1}{N} \sum_l^N \sum_{m=1}^3 e^{ik \cdot \delta_m} \gamma_0 \text{ at } R_{Al} - R_{Bm} = \delta_m \\
H_{AB} &= -\frac{1}{N} \sum_l^N f(k) \gamma_0 \text{ where } f(k) = \sum_{m=1}^3 e^{ik \cdot \delta_m} \quad (2.15) \\
&= -\gamma_0 f(k)
\end{aligned}$$

From the position of the nearest neighbor from an A atom to surrounding B atoms, the three vectors are

$$\begin{aligned}
\delta_1 &= \left(0, \frac{a}{\sqrt{3}}\right), \delta_2 = \left(\frac{a}{2}, -\frac{a}{2\sqrt{3}}\right), \delta_3 = \left(-\frac{a}{2}, -\frac{a}{2\sqrt{3}}\right) \\
f(k) &= \sum_{m=1}^3 e^{ik \cdot \delta_m} = e^{iky \frac{a}{\sqrt{3}}} + 2e^{-iky \frac{a}{2\sqrt{3}}} \cos\left(k_x \frac{a}{2}\right). \quad (2.16)
\end{aligned}$$

Similarly, the off-diagonal elements of the overlap matrix are

$$\begin{aligned}
S_{AB} &= \frac{1}{N} \sum_{l=1}^N \sum_m^3 e^{ik \cdot (R_{Al} - R_{Bm})} \langle \varphi_A(r - R_{Al}) | \varphi_A(r - R_{Bm}) \rangle \\
&= \frac{1}{N} \sum_{l=1}^N f(k) S_0 \text{ where } \langle \varphi_A(r - R_{Al}) | \varphi_A(r - R_{Bm}) \rangle = S_0 \quad (2.17) \\
&= S_0 f(k)
\end{aligned}$$

Therefore, the transfer integral Matrix H and overlap integral matrix S are

$$\begin{aligned}
H &= \begin{bmatrix} \varepsilon & -\gamma_0 f(k) \\ -\gamma_0 f(k)^* & \varepsilon \end{bmatrix} \\
S &= \begin{bmatrix} 1 & S_0 f(k) \\ S_0 f(k)^* & 1 \end{bmatrix} \quad (2.18)
\end{aligned}$$

where $H_{AB} = H_{BA}^*$ and $S_{AB} = S_{BA}^*$ in Hermitian conjugate condition.

To solve this Eigenvalue equation given by equation 2.17, the determinant is

$$\det \begin{bmatrix} \varepsilon - E & -(\gamma_0 + ES_0)f(k) \\ -(\gamma_0 + ES_0)f(k)^* & \varepsilon - E \end{bmatrix} = 0$$

$$(\varepsilon - E)^2 - |f(k)|^2(\gamma_0 + ES_0)^2 = 0 \quad (2.19)$$

$$E_{\pm} = \frac{\varepsilon \pm |f(k)|\gamma_0}{1 \mp |f(k)|S_0}$$

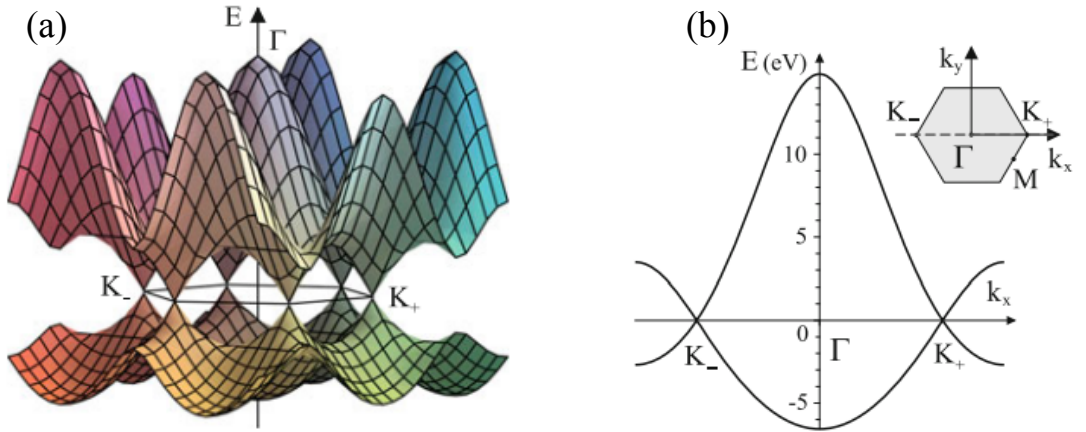


Figure 2.3: Energy band structure of single layer graphene. (a) Band structure of SLG from the tight binding calculation (b) Cross section along the line k_y from (a). image from ref. 3.

Figure 2.3a shows the band structure calculated from above equation in the first Brillouin zone (BZ) where E_+ and E_- indicate the conduction and valence band, respectively. The parameters¹ such as $\gamma_0 = 3.033$ eV, $S_0 = 0.12$ and orbital energy $\varepsilon = 0$ used in the calculation. Figure 2.3b shows that it is gapless and touching at K_- and K_+ points which is located at the corner of the first BZ

$$K_{\xi=\pm 1} = \xi \left(\frac{4\pi}{3a}, 0 \right). \quad (2.20)$$

In the vicinity of K_{ξ} valley, equation 2.16 can be performed to approximate with Taylor expansion considering only linear term in p

$$f(k) \approx -\frac{\sqrt{3}a}{2\hbar} (\xi p_x - ip_y) \text{ where } p_x = \hbar k_x - \hbar K_{\xi}. \quad (2.21)$$

An effective Hamiltonian at low energy becomes

$$\begin{aligned} H_{\xi} &= v \begin{bmatrix} 0 & \xi p_x - ip_y \\ \xi p_x + ip_y & 0 \end{bmatrix} \\ &= v \xi p \begin{bmatrix} 0 & e^{-i\varphi} \\ e^{i\varphi} & 0 \end{bmatrix} \end{aligned} \quad (2.22)$$

where $p_x + ip_y = p e^{i\varphi}$, $v = \frac{\sqrt{3}a\gamma_0}{2\hbar}$ is the Fermi velocity with $\sim 10^5$ m/s by using for $a \approx 1.42 \text{ \AA}$ and $\gamma_0 = 3.033 \text{ eV}$. From the secular equation, the energy eigenvalues and eigenstates are

$$E_{\pm} = \pm v p, \quad \psi_{\pm} = \frac{1}{\sqrt{2}} \begin{pmatrix} 1 \\ \pm \xi e^{i\xi\varphi} \end{pmatrix} e^{ip \cdot r / \hbar}, \quad (2.23)$$

where \pm denotes the conduction and valence bands. This linear dispersion is particularly significance, since the charge carriers in SLG behave as massless relativistic particles⁴ with an effective speed of light described by the Dirac equation.

2.3: Tight binding model of bilayer layer graphene

In Bernal-stacked bilayer graphene (BLG), a single layer graphene stack on top of another, with one sublattice above the center of the hexagons of the bottom layer, as shown figure 2.4. The primitive lattice vectors are the same as those of single layer

graphene under the translational invariance as described in figure 2.4a. The unit cell includes four different atoms: A and B atoms from the bottom layer and \tilde{A} and \tilde{B} from the top layer. \tilde{A} and B are directly stacked, comprising a dimer-bond. Here in addition to the nearest neighbor hopping, we consider also interlayer hopping; thus BLG has additional hopping term $\gamma_1 = \langle \varphi_{\tilde{A}}(r - R_{\tilde{A}}) | H | \varphi_B(r - R_B) \rangle = 0.39$ eV between the stacked atoms⁵.

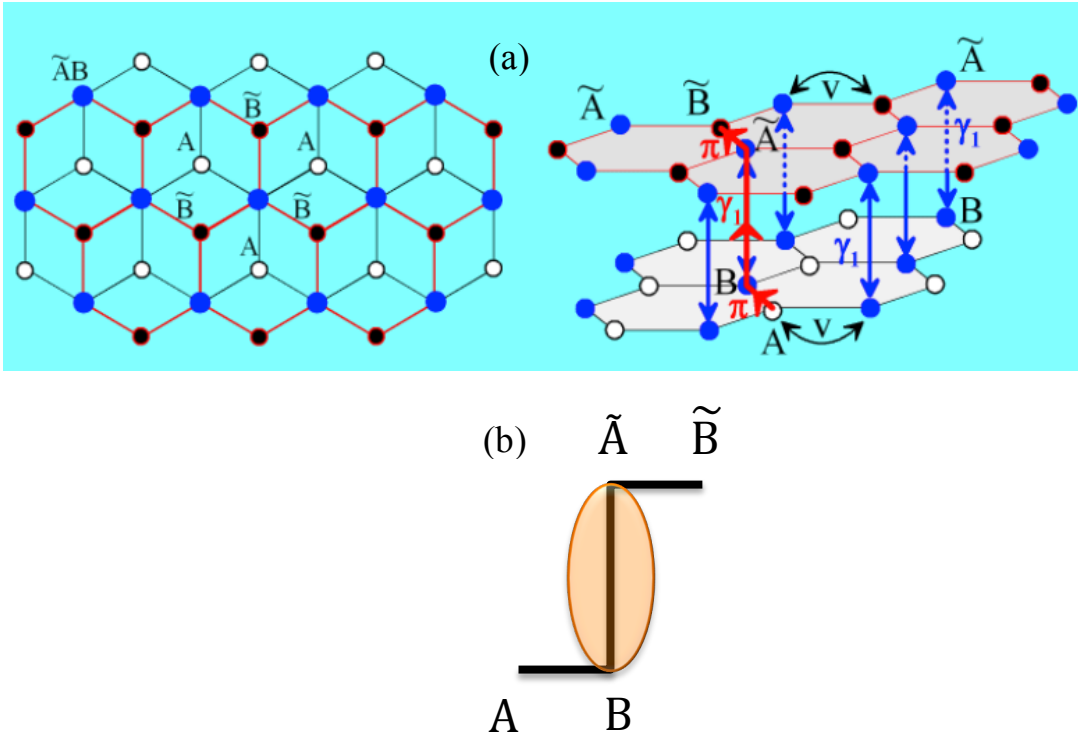


Figure 2.4: Crystal structure of BLG. (a) Top and side view of honeycomb carbon lattice of BLG in real space (b) The unit cell including four atoms: A and B atoms from the bottom layer and \tilde{A} and \tilde{B} from the top layer.

The transfer and overlap matrix for BLG are

$$H = \begin{bmatrix} A & B & \tilde{A} & \tilde{B} \\ A & \varepsilon & -\gamma_0 f(k) & 0 \\ B & -\gamma_0 f(k) & \varepsilon & \gamma_1 \\ \tilde{A} & 0 & \gamma_1 & \varepsilon \\ \tilde{B} & 0 & 0 & -\gamma_0 f(k) \end{bmatrix} \quad (2.24)$$

$$S = \begin{bmatrix} A & B & \tilde{A} & \tilde{B} \\ A & 1 & S_0 f(k) & 0 \\ B & S_0 f(k) & 1 & S_1 \\ \tilde{A} & 0 & S_1 & 1 \\ \tilde{B} & 0 & 0 & S_0 f(k) \end{bmatrix}$$

where $S_1 = \langle \varphi_{\tilde{A}}(r - R_{\tilde{A}}) | \varphi_B(r - R_B) \rangle$ describes the non-orthogonality of the orbitals at the dimer-bond. The 2×2 block matrix at the upper left and lower right exhibits the same transfer and integral matrices of SLG at the bottom and top layers, respectively. The off-diagonal 2×2 blocks describes the effect of interlayer coupling between B and \tilde{A} .

The band structure of BLG can be obtained by solving the secular equation. To simplify the equation, we can assume that the overlap integral matrix is a unit matrix and the orbital energy $\varepsilon=0$ as a reference point. Since S_0 and S_1 are negligible at the low energy, the determinant is given by

$$\det(H - ES) = 0$$

$$\det \begin{bmatrix} -E & -\gamma_0 f(k) & 0 & 0 \\ -\gamma_0 f(k) & -E & \gamma_1 & 0 \\ 0 & \gamma_1 & -E & -\gamma_0 f(k) \\ 0 & 0 & -\gamma_0 f(k) & -E \end{bmatrix} = 0 \quad (2.25)$$

The eigenvalues of this equation are given by

$$E_{\pm}^{\alpha} = \pm \frac{\gamma_1}{2} \left(\sqrt{1 + \frac{4\gamma_0^2 |f(k)|^2}{\gamma_1^2}} + \alpha \right), \quad \alpha = \pm 1 \quad (2.26)$$

The \pm sign refers to two conduction and valence bands, respectively, and $\alpha=1$

corresponds to the higher energy band. Equation 2.26 can be simplified in 2 limits. (1). In

the high energy limit, where $4\gamma_0^2 |f(k)|^2 \gg \gamma_1^2$, the higher energy bands can be

approximated by $E_{\pm}^1 \approx \pm(\gamma_0 |f(k)| + \frac{\gamma_1}{2})$ which describes two bands with a gap γ_1 at the

$|f(k)| = 0$. (2). In the low energy limit near K point $4\gamma_0^2 |f(k)|^2 \ll \gamma_1^2$, the energy

bands are $E_{\pm}^{-1} \approx \pm \frac{\gamma_0^2 |f(k)|^2}{\gamma_1}$ with $\gamma_0 = 3.033$ eV, $S_0 = 0.129$ and $\gamma_1 = 0.39$ eV at

$k_y=0$; here the valence and conduction bands touch at the K point⁶.

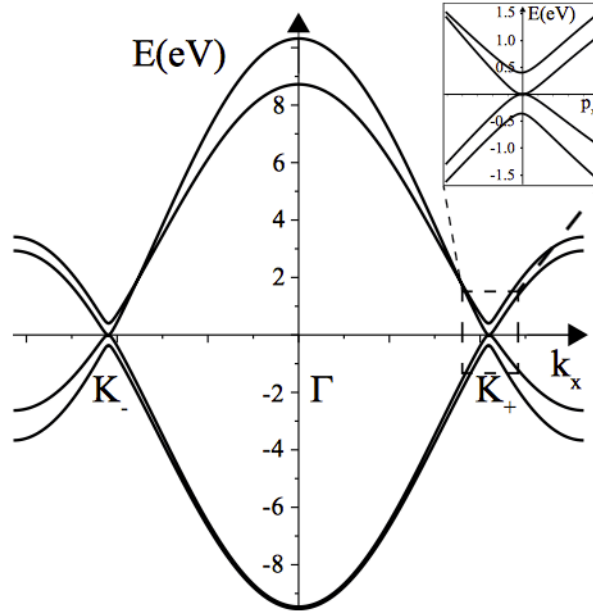


Figure 2.5: Low-energy band structure of BLG. Band structure of BLG from the tight binding calculation with $\gamma_0 = 3.033$ eV, $S_0 = 0.129$ and $\gamma_1 = 0.39$ eV Adapt from ref 6

2.4: Asymmetry gap in the band structure of bilayer graphene

In the both single and bilayer graphene, the conduction and valence bands touch at the K point due to A-B lattice symmetry which protects a combination of space and time inversion symmetry⁷, thus leading to a gapless band structure. Generating a band gap therefore requires breaking the A-B sublattice symmetry. This can be achieved by graphene/boron-nitride heterostructures. The different local potentials produced by boron and nitrogen atoms break the local sublattice symmetry of graphene, inducing a local band gap^{8,9}. For BLG, the inversion symmetry can be simply broken by applying an out-of-plane electric field, opening a band gap at degenerate K-point¹⁰.

Mathematically, consider the difference in energy ($\Delta = \varepsilon_2 - \varepsilon_1$) between the top(A_2, B_2) and bottom(A_1, B_1) layers, $\varepsilon_{A_2} = \varepsilon_{B_2} = \frac{\Delta}{2}$ and $\varepsilon_{A_1} = \varepsilon_{B_1} = -\frac{\Delta}{2}$. The transfer integral matrix of BLG at the low energy is

$$H = \begin{bmatrix} -\frac{\Delta}{2} & -\gamma_0 f(k) & 0 & 0 \\ -\gamma_0 f(k) & -\frac{\Delta}{2} & \gamma_1 & 0 \\ 0 & \gamma_1 & \frac{\Delta}{2} & -\gamma_0 f(k) \\ 0 & 0 & -\gamma_0 f(k) & \frac{\Delta}{2} \end{bmatrix} \quad (2.27)$$

$$\det \begin{bmatrix} -\frac{\Delta}{2} - E & -\gamma_0 f(k) & 0 & 0 \\ -\gamma_0 f(k) & -\frac{\Delta}{2} - E & \gamma_1 & 0 \\ 0 & \gamma_1 & \frac{\Delta}{2} - E & -\gamma_0 f(k) \\ 0 & 0 & -\gamma_0 f(k) & \frac{\Delta}{2} - E \end{bmatrix} = 0$$

The eigenvalues of this equation are given by

$$E_{\pm}^{\alpha} = \pm \left(\frac{\Delta^2}{4} + \gamma_0^2 |f(k)|^2 + \frac{\gamma_1^2}{2} \left\{ 1 + \alpha \sqrt{1 + \frac{4\gamma_0^2 |f(k)|^2}{\gamma_1^2} + \frac{4\gamma_0^2 \Delta^2 |f(k)|^2}{\gamma_1^4}} \right\} \right)^{1/2}, \quad \alpha = \pm 1 \quad (2.28)$$

where $\alpha=1$ and $\alpha=-1$ are for the high energy band and for the low energy band, respectively. At the K-point, $f(k) = 0$, the low energy band E_{\pm}^{-1} open a band gap with Δ . In the vicinity of K point, the energy band shows “Mexican hap” shape as shown in figure 2.6. Thus, since the energy difference between the layers can be experimentally controlled by the external top and bottom gates, BLG has tunable band gap at the K valley¹¹.

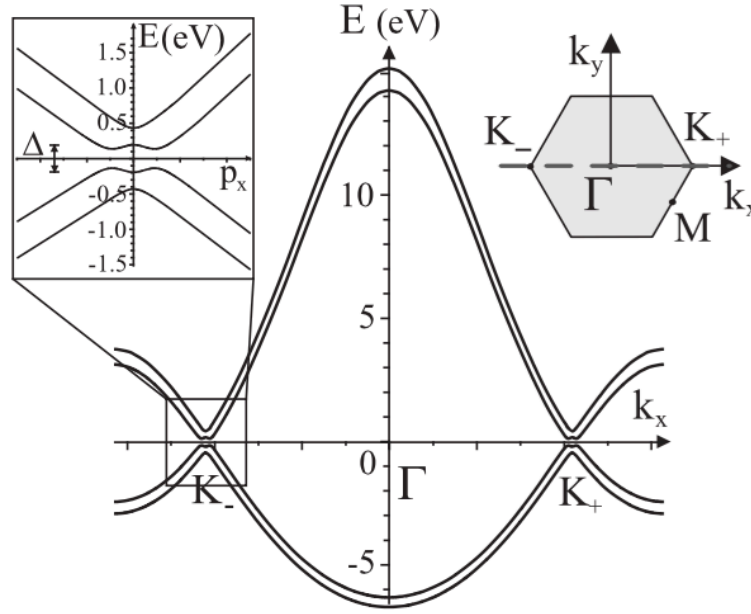


Figure 2.6: Low-energy band structure of BLG for induced asymmetry gap. Band structure of BLG from the tight binding calculation with $\gamma_0 = 3.033$ eV, $S_0 = 0.129$ and $\gamma_1 = 0.39$ eV = Δ . Image from ref.3.

2.5: Tight binding model of trilayer layer graphene

Unlike single and bilayer graphene, trilayer graphene (TLG) has two types of stable configurations: ABA (bernal) and ABC (rhombohedral) stacking orders. In both types, the first two layers are Bernal-stacked, where one sublattice of the middle layer is located above the center of the hexagons of the bottom layer. In ABA-stacked TLG, third layer is exactly on top of the lowest layer. In ABC-stacked trilayer, however, the top layer is shifted by the distance of an atom, so that the top and the bottom layers are also Bernal-stacked.

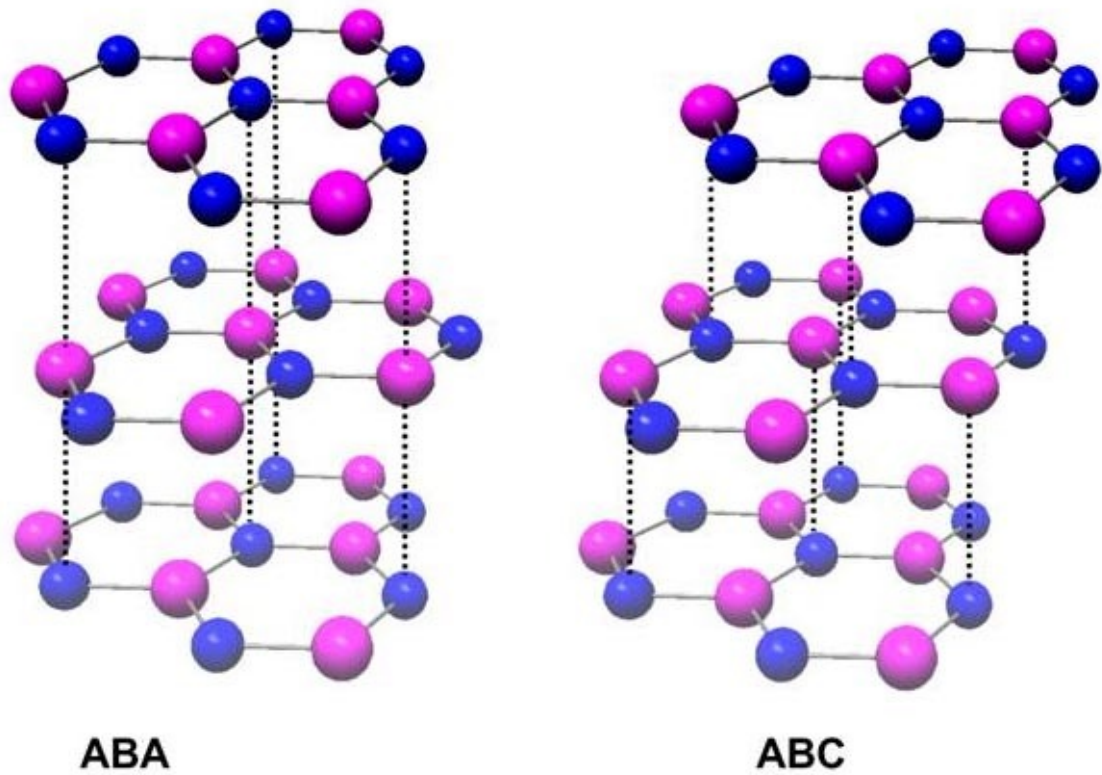


Figure 2.7: Schematics of Bernal stacked and Rhombohedral stacked trilayer graphene

To model the simplest tight binding calculation of TLG we consider the only the nearest intra-layer and interlayer hopping terms, γ_0 and γ_1 in the 6 atoms that comprise the unit cell at the low energy region; we will assume that the overlap integral matrix is a unit matrix. Regarding the effect of the remote hopping terms, we will discuss it later in chapter 5 and chapter 6.

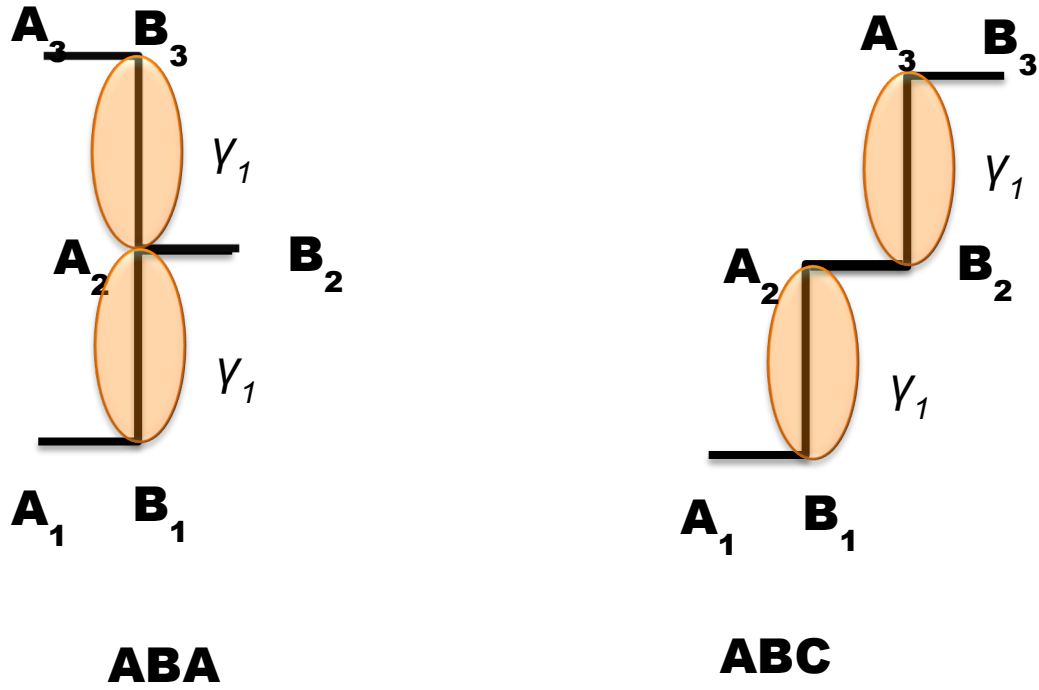


Figure 2.8: Schematics of side view of Bernal-stacked and Rhombohedral-stacked trilayer graphene The unit cell includes 6 atoms considering the only the nearest intra-layer and interlayer hopping terms.

The simplest Hamiltonian of ABA TLG is given by

$$H_{ABA} = \begin{bmatrix} A_1 & B_1 & A_2 & B_2 & A_3 & B_3 \\ A_1 & 0 & -\gamma_0 f(k) & 0 & 0 & 0 & 0 \\ B_1 & -\gamma_0 f(k) & 0 & \gamma_1 & 0 & 0 & 0 \\ A_2 & 0 & \gamma_1 & 0 & -\gamma_0 f(k) & 0 & \gamma_1 \\ B_2 & 0 & 0 & -\gamma_0 f(k) & 0 & 0 & 0 \\ A_3 & 0 & 0 & 0 & 0 & 0 & -\gamma_0 f(k) \\ B_3 & 0 & 0 & \gamma_1 & 0 & -\gamma_0 f(k) & 0 \end{bmatrix} \quad (2.29)$$

Performing the unitary transformation with the basis of linear combination of the atomic orbitals, $A_2, B_2, \frac{1}{\sqrt{2}}(A_1 - A_3), \frac{1}{\sqrt{2}}(B_1 - B_3), \frac{1}{\sqrt{2}}(A_1 + A_3)$ and $\frac{1}{\sqrt{2}}(B_1 + B_3)$, the Hamiltonian has two blocks, a monolayer-like and a bilayer-like Hamiltonian on the diagonal. Off-diagonal terms become zero in the simplest model.

$$\tilde{H}_{ABA} = \begin{bmatrix} H_s & 0 \\ 0 & H_b \end{bmatrix},$$

$$H_m = \begin{bmatrix} 0 & -\gamma_0 f(k) \\ -\gamma_0 f(k) & 0 \end{bmatrix}, \quad (2.30)$$

$$H_b = \begin{pmatrix} 0 & -\gamma_0 f(k) & 0 & 0 \\ -\gamma_0 f(k) & 0 & \gamma_1 & 0 \\ 0 & \gamma_1 & 0 & -\gamma_0 f(k) \\ 0 & 0 & -\gamma_0 f(k) & 0 \end{pmatrix}$$

Therefore the energy bands of ABA-stacked TLG is considered by a combination of the linear dispersion of SLG and quadratic relation of BLG, commonly referred to as the 1+2 model as shown in figure 2.9.

On the other hands, the nearest intra hopping term γ_1 in ABC trilayer (between B_1 - A_2 and B_2 - A_3) is different from those in ABA (B_1 - A_2 and A_2 - B_3) as shown in figure 2.8. This seemingly small distinction results in dramatic difference in energy band. The ABC TLG Hamiltonian and the secular equation are

$$H_{ABC} = \begin{bmatrix} & A_1 & B_1 & A_2 & B_2 & A_3 & B_3 \\ A_1 & 0 & -\gamma_0 f(k) & 0 & 0 & 0 & 0 \\ B_1 & -\gamma_0 f(k) & 0 & \gamma_1 & 0 & 0 & 0 \\ A_2 & 0 & \gamma_1 & 0 & -\gamma_0 f(k) & 0 & 0 \\ B_2 & 0 & 0 & -\gamma_0 f(k) & 0 & \gamma_1 & 0 \\ A_3 & 0 & 0 & 0 & \gamma_1 & 0 & -\gamma_0 f(k) \\ B_3 & 0 & 0 & 0 & 0 & -\gamma_0 f(k) & 0 \end{bmatrix}$$

$$(2.31)$$

$$\det \begin{bmatrix} & A_1 & B_1 & A_2 & B_2 & A_3 & B_3 \\ A_1 & -E & -\gamma_0 f(k) & 0 & 0 & 0 & 0 \\ B_1 & -\gamma_0 f(k) & -E & \gamma_1 & 0 & 0 & 0 \\ A_2 & 0 & \gamma_1 & -E & -\gamma_0 f(k) & 0 & 0 \\ B_2 & 0 & 0 & -\gamma_0 f(k) & -E & \gamma_1 & 0 \\ A_3 & 0 & 0 & 0 & \gamma_1 & -E & -\gamma_0 f(k) \\ B_3 & 0 & 0 & 0 & 0 & -\gamma_0 f(k) & -E \end{bmatrix} = 0$$

$$E^6 - E^4(2\gamma_1^2 + 3\gamma_0^2 f(k)^2) + E^2(\gamma_1^4 + 3\gamma_0^4 f(k)^4 + 2\gamma_1^2 \gamma_0^2 f(k)^2) - \gamma_0^6 f(k)^6 = 0$$

$$(2.32)$$

As shown in figure 2.9, the dispersion of the low energy band is cubic when considering the effective hoppings from A_1 to B_3 . The high energy bands are the quadratic dispersion from the B_1 - A_2 and B_2 - A_3 dimers.

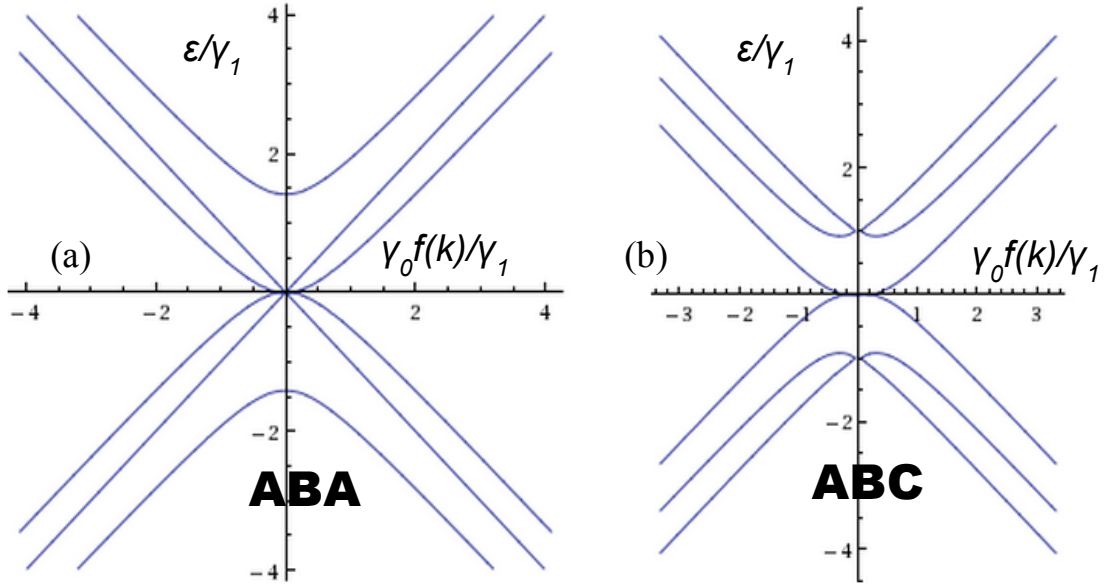


Figure 2.9: Energy band structure of TLG. (a) Band structure of ABA trilayer and (b) ABC trilayer graphene from the tight binding calculation

2.6: Asymmetry gap in the band structure of trilayer graphene

The simplest tight binding calculation of ABA and ABC TLG yield gapless band structures at the K point, where the degeneracy reflects the mirror reflection symmetry with respect to the middle layer of ABA TLG and the inversion symmetry in ABC TLG. With the presence of the external gate such as the top and back gates, these symmetries can be broken. In the following, we model the effective low energy Hamiltonian with the simplest tight binding model and the induced interlayer gap by the external gate.

Let's introduce the two parameters, Δ_1 and Δ_2 that define the interlayer asymmetry in the transfer matrix of ABA TLG. $\Delta_1 = -\frac{e(V_1 - V_3)}{2}$ is the energy difference between outmost layers and $\Delta_2 = -\frac{e(V_1 - 2V_2 + V_3)}{6}$ describes the energy difference between the

middle layer and the average of top and bottom layers where V_1 , V_2 and V_3 are the potential of the bottom, middle and top layers, respectively¹². Δ_1 is the only parameter to break mirror reflection symmetry so it can appear in the off-diagonal block. After a unitary transformation with linear combinations of the atomic orbitals¹³, $\frac{1}{\sqrt{2}}(A_1 - A_3)$, $\frac{1}{\sqrt{2}}(B_1 - B_3)$, $\frac{1}{\sqrt{2}}(A_1 + A_3)$, B_2 , A_2 , and $\frac{1}{\sqrt{2}}(B_1 + B_3)$, the transfer matrix of ABA TLG becomes

$$\tilde{H}_{ABA} = \begin{bmatrix} \Delta_2 & -\gamma_0 f(k) & \Delta_1 & 0 & 0 & 0 \\ -\gamma_0 f(k) & \Delta_2 & 0 & 0 & 0 & \Delta_1 \\ \Delta_1 & 0 & \Delta_2 & 0 & 0 & -\gamma_0 f(k) \\ 0 & 0 & 0 & -2\Delta_2 & -\gamma_0 f(k) & 0 \\ 0 & 0 & 0 & -\gamma_0 f(k) & -2\Delta_2 & \sqrt{2}\gamma_1 \\ 0 & \Delta_1 & -\gamma_0 f(k) & 0 & \sqrt{2}\gamma_1 & \Delta_2 \end{bmatrix}, \quad (2.33)$$

where $V_1 + V_2 + V_3 = 0$. To see the effect of the broken mirror symmetry, we assume $\Delta_2 = 0$. The transfer matrix and the secular equation are

$$\tilde{H}_{ABA} = \begin{bmatrix} 0 & -\gamma_0 f(k) & \Delta_1 & 0 & 0 & 0 \\ -\gamma_0 f(k) & 0 & 0 & 0 & 0 & \Delta_1 \\ \Delta_1 & 0 & 0 & 0 & 0 & -\gamma_0 f(k) \\ 0 & 0 & 0 & 0 & -\gamma_0 f(k) & 0 \\ 0 & 0 & 0 & -\gamma_0 f(k) & 0 & \sqrt{2}\gamma_1 \\ 0 & \Delta_1 & -\gamma_0 f(k) & 0 & \sqrt{2}\gamma_1 & 0 \end{bmatrix},$$

$$\det \begin{bmatrix} 0 & -\gamma_0 f(k) & \Delta_1 & 0 & 0 & 0 \\ -\gamma_0 f(k) & 0 & 0 & 0 & 0 & \Delta_1 \\ \Delta_1 & 0 & 0 & 0 & 0 & -\gamma_0 f(k) \\ 0 & 0 & 0 & 0 & -\gamma_0 f(k) & 0 \\ 0 & 0 & 0 & -\gamma_0 f(k) & 0 & \sqrt{2}\gamma_1 \\ 0 & \Delta_1 & -\gamma_0 f(k) & 0 & \sqrt{2}\gamma_1 & 0 \end{bmatrix} = 0$$

$$E^6 - E^4(2\gamma_1^2 + 3\gamma_0^2 f(k)^2 + 2\Delta_1^2) + E^2(\Delta_1^4 + 3\gamma_0^4 f(k)^4 + \gamma_1^2(\gamma_0^2 f(k)^2 + \Delta_1^2)) - \gamma_0^2 f(k)^2(\gamma_0^2 f(k)^2 - \Delta_1^2)^2 = 0 \quad (2.34)$$

On the other hands, in the ABC TLG Hamiltonian and the secular equation, the energy difference $2\Delta_1$ between the top and bottom layers breaks the inversion symmetry,

$$H_{ABC} = \begin{bmatrix} A_1 & B_1 & A_2 & B_2 & A_3 & B_3 \\ B_1 & -2\Delta_1 & -\gamma_0 f(k) & 0 & 0 & 0 \\ A_2 & -\gamma_0 f(k) & -2\Delta_1 & \gamma_1 & 0 & 0 \\ B_2 & 0 & \gamma_1 & 0 & -\gamma_0 f(k) & 0 \\ A_3 & 0 & 0 & -\gamma_0 f(k) & 0 & 0 \\ B_3 & 0 & 0 & 0 & \gamma_1 & 2\Delta_1 \\ & & & & & -\gamma_0 f(k) \\ & & & & & & 2\Delta_1 \end{bmatrix} \quad (2.35)$$

det

$$\begin{bmatrix} A_1 & B_1 & A_2 & B_2 & A_3 & B_3 \\ A_1 & -E - 2\Delta_1 & -\gamma_0 f(k) & 0 & 0 & 0 \\ B_1 & -\gamma_0 f(k) & -E - 2\Delta_1 & \gamma_1 & 0 & 0 \\ A_2 & 0 & \gamma_1 & -E & -\gamma_0 f(k) & 0 \\ B_2 & 0 & 0 & -\gamma_0 f(k) & -E & \gamma_1 \\ A_3 & 0 & 0 & 0 & \gamma_1 & -E + 2\Delta_1 \\ B_3 & 0 & 0 & 0 & 0 & -\gamma_0 f(k) & -E + 2\Delta_1 \end{bmatrix} = 0 \quad (2.36)$$

where $V_1 + V_2 + V_3 = 0$ and $\Delta_2 = 0$. In the both ABA and ABC TLG, the analytic forms of the eigenvalues do not exist under the presence assumption. Thus we make plots assuming that the energy differences Δ_1 in ABA TLG and ABC TLG are $0.5\gamma_1$ and $0.1\gamma_1$ as shown in figure 2.10.

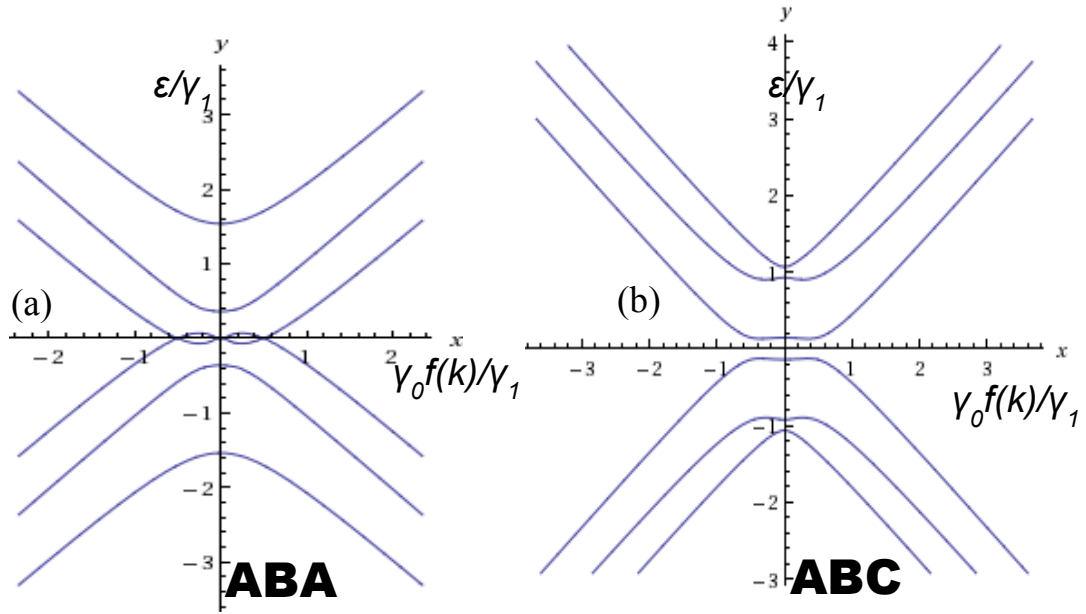


Figure 2.10: Energy band structure of TLG in the layer asymmetry. (a) Band structure of ABA trilayer and (b) from the tight binding calculation considering $\Delta_1 = 0.5\gamma_1$ and $0.1\gamma_1$

Figure 2.10a shows that the energy band of ABA TLG has a small overlap at the vicinity of K point whereas the potential difference between outmost layers in ABC TLG leads to opening of an energy gap^{12,14} between the conduction and valence bands similar to BLG in the simplest tight binding calculation.

Reference

- 1 Saito, R., Dresselhaus, G. & Dresselhaus, M. S. *Physical properties of carbon nanotubes*. Vol. 4 (World Scientific, 1998).
- 2 Kittel, C. Introduction to solid state physics (4th edition). *Introduction to solid state physics (4th edition)*, xv+766 pp. (1971).
- 3 Raza, H. *Graphene nanoelectronics: Metrology, synthesis, properties and applications*. (Springer, 2012).
- 4 Novoselov, K. S. *et al.* Two-dimensional gas of massless Dirac fermions in graphene. *Nature* **438**, 197-200, doi:10.1038/nature04233 (2005).
- 5 Dresselhaus, M. S. & Dresselhaus, G. Intercalation compounds of graphite. *Advances in Physics* **51**, 1-186, doi:10.1080/00018730110113644 (2002).
- 6 McCann, E. & Koshino, M. The electronic properties of bilayer graphene. *Reports on Progress in Physics* **76**, 1-28, doi:10.1088/0034-4885/76/5/056503 (2013).
- 7 Mañes, J. L., Guinea, F. & Vozmediano, M. A. H. Existence and topological stability of Fermi points in multilayered graphene. *Physical Review B* **75**, 155424 (2007).
- 8 Sachs, B., Wehling, T. O., Katsnelson, M. I. & Lichtenstein, A. I. Adhesion and electronic structure of graphene on hexagonal boron nitride substrates. *Physical Review B* **84**, 195414 (2011).
- 9 Chen, Z.-G. *et al.* Observation of an intrinsic bandgap and Landau level renormalization in graphene/boron-nitride heterostructures. *Nat Commun* **5** (2014).
- 10 McCann, E. Asymmetry gap in the electronic band structure of bilayer graphene. *Physical Review B* **74**, 161403 (2006).
- 11 Lei, J. *et al.* Quantum Transport and Field-Induced Insulating States in Bilayer Graphene pnp Junctions. *Nano Letters* **10**, 4000-4004 (2010).
- 12 Koshino, M. & McCann, E. Gate-induced interlayer asymmetry in ABA-stacked trilayer graphene. *Physical Review B* **79**, 125443 (2009).

- 13 Koshino, M. & Ando, T. Orbital diamagnetism in multilayer graphenes: Systematic study with the effective mass approximation. *Physical Review B* **76**, 085425 (2007).
- 14 Zou, K., Zhang, F., Clapp, C., MacDonald, A. H. & Zhu, J. Transport Studies of Dual-Gated ABC and ABA Trilayer Graphene: Band Gap Opening and Band Structure Tuning in Very Large Perpendicular Electric Fields. *Nano Letters* **13**, 369-373 (2013).

Chapter 3 : Device Fabrication

All the devices presented in this thesis are fabricated using graphene sheets that are isolated via mechanical exfoliation from Kish graphite onto Si/SiO₂ substrates with 3M scotch tapes¹. Flakes up to a few μm in size can be readily obtained.

3.1: Identification of number of layers and stacking order

After mechanical exfoliation, we search for graphene sheets with the desired shape, thickness and stacking order. For example, for dual-gated suspended devices, flakes with rectangular shapes and widths $\sim 1.3 - 1.6 \mu\text{m}$ are selected for fabrication.

To determine the number of layers, the flakes are first identified by color contrast in the optical microscope. Figure 3.1a shows the optical images of mono-, bi- and tri-layer graphene, whose colors becomes darker with increasing thickness. Quantitatively, we use the relative green shift (RGS) to determine the number of layer. After capturing the optical image by a high-resolution camera, we use an image manipulation software (such as Photoshop) to acquire the green channel components of the graphene flake G_g and of the nearby SiO₂ substrate G_s :

$$\text{RGS} = (G_s - G_g) / G_s \quad (3.1)$$

Figure 3.1a displays several graphene sheets with different thicknesses and measure RGS values². Typically the ranges of RGS values for monlayer, bilayer, trilayer and tetralayer graphene are 0.03–0.045, 0.05–0.068, 0.073–0.085, and 0.09–0.11, respectively, as

shown in figure 3.1b. Note that there is a spread in RGS values for each thickness, due to the variations in the green channel values of the substrate and the illumination intensity.

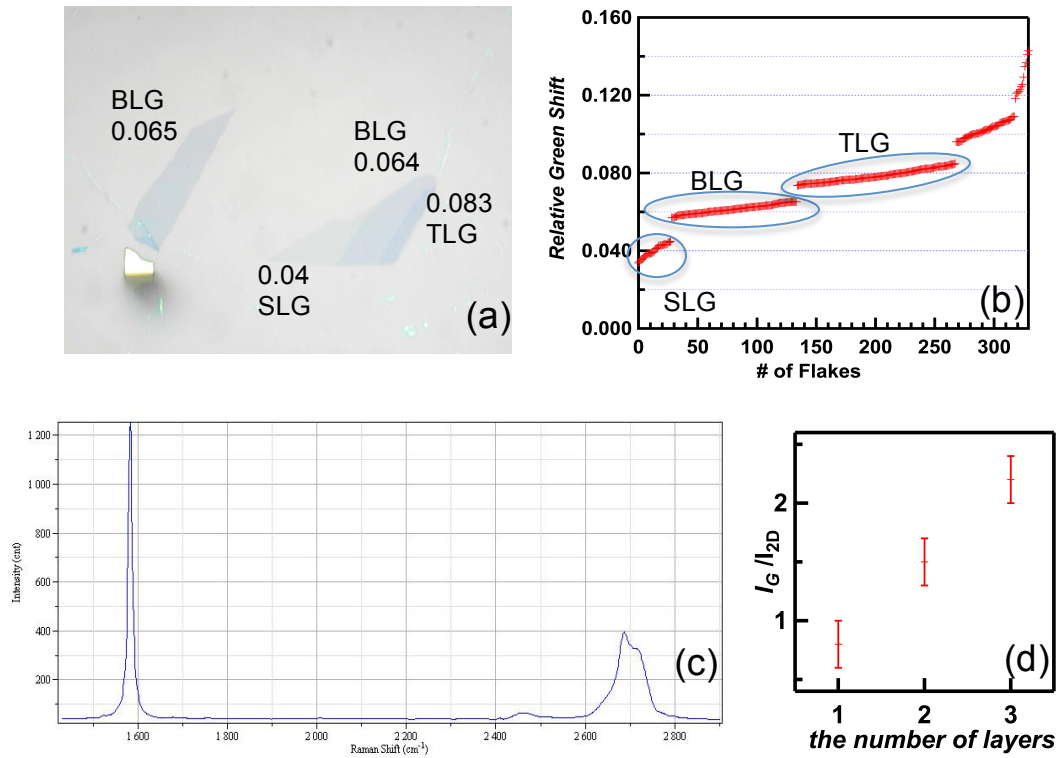


Figure 3.1: Identification of the number of layers. (a) Optical images of SLG, BLG and TLG. (b) The values of relative green shift channel for SLG, BLG and TLG (c) The Raman spectroscopy of TLG (d) The intensity ratio (I_G/I_{2D}) of SLG, BLG and TLG.

Nevertheless, the RGS value provides an excellent preliminary measurement of the number of layers, which will be further confirmed by the G/2D peak ratio of Raman spectroscopy³, the magnitude of annealing current and quantum Hall effect (QHE) transport data. Since Raman spectroscopy is sensitive to the geometrical structure of graphene⁴, it can provide the method for determining the layer thickness of graphene.

Here we measure the intensity ratio I_G/I_{2D} where I_G and I_{2D} are for G and 2D bands at $\sim 1590\text{cm}^{-1}$ and 2700cm^{-1} . Empirically, the intensity of the ratio scales linearly as the number of layers, as shown in figure 3.1d. For our substrates and 532 nm laser, the ratios of single layer graphene (SLG), bilayer graphene (BLG) and trilayer graphene (TLG) are 0.8, 1.5 and 2.2, respectively.

3.2: Stacking Order

In a few layer graphene (FLG), stacking order provides a unique “knob” for tuning the electronic properties, thus attracting much attention from theorists and experimentalists. The energy structures are calculated with the density functional theory on each stacking orders⁵. For example, there are in principle infinite number of stacking orders in Bilayer Graphene, depending on the relative angles between the top and bottom layers, though it is known that AB-stacking has the lowest energy. Within the density functional theory with the local density approximation, the energy of AA-bilayer in per atom is calculated to be 10 meV/atom higher than that of AB-bilayer.⁵ Therefore the exfoliated bilayer graphene sheets are most likely AB-stacked.

Trilayer has two types of stable configuration: ABA or Bernal stacking, and ABC or rhombohedral stacking. For both stacking orders, the bottom two layers are Bernal-stacked, in which one sublattice of the middle layer is located above the center of the hexagons of the bottom layer. In ABA trilayer, the third layer is directly above the lowest layer, whereas in ABC trilayer, the top layer is shifted by a lattice constant, so that the top layer and the lowest layer form Bernal stacking as well. ABC trilayer is metastable, and is

calculated to have slightly higher energy (0.18meV/atom)⁵ than ABA trilayer. Thus only ~16% of the exfoliated graphene sheets are found to be rhombohedral stacked, and it is crucial to identify the stacking order of a given trilayer sheet before fabrication.

To determine the stacking order, we use Raman spectroscopy. For instance, due to the different electronic structure that gives rise to a double resonance process⁶, the 2D peak of ABC trilayer graphene is more asymmetric than that of ABA trilayer. Figure 3.2 displays the Raman spectra of trilayer graphene of these two different stacking orders.

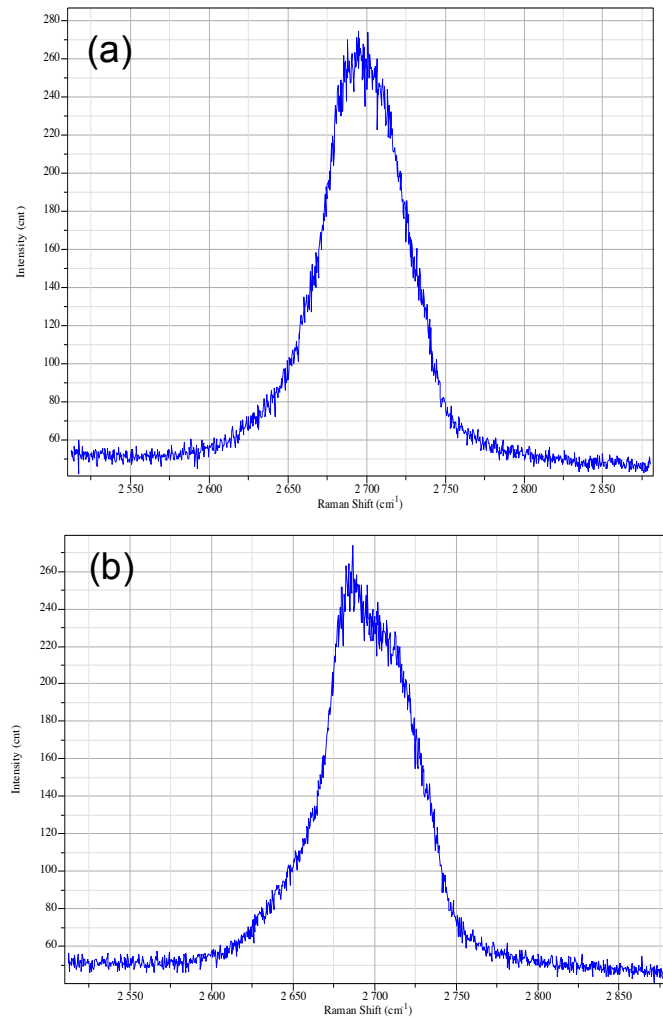


Figure 3.2: Raman spectroscopy of (a) ABA-stacked TLG and (b) ABC-stacked TLG in the 2D mode using 532 nm laser.

3.3 Device Fabrication

After ascertaining the thickness and stacking order of the desired sheets, we start the device fabrication by first putting down the number matrix alignment marks and extra align-marks on the chip; the latter is very important to control precisely the distance between the source-drain electrode and the top-gate.

Table 3.1: The fabrication procedure of extra alignment mark

	Procedure	Note
1. Normal alignment	-Spin coat with MMA and PMMA (4000 rpm and 300 acceleration) -Bake at 180 Celsius for 10min for each layer. -Use EBL and is developed by MIBK(60s) and IPA(30s)	1440 × 1440 (mm × mm) alignment matrices
2. Extra alignment mark	-From procedure#1, without adding a new resistor, simply put an extra alignment mark nearby the selected graphene. It will especially help to make a pattern of the top-gate with high resolution.	
3. Metal deposition	-deposit the Cr(10nm) + Au(70nm) at 2.5~3.3 A/s rate.	
4. Lift off	- Immerse in acetone at ~60°C for 2~3 hours. - Gently blow-dry acetone with N ₂ gas	

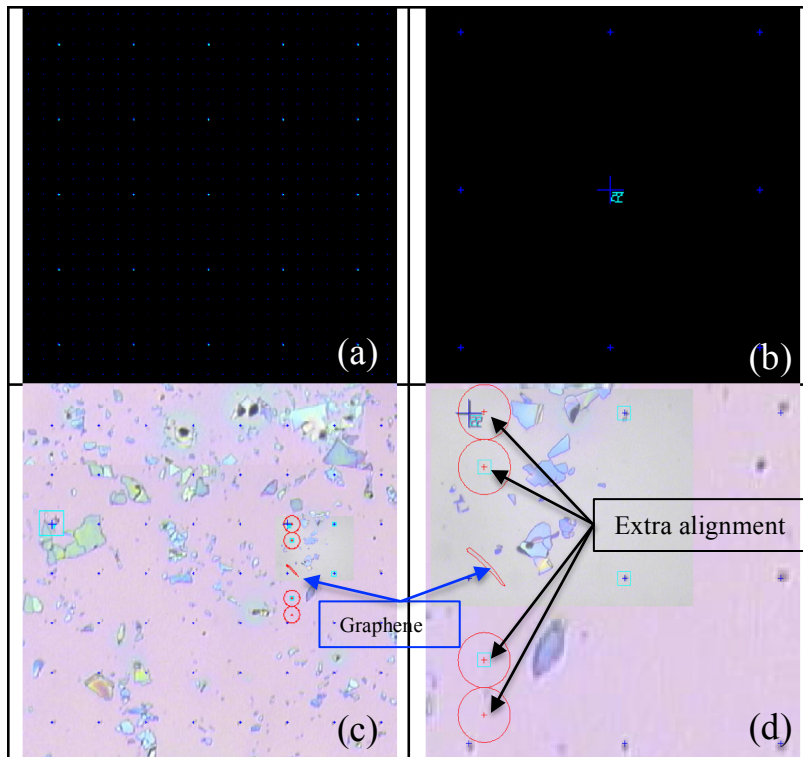


Figure 3.3: Alignment mark of the normal matrix and extra matrix (a) 1440×1440 (mm \times mm) alignment matrices (b) the number matrices every 300mm (c) extra alignment nearby graphene (d) High resolution image of extra alignment

3.4: Suspend Top gate and the electrode fabrication

Graphene consists of only a single atomic layer of the carbon. Deposition of top gate materials may introduce defects, dopants or additional scattering sites, which preclude access to many fascinating physical phenomena. Previously, materials such as electron beam resists or alternating layers of NO_2 , trimethylaluminum and Al_2O_3 have been used as the dielectrics for local gates. We developed a multi-level lithography technique to fabricate ‘air-bridge’-styled top gates⁷, in which a metallic bridge is

suspended across a portion of the graphene sheet, with the vacuum acting as the dielectric.

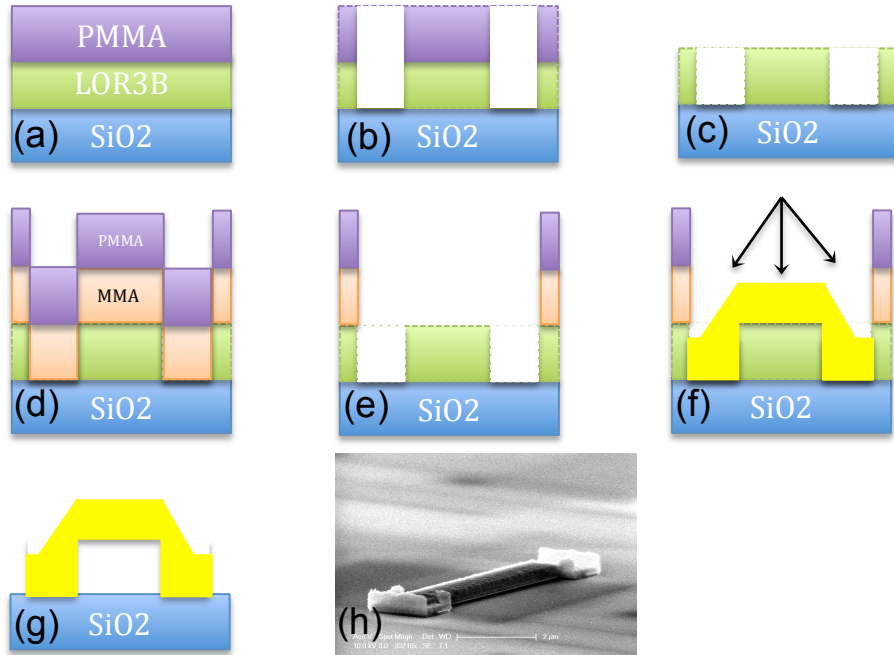


Figure 3.4: Top gate fabrication process (a) Spin coat LOR and PMMA (b) EBL pattern for step 1-e (c) Remove PMMA (d) Spin coat MMA and PMMA (e) EBL pattern for step 2-e (f) Deposit metal (g) Life-off metal (f) SEM image of the top gate

First of all, LOR3B and polymethylmethacrylate (PMMA) resists are spun and baked on SiO₂ chip at 190°C and 180°C, respectively. The detail recipe is shown in table 3.2. We then use an electron beam to expose the pattern for the first level design. The chips are developed by methylisobutylketone (MIBK) and MF319. Subsequently, acetone solution is used to remove the top PMMA layer and while LOR is left as shown in figure 3.4c. New MMA and PMMA layers are spun and baked on top of the LOR layer for a

second pattern which is the air bridge to be exposed by electron beam as shown in figure 3.4e. The chips are developed in MIBK, leaving windows for the top-gate^{8,9}. We then deposit metal (Cr and Au) by three angles electron beam evaporation at -45, 45 and 0 degree. Based on our experience, the combination of Cr and Au reinforces the top gate structure. To fabricate electrodes, the general electron beam lithography (EBL) process from step 6 to step 9 in Table 3.2 is repeated.

The substrate supported device is immersed in HF for 70 second to partially remove the SiO₂ layer. Note that etching more than 90 second might cause gate-leakage due to over-etching. Table 3.2 summarizes the detailed device fabrication procedure and notes.

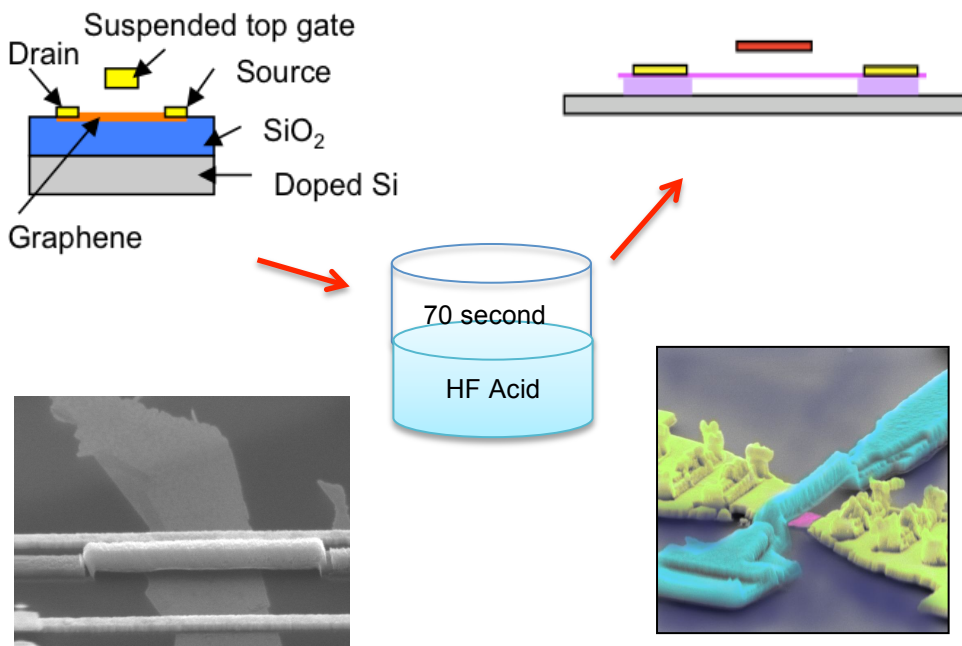


Figure 3.5: Schematic of etching proces

Table 3.2 Procedure of the device fabrication

1. top-gate design (1-e)	<ul style="list-style-type: none"> -Spin coat LOR3B (4000 rpm and 300 acceleration) and bake at 190 Celsius for 5min. -Spin coat PMMA (4000 rpm and 300 acceleration) and bake at 180 Celsius for 10min. - EBL exposure for electrode and anchors of the top gate (figure 3.4b) and develop with MIBK(60s), IPA(30s), MF319(3~4s) and DI water(5min) - Gently remove DI water with N₂ gas. - Immerse in acetone for 10min to remove the PMMA layer 	<p>The height of Top-gate depends on the thickness of the LOR resistor. There are three LOR resistors;</p> <p>LOR3B : ~300nm and developing time 3~4s</p> <p>LOR1A : ~100nm and developing time 15s</p> <p>LOR0.7A : ~70nm and developing tie 15s</p>
2. top-gate design (2-e)	<ul style="list-style-type: none"> -Spin coat MMA and PMMA (4000 rpm and 300 acceleration) and bake at 180 Celsius for 10min. - EBL exposure for the top gate (figure 3.4e) and develop with MIBK(60s) and IPA(30s). 	
3. Metal deposition	<ul style="list-style-type: none"> - Three steps metal deposition -45, 45, 0 angle as shown in figure 3.4f with following the thicknesses: -1st step :Cr(10nm) + Au (150nm) -2nd step :Cr(10nm) + Au (180nm) -3rd step : Cr(15nm) + Au (120nm) 	<ul style="list-style-type: none"> - Keep the temperature within 50 Celsius and deposit the rate at ~2.5 ~3.3 A/s
4. Lift off	<ul style="list-style-type: none"> - Immerse in the PG remover for 10~15 hours at around 60 Celsius. Afterwards, gently squirt with the pipet inside the PG-remover beaker to remove metal pieces. - Dilute the PG remover with high-quality IPA seven times. -Device is then transferred with the plastic basket 	
5. CPD	<ul style="list-style-type: none"> -High quality IPA is then dried by the critical point dryer machine for ~50min to ensure structural integrity. 	

6. O ₂ gas annealing	-Bake the sample in quartz tube at 300 Celsius flowing O ₂ with 0.4 rate for 1 hour.	Quartz tube might be necessary to clean before gas annealing with 990 Celsius in a vacuum.
7. Source and drain electrode (3-e)	-Spin coat MMA and PMMA (4000 rpm and 300 acceleration) and bake 180 Celsius for 10min. - EBL exposure and develop with MIBK(60s) and IPA(30s).	- Doses test for source and drain electrode is required to prevent the over-pattern and under-pattern.
8. Metal deposition	-Deposit the Cr(10nm) + Gold(120nm) at a 2.5 – 3.3 A/s rate.	
9. Lift off	-Dip in Acetone at 65 Celsius - Gently squirt with a pipet in the acetone to remove the metal covering the chip. - The device is then transferred with the plastic basket -Dilute 7 times with high quality IPA	
10. Wet etching	- Immerse 70s in BOE solution -Dilute 7 times with DI water -Dilute 7 times with high quality IPA	
11. CPD	High quality IPA is then evaporated by the critical point dryer machine for ~50min.	

Depending on the purpose of physics, the devices' top gate geometry is variously achieved such as global top-gate, local top-gate and two split-top gates. The length of a suspended graphene device is typically limited to <1.4mm, otherwise it might be collapsed or break during the current annealing. This constraint should be considered when the various top-gates are designed, as it impacts the space between the electrodes and top-gate, between top-gates in split top-gate. After several design tests, the protocol for the global top-gate, local top-gate and two split-top gates without any shortage between the patterns as shown in figure 3.5.

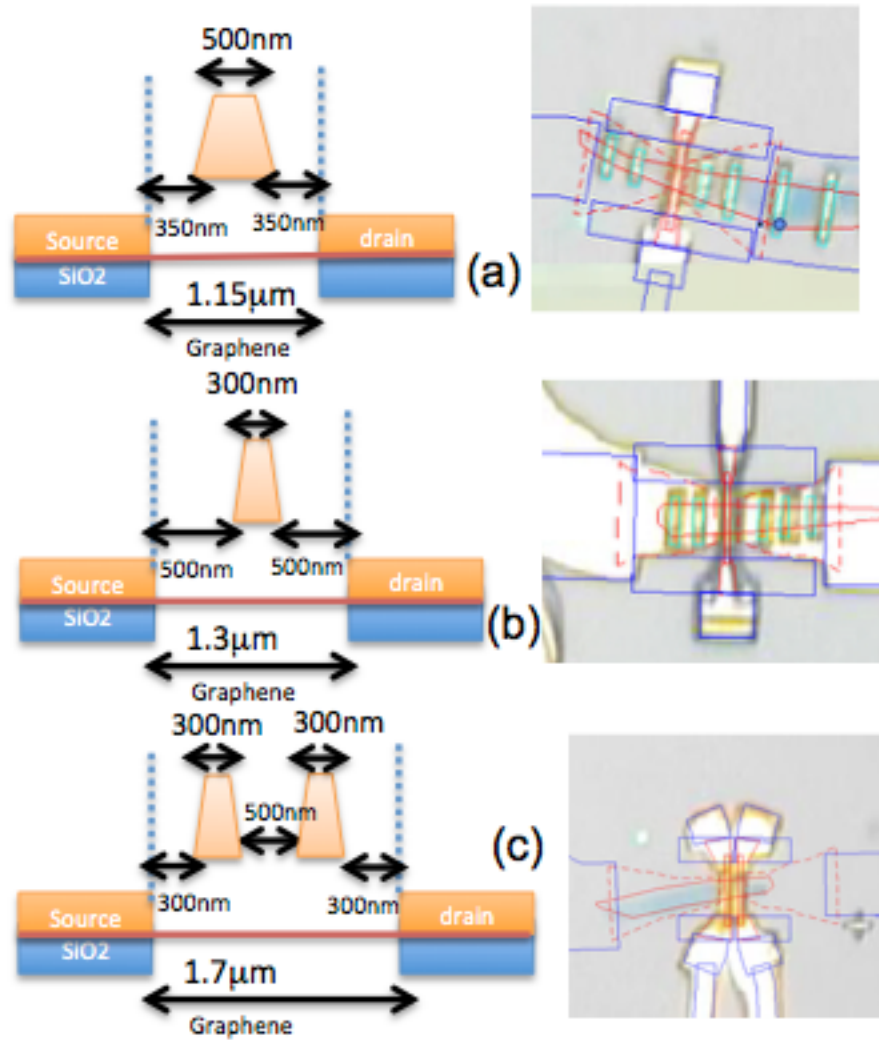


Figure 3.6 :Top gate protocol (a) Global top-gate design (b) Local top-gate design (c) Split two top-gate design

3.5: Characterization of Device

The devices subject to the above fabricating process are chemically contaminated due to the presence of resist residues and impurities. Thus, to achieve high mobility samples, certain cleaning procedures are required to remove the contaminants. Generally one or both of two annealing procedure are adopted: gas annealing and current annealing. Gas annealing entails heating the devices in flowing oxygen at 300°C in a furnace for one hour in step 6 of the device fabrication. Using this form of treatment, we expect to strengthen the top gate structure and improve the contact between the graphene and the electrode.

Current annealing

The most dramatic change that we have introduced in purifying 2D graphene samples is current annealing, which consists of applying a large DC voltage across the graphene sheet and generating significant Joule heating. Indeed, this is the same principle as the lighting and heating of a light bulb when electricity flows through its filament. Induced by the Joule heating, the temperature at the center of graphene can be as high as 600-1000°C, thus driving or burning off impurities.

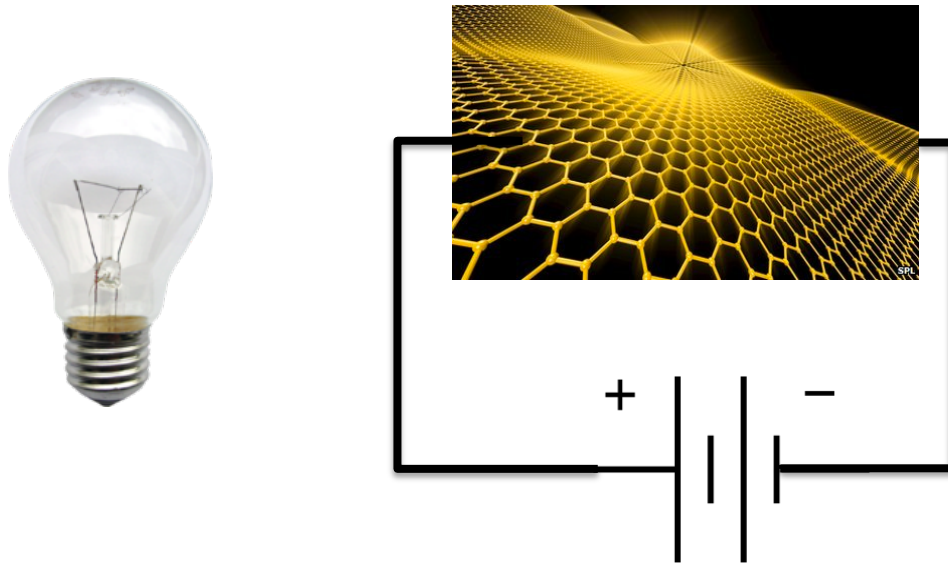


Figure 3.7: Schematic images of light bulb and graphene bulb

Setup and general procedure

As shown in figure 3.7, the circuit for current annealing uses a DAQ board to supply the output DC voltage to the source terminal of the device and measures the induced current from the drain channel that is amplified by an Ithaco current preamplifier. The sensitivity in the Ithaco preamplifier during annealing is set to 10^{-3} A/V. A Keithley 2400 source meter is used to apply back-gate or top-gate voltage; it also displays the leakage current between the device and the gate. Generally a reading of $> 0.001\mu\text{A}$ suggests that the suspended membrane is buckled towards the gate and is close to the point of device failure, thus no higher gate voltage should be applied.

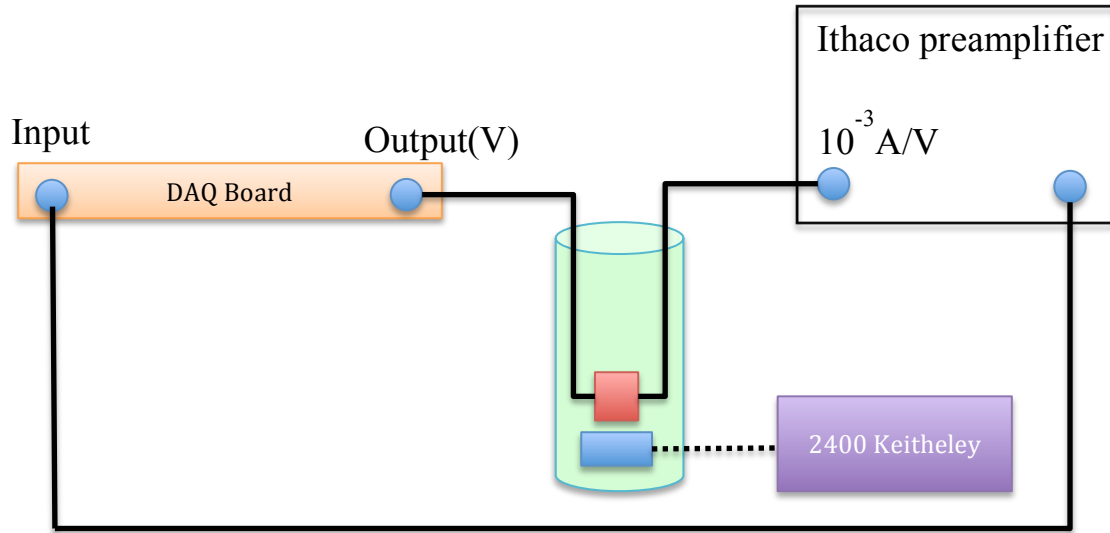


Figure 3.8: Schematic of current annealing circuit

Procedure

Current annealing is performed at liquid helium temperatures (1.6 ~ 4.2K) inside a cryogenic fridge and its effectiveness is checked by the device's conductance G vs gate voltage V_g . Before the first annealing process, the $G(V_g)$ response of the device is measured to establish the initial quality of the devices. Usually this plot shows a nearly linear curve with no visible Dirac point, presumably due to the scattering from contaminants. To perform current annealing, we ramp the bias voltage at 20~30mV/s in the beginning of each sweeping and 5~10mV/s in the end of each sweeping and measure the current, and closely monitor the current-voltage (I - V) curve. For instance, the slope of the I - V curve, *i.e.* the sample conductance, changes during annealing in figure 3.8. After successful annealing, the overall conductance drops and a sharp V-shaped $G(V_g)$ curve ensues, as shown in figure 3.8, due to the desorption of contaminants.

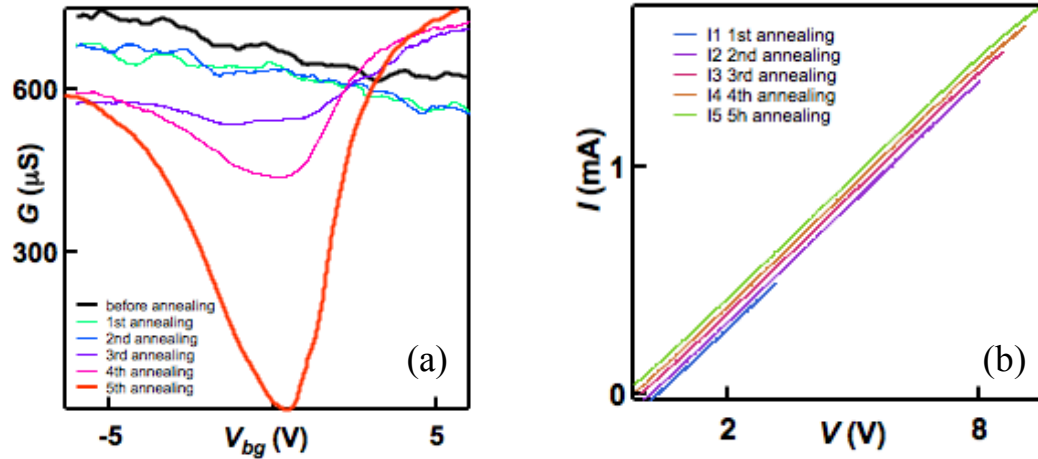


Figure 3.9: Annealing result of TLG (a) $G(V_{bg})$ after each cycle of annealing (b) $I-V$ curve of annealing

The strongest indication that the optimal state has been reached is when $I-V$ curve starts to saturate the $G(V_g)$ response adopts a sharp V-shape centered at $V_{bg} \sim 0$ with high field effect mobility. If the annealing current overshoots some critical current value, then it is possible to over-anneal, where the device's field effect mobility decreases, and the charge neutrality point shift to the electron side as shown in figure 3.10. Thus it is crucially important to stop when the optimal annealing current has been reached. This is typically determined by monitoring the following 3 metrics: the $I-V$ curve, the instantaneous sample space temperature and $G(V_g)$ response. Since the current annealing procedures are different for graphene sheets of different thickness, we will describe in

following section details for current annealing for bilayer and trilayer graphene. (Single layer graphene does not always display the characteristic saturation in I-V curves, thus is difficult to anneal.)

Current Annealing of BLG

BLG is twice as thick as SLG and is expected to withstand a higher current density. The sample space temperature is a good indicator that Joule heating is effective: it should reach 3-4K during current annealing if the initial temperature is ~ 1.6 K. Note that this is the general rule of thumb; the final temperature of the sample space also depends on the sweeping rate of voltage bias. After each annealing cycle, the annealing effect is clearly evident by observing changes in the $G(V_g)$ response. The saturated I-V curve behavior is also a clear indication of the optimal state. Generally speaking, depending on the sample's length, width and shape, the optimal annealing current has a range of 1-1.5 mA for a device of 1-1.6 μ m in width.

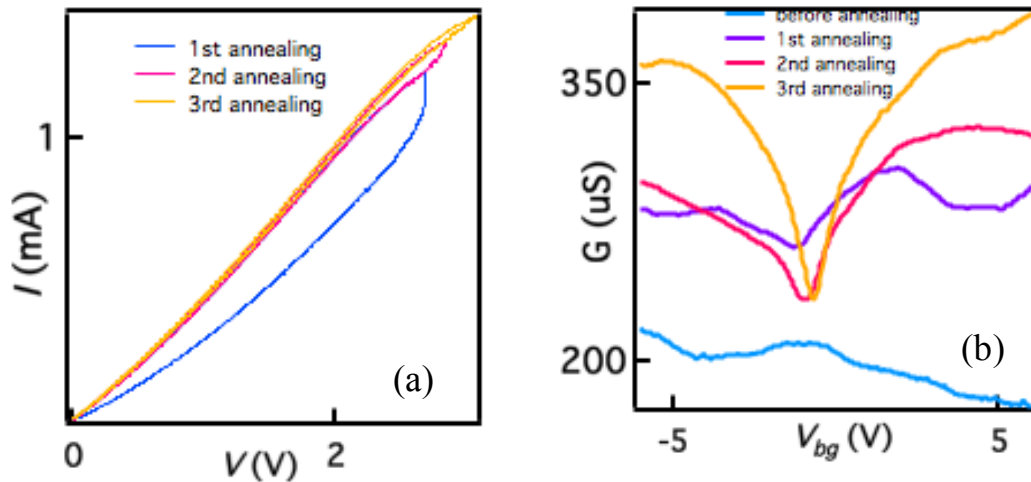


Figure 3.10: Annealing result of BLG (a) I - V curve of annealing (b) $G(V_{bg})$ after each cycle of annealing. Note that initially, the overall conductance is low indicating that the contact is poor. However, the contact improves considerably during annealing, as evidenced by the sudden increase in current during 1st annealing.

Current Annealing of TLG

Compared to BLG, TLG is thicker and withstands even higher current. During annealing, the sample space temperature quickly increases from ~ 2 - 4 K to 4 - 6 K for a successful process. The I - V inflection point is not as clear as the current saturation is more smooth and gradual as shown in figure 3.8. The typical annealing current is 1.4 - 1.6 mA per μm .

Over-annealed state

We typically consider optimal annealing is reached and stop annealing if the sample has high field-effect mobility (say more than $15,000$ cm^2/s), and if the charge neutrality point is near 0 V (thus indicating minimal extrinsic doping), and if clear

plateaus in the quantum hall (QH) regime. Over-annealed devices are likely deformed or damaged, with the charge neutrality point shifting away from 0V, decreasing mobility and less resolved QH plateaus.

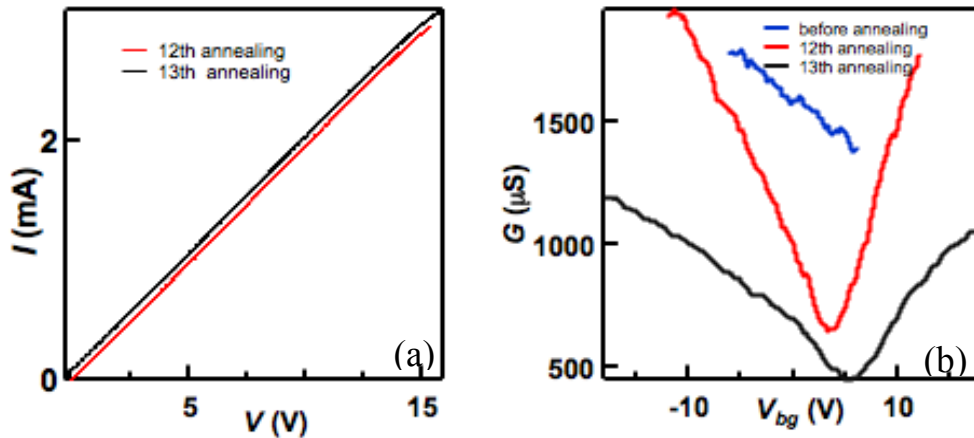


Figure 3.11: Overannealed device (a) I - V curve of annealing (b) $G(V_{bg})$ after each cycle of annealing. After the 13th annealing cycle, the dirac point shifts away from 0V and the mobility decreases.

Dependence on Refrigerators

It is possible for the sample to retain high mobility without re-annealing, if it has been previously annealed and thermally cycled. However, if it is exposed to air for a prolonged period of time, another round of current annealing is required. If the annealing is performed in the same refrigerator system, one can use the previous parameters (such as annealing current) for the annealing procedure. However, if the device is annealed in a different fridge, the parameters will likely change, since the line resistances and the refrigerator's cooling power may be different. Here, we compare the annealing procedure

of the helium Oxford fridge with the fridge at the National High Magnetic Field Lab in Florida in the following section.

Oxford He3 fridge in the lab

In the Oxford He3 refrigerator, the sample is placed in vacuum in the inner vacuum chamber (IVC) which is vacuum isolated from the He3 pot. The applied DC voltage is usually very high since each electrical line has a 2.2-k Ω series resistance. If >10V bias voltage is needed, an analog voltage amplifier is used to amplify the signal from the DAQ board. In this case multiplication factor for the voltage parameter in the Mezurit I software should be 20.

He3 fridge at NHML

For the He3 refrigerators at National High Magnet Field Laboratory (NHMFL), the sample is placed in He3 vapor with more cooling power than our Oxford fridge, and current annealing is not as effective. It is therefore recommended to vaporize the He3 liquid prior to annealing by heating the He3 pot. The annealing current in the Florida fridge is typically higher than that in our Oxford fridge.

The above serves as a general guideline for the current annealing procedure. The exact annealing current depends on sample geometry and impurities introduced by fabrication. Thus the optimal current value may vary from sample to sample. With care and luck, successful current annealing process allows us to explore few-layer graphene devices in the clean limit.

Reference

- 1 Novoselov, K. S. *et al.* Electric Field Effect in Atomically Thin Carbon Films. *Science* **306**, 666-669 (2004).
- 2 Craciun, M. F. *et al.* Trilayer graphene is a semimetal with a gate-tunable band overlap. *Nat Nano* **4**, 383-388 (2009).
- 3 Ferrari, A. C. *et al.* Raman Spectrum of Graphene and Graphene Layers. *Physical Review Letters* **97**, 187401 (2006).
- 4 Wall, M. *The Raman Spectroscopy of Graphene and the Determination of Layer Thickness*, (2011).
- 5 Aoki, M. & Amawashi, H. Dependence of band structures on stacking and field in layered graphene. *Solid State Communications* **142**, 123-127, doi:10.1016/j.ssc.2007.02.013 (2007).
- 6 Lui, C. H. *et al.* Imaging stacking order in few-layer graphene. *Nano Lett.* **11**, 164-169 (2011).
- 7 Liu, G., Velasco, J., Bao, W. & Lau, C. N. Fabrication of graphene p-n-p junctions with contactless top gates. *Applied Physics Letters* **92**, 203103, doi:10.1063/1.2928234 (2008).
- 8 Liu, G., Velasco, J., Bao, W. Z. & Lau, C. N. Fabrication of graphene p-n-p junctions with contactless top gates. *Appl. Phys. Lett.* **92**, 203103 (2008).
- 9 Velasco, J., Liu, G., Bao, W. Z. & Lau, C. N. Electrical transport in high-quality graphene pnp junctions. *New J. Phys.* **11**, 095008 (2009).

Chapter 4 : Band gap and overlap in bilayer and trilayer graphene

Graphene¹⁻⁴ is a unique two dimensional electron system with compelling material properties, such as unparalleled breaking strength⁵, chiral charge carriers, ultra-high electron mobility and thermal conductivity⁶, unprecedented current carrying capability, optical transparency⁷⁻⁹, chemical stability and compatibility with CMOS technology. These properties make graphene the most popular material for exploring novel phenomena and next generation electronic materials. However, what makes single layer graphene (SLG) such a great and unusual electrical conductor, i.e. the Dirac dispersion relation, is also responsible for its critical drawback – graphene is gapless and cannot be directly applied to digital electronics. To date band gap engineering of SLG remains the grand challenge in this area. Recently, few-layer graphene have also piqued the interest of scientific and technological communities, since they share SLG's attractive material properties but not the weakness, as their electronic spectra are conducive (and even unstable) to gap opening. These gaps may arise from single particle physics in the presence of an out-of-plane electric field that breaks the inversion symmetry.

In this chapter, I will discuss the external electric effect on the electrical properties of bilayer and trilayer graphene¹⁰. Section 4.1 describes device characterization. Section 4.2 presents the electric field-induced asymmetry gap in BLG within the tight binding model and Section 4.3 its application to transport data. Section 4.4 discusses the band overlap in ABA trilayer graphene (TLG) in the presence of an out-of-plane electric field.

4.1: Device characterization and experimental procedure

Bilayer and trilayer graphene sheets are exfoliated from bulk graphite onto Si wafers covered with 300 nm of SiO₂. The number of layers are identified by color contrast in the optical microscope, and confirmed by Raman spectroscopy¹¹. Specifically, we find that the layer number is proportional to the intensity of the green channel in the sheet's RGB image¹², and to the ratio I_G/I_{2D} , where I_G and I_{2D} are the intensities of the Raman shift for the G and $2D$ bands at 1580 cm⁻¹ and 2700 cm⁻¹, respectively in figure 4.1a.

After a desirable sheet is located, a multi-level electron beam lithography process is used to deposit electrodes and fabricate top gates that are suspended ~150-300 nm above the substrates. Details of top gate fabrication are described elsewhere¹³. After the last lithography step, the device is immersed in 49% buffered HF solution for 70s to etch away ~ 180-200 nm of SiO₂, in order to release the graphene sheet from the SiO₂ substrate. The device is then rinsed in deionized water and dried using a critical point dryer. An SEM image of a finished device is shown in figure 4.1a inset. All devices have source-drain separation ~ 1 – 1.5 μm, and width 1.3 – 1.6 μm.

The devices are measured in a pumped He³ refrigerator. An as-fabricated device typically has very low mobility, often <500 cm²/Vs, presumably due to the presence of resist residues and adsorbed molecules that dopes the graphene sheets and provide extra scattering sites. Device mobility can be improved dramatically by current annealing¹⁴, in which Joule heating is used to drives off resist residue and adsorbed species. We found that optimal annealing results are reached when the current-voltage (I - V) characteristic

start to saturate, typically at ~ 0.2 mA/ μm /layer. A simple estimate shows that the center of the graphene reaches ~ 600 - 1000 K at such a current density. Moreover, all current annealing are performed at low temperature ($T=1.6\text{K}$), where the sample space is effectively cryo-pumped. A thermally cycled sample, even without breaking vacuum, almost always reverts to a low mobility state; the high mobility can, however, be recovered via annealing at low temperature, usually with previous parameters. After successful current annealing, the devices are measured using standard lock-in techniques. All measurements are performed at temperature $T=260$ mK, unless otherwise specified.

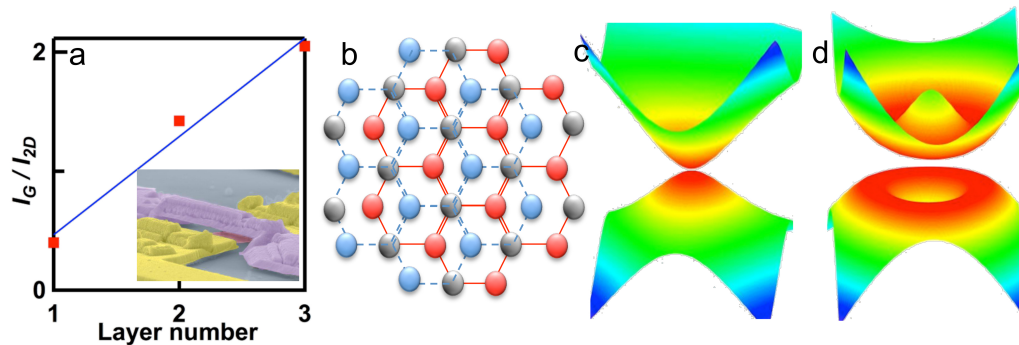


Figure 4.1: (a) Ratio of the intensities of G and $2D$ bands in graphene's Raman spectrum as a function of number of layers. Inset: SEM image of a dual-gated suspended BLG device. (b). Atomic structures of BLG. Red atoms belong to the sublattice A of the top layer, and blue atoms to sublattice B of the bottom layer. The gray atoms are vertically stacked; they hybridize to form high energy bands and can be ignored in low energy approximation. (c-d). Band structure of BLG at zero and finite E_{\perp} , respectively.

4.2: Gap in bilayer graphene

The honeycomb lattice of SLG consists of two intersecting sublattices A and B, and adjacent atoms belong to different sublattices. In BLG, the two layers are stacked in

Bernal registry, *e.g.* sublattice A of the top layer is located above the center of the hexagons of the bottom layer, and sublattice B is directly above sublattice A of the bottom layer in figure 4.1b. The stacked atoms (B1 and A2) hybridize to form higher energy bands that are separated from the lowest band by $t_{\perp} \sim 0.3$ eV, the interlayer hopping parameter.^{4,15} Thus, in the low energy approximation, BLG's Hamiltonian only consists of contributions from sublattices A1 and B2, thus the layer and sublattice indices are equivalent.

From tight-binding calculations, the charge carriers in BLG behave as massive Dirac fermions, and are described by a combination of the Schrödinger and Dirac equations, with energy given by^{4,15}

$$E_{\pm}(k) = \left[e^2 V_{\perp}^2 + \hbar^2 v_F^2 k^2 + t_{\perp}^2 / 2 \pm \left(4e^2 V^2 \hbar^2 v_F^2 k^2 + t^2 \hbar^2 v_F^2 k^2 + t_{\perp}^4 / 4 \right)^{1/2} \right]^{1/2} \quad (4.1)$$

where V_{\perp} is the electric potential across the bilayer, e the electron charge, \hbar is Planck's constant, $v_F \sim 10^6$ m/s is SLG's Fermi velocity, $t_{\perp} \sim 3$ eV is the nearest neighbor hopping, $t \sim 0.4$ eV is the interlayer hopping energy, and the \pm signs refer to the conduction and valence bands, respectively. For $V_{\perp} = 0$ and at low energies, BLG has a parabolic dispersion with zero band gap in figure 4.1c, $E = \pm \hbar^2 k^2 / 2m^*$, where

$m^* = t_{\perp} / 2v_F^2 \sim 0.03m_e$ is the effective mass of charge carriers¹⁶⁻¹⁸ and m_e is electron rest mass in figure 4.1. For $V_{\perp} \neq 0$, the band structure adopts a "Mexican-hat" shape, with a

band gap $\Delta = \frac{t_{\perp} V_{\perp}}{\sqrt{t_{\perp}^2 + V_{\perp}^2}}$ in figure 4.1d. We note that V_{\perp} is the screened internal potential

between the layers, and is not simply given by $E_{\perp} d$, where E_{\perp} is the applied external field

and $d=0.34$ nm is the interlayer spacing. Generally, V_{\perp} is reduced from $E_{\perp}d$ by a factor of 5-10 at low E_{\perp} and by a factor of ~ 2 at large E_{\perp} .

The most interesting consequence of equation. 4.1 is that BLG allows creation of a band gap that is tunable by an applied external potential and ranges from 0 to 250 meV. Such a tunable band gap has been verified in a number of transport and optical experiments¹⁹⁻²⁵ and is significant as a promising route to band gap engineering and control in graphene electronics.

4.3: Transport data of BLG devices at B=0T

We first examine the transport data from a dual-gated suspended device with moderate mobility, $\sim 10,000$ cm²/Vs. The presence of two gates allows us to adjust the applied electric field E_{\perp} and induced charge density n independently. Figure 4.2a presents a two-dimensional plot of the two-terminal differential conductance $G=dI/dV$ (color) vs. applied back gate voltage V_{bg} and top gate voltage V_{tg} . The most prominent feature of the plot, the thin diagonal band, indicates the charge neutrality point(CNP) of the device, demonstrating that charge density and type can be tuned by either of the two gates. The slope of the band in the V_{tg} - V_{bg} plane yields the ratio between the capacitive coupling efficiency of the two gates, $C_{tg}/C_{bg}\cong 0.34$, where C_{bg} (C_{tg}) is the capacitance per unit area between graphene and the back gate (top gate). From Landau fan data (not shown) as well as geometrical consideration, we estimate that $C_{bg}\sim 50$ aF/mm² and $C_{tg}\sim 16.6$ aF/mm².

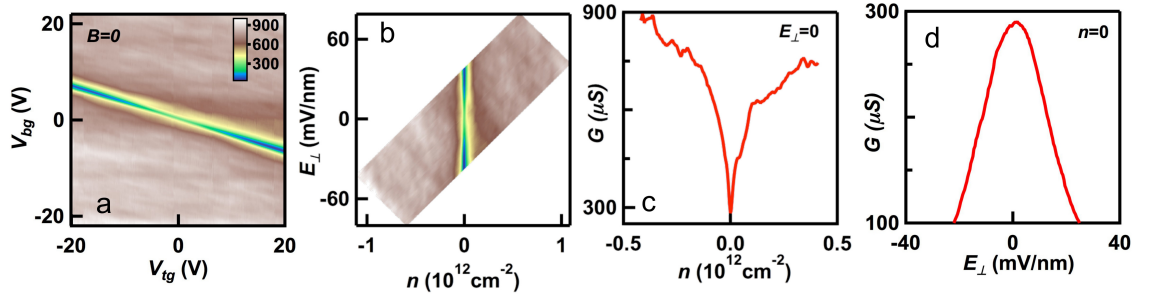


Figure 4.2: (a). $G(V_{bg}, V_{tg})$ of a device with mobility $10,000 \text{ cm}^2/\text{Vs}$ at $B=0$. (b). Same data as (a) plotted as $G(n)$. (c). Line trace $G(n)$ at $E_{\perp}=0$. (d). Line trace $G(E_{\perp})$ at $n=0$.

To analyze the device behavior as a function of E_{\perp} and n , which are calculated using

$$n = n_{bg} + n_{tg} \equiv \frac{C_{bg}}{e}(V_{bg} - V_{bg}^D) + \frac{C_{tg}}{e}(V_{tg} - V_{tg}^D) \quad (4.2)$$

$$E_{\perp} = \frac{n_{bg} - n_{tg}}{2\epsilon_0} \quad (4.3)$$

where V^D is the gate voltage at which CNP is located, ϵ_0 is the permittivity of vacuum, and the subscripts indicate back gate and top gate, respectively. Figure 4.2b replots the data in figure 4.2a as a function of E_{\perp} (vertical axis) and n (horizontal axis). A line trace $G(n)$ at $E_{\perp}=0$ is shown in figure 4.2c. As expected, G rises sharply as n increases, indicating reasonably high device quality. Figure 4.2d displays the vertical line trace $G(E_{\perp})$ at $n=0$, where G decreases symmetrically with E_{\perp} of either polarity. Such a conductance maximum at $n=0$ is consistent with the opening of a small band gap induced by electric field, as described by equation (4.1).

4.4: Transport data of TLG devices at B=0T

Trilayer graphene has two stable configurations, ABA and ABC stackings, which differ only in the relative positions of the topmost and bottom layers. As the name suggests, in ABA-stacked TLG the top and bottom layers are AA-stacked, whereas in ABC-stacked TLG they are Bernal-stacked. These 2 allotropes have dramatically different band structures^{12,19,26-31} and electrical and optical properties^{20,28,32-36}, and can be experimentally identified via infrared or Raman spectroscopy^{32,37}.

Here we will focus on only ABA-stacked TLG, which is estimated to consist of ~85% of all graphene devices. Note that this particular substrate supported device has a local top gate which only straddles a segment of the graphene sheet, but does not cover the whole device area, as shown in figure 4.3b. Its band structure is expected to be a combination of SLG's linear dispersion and BLG's quadratic dispersion. Like BLG, it is susceptible to effects of an out-of-plane electric field E_{\perp} ; but instead of the tunable band gap in BLG, ABA-stacked TLG is predicted to have a tunable band overlap^{19,26-31}. Such effects can be seen from transport data of double-gated TLG device, which is verified to be ABA-stacked via Raman spectroscopy in figure 4.3a. Figure 4.3b displays the resistance R (color) through a TLG *pnp* device with suspended top gates as functions of V_{bg} (vertical axis) and V_{tg} (horizontal axis)³⁸. The global Dirac point of the device is found to be at $V_{bg}=-7.8$ and $V_{tg}=13.5$ V. Figure 4.3c displays the line traces $R(V_{bg})$ at different V_{tg} values. For V_{tg} at the Dirac point, the $R(V_{bg})$ curve has the characteristic inverse V-shape, with an estimated mobility $4000\text{cm}^2/\text{Vs}$. As V_{tg} shifts away from the

Dirac point, *i.e.* with increasing E_{\perp} the maximum resistance R_{max} decreases, indicating an increasing band overlap, in agreement with previously reported work²⁸.

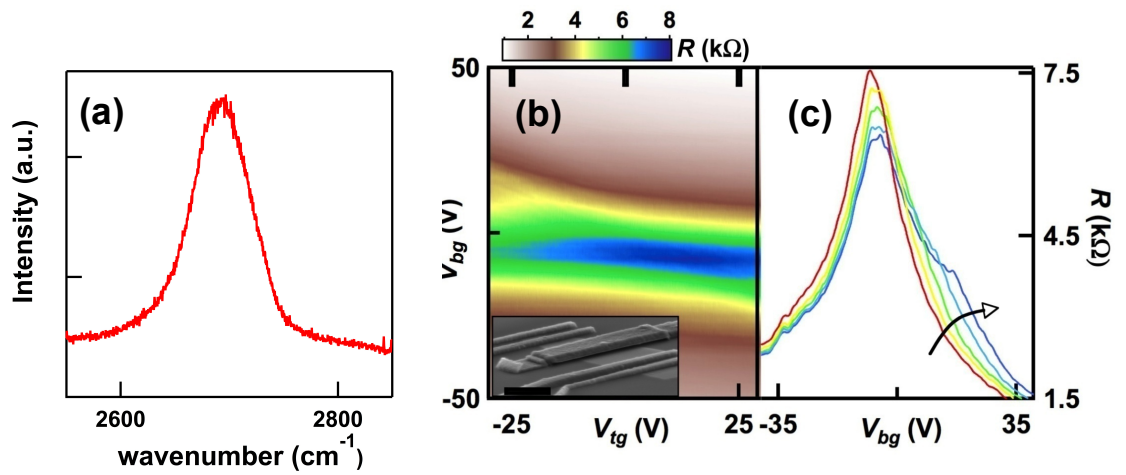


Figure 4.3: Raman and transport data from a TLG *pnp* junction. (a). Raman spectrum of the TLG device. (b). $R(V_{bg}, V_{tg})$ of the TLG device at $B=0$. (c). Line traces through (a) at, from red to blue, $V_{tg}=13.5$ (CNP), 0, 10, 20, and 28V, respectively

References

- 1 Novoselov, K. S. *et al.* Electric Field Effect in Atomically Thin Carbon Films. *Science* **306**, 666-669 (2004).
- 2 Yuanbo, Z., Yan-Wen, T., Stormer, H. L. & Kim, P. Experimental observation of the quantum Hall effect and Berry's phase in graphene. *Nature* **438**, 201-204, doi:10.1038/nature04235 (2005).
- 3 Novoselov, K. S. *et al.* Two-dimensional gas of massless Dirac fermions in graphene. *Nature* **438**, 197-200, doi:10.1038/nature04233 (2005).
- 4 Neto, A. H. C., Guinea, F., Peres, N. M. R., Novoselov, K. S. & Geim, A. K. The electronic properties of graphene. *Reviews of Modern Physics* **81**, 109-162, doi:10.1103/RevModPhys.81.109 (2009).
- 5 Changgu, L., Xiaoding, W., Kysar, J. W. & Honel, J. Measurement of the Elastic Properties and Intrinsic Strength of Monolayer Graphene. *Science* **321**, 385-388 (2008).
- 6 Balandin, A. A. *et al.* Superior Thermal Conductivity of Single-Layer Graphene. *Nano Letters* **8**, 902-907, doi:10.1021/nl0731872 (2008).
- 7 Nair, R. R. *et al.* Fine Structure Constant Defines Visual Transparency of Graphene. *Science* **320**, 1308-1308 (2008).
- 8 Measurement of the Optical Conductivity of Graphene. *Physical Review Letters* **101**, 196405 (2008).
- 9 Optical conductivity of graphene in the visible region of the spectrum. *Physical Review B* **78**, 085432 (2008).
- 10 Lee, Y. *et al.* 872506-872506-872509.
- 11 Ferrari, A. C. *et al.* Raman Spectrum of Graphene and Graphene Layers. *Physical Review Letters* **97**, 187401 (2006).
- 12 Craciun, M. F. *et al.* Trilayer graphene is a semimetal with a gate-tunable band overlap. *Nat Nano* **4**, 383-388 (2009).

- 13 Liu, G., Velasco, J., Bao, W. & Lau, C. N. Fabrication of graphene p-n-p junctions with contactless top gates. *Applied Physics Letters* **92**, 203103, doi:10.1063/1.2928234 (2008).
- 14 Moser, J., Barreiro, A. & Bachtold, A. Current-induced cleaning of graphene. *Applied Physics Letters* **91**, 163513, doi:10.1063/1.2789673 (2007).
- 15 McCann, E. & Fal'ko, V. I. Landau-Level Degeneracy and Quantum Hall Effect in a Graphite Bilayer. *Physical Review Letters* **96**, 086805 (2006).
- 16 Cho, S. & Fuhrer, M. Massless and massive particle-in-a-box states in single- and bi-layer graphene. *Nano Research* **4**, 385-392, doi:10.1007/s12274-011-0093-1 (2011).
- 17 Henriksen, E. A. *et al.* Cyclotron Resonance in Bilayer Graphene. *Physical Review Letters* **100**, 087403 (2008).
- 18 Martin, J., Feldman, B. E., Weitz, R. T., Allen, M. T. & Yacoby, A. Local Compressibility Measurements of Correlated States in Suspended Bilayer Graphene. *Physical Review Letters* **105**, 256806 (2010).
- 19 Avetisyan, A. A., Partoens, B. & Peeters, F. M. Electric-field control of the band gap and Fermi energy in graphene multilayers by top and back gates. *Phys. Rev. B* **80**, 195401, doi:10.1103/PhysRevB.80.195401 (2009).
- 20 Lui, C. H., Li, Z., Mak, K. F., Cappelluti, E. & Heinz, T. F. Observation of an electrically tunable band gap in trilayer graphene. *Nat. Phys.* **7**, 944 (2011).
- 21 Lui, C. H., Li, Z., Mak, K. F., Cappelluti, E. & Heinz, T. F. Observation of an electrically tunable band gap in trilayer graphene. *Nature Physics* **7**, 944-947, doi:10.1038/nphys2102 (2011).
- 22 Avetisyan, A., Partoens, B. & Peeters, F. Stacking order dependent electric field tuning of the band gap in graphene multilayers. *Physical Review B* **81**, 115432 (2010).
- 23 Bao, W. Stacking-dependent band gap and quantum transport in trilayer graphene. *Nat. Phys.* **7**, 948-952 (2011).
- 24 Zou, K. & Zhu, J. Transport in gapped bilayer graphene: The role of potential fluctuations. *Physical Review B* **82**, 081407 (2010).
- 25 Jing, L. *et al.* Quantum Transport and Field-Induced Insulating States in Bilayer Graphene pnp Junctions. *Nano Letters* **10**, 4000-4004, doi:10.1021/nl101901g (2010).

- 26 Guinea, F., Castro Neto, A. H. & Peres, N. M. R. Electronic states and Landau levels in graphene stacks. *Phys. Rev. B* **73**, 245426 (2006).
- 27 Aoki, M. & Amawashi, H. Dependence of band structures on stacking and field in layered graphene. *Sol. State Commun.* **142**, 123-127 (2007).
- 28 Craciun, M. F. *et al.* Trilayer graphene is a semimetal with a gate-tunable band overlap. *Nat. Nanotechnol.* **4**, 383-388, doi:[10.1038/nnano.2009.89](https://doi.org/10.1038/nnano.2009.89) (2009).
- 29 Zhang, F., Sahu, B., Min, H. K. & MacDonald, A. H. Band structure of ABC-stacked graphene trilayers. *Phys. Rev. B* **82**, 035409, doi:[10.1103/PhysRevB.82.035409](https://doi.org/10.1103/PhysRevB.82.035409) (2010).
- 30 Partoens, B. & Peeters, F. M. From graphene to graphite: Electronic structure around the K point. *Phys. Rev. B* **74**, 075404 (2006).
- 31 Avetisyan, A. A., Partoens, B. & Peeters, F. M. Stacking order dependent electric field tuning of the band gap in graphene multilayers. *Phys. Rev. B* **81**, 115432, doi:[10.1103/PhysRevB.81.115432](https://doi.org/10.1103/PhysRevB.81.115432) (2010).
- 32 Mak, K. F., Shan, J. & Heinz, T. F. Electronic structure of few-layer graphene: experimental demonstration of strong dependence on stacking sequence. *Phys. Rev. Lett.* **104**, 176404 (2010).
- 33 Henriksen, E. A., Nandi, D. & Eisenstein, J. P. Quantum Hall Effect and Semimetallic Behavior of Dual-Gated ABA-Stacked Trilayer Graphene. *Physical Review X* **2**, 011004.
- 34 Bao, W. *et al.* Stacking-Dependent Band Gap and Quantum Transport in Trilayer Graphene. *Nat. Phys.* **7**, 948-952 (2011).
- 35 Zhang, L., Zhang, Y., Camacho, J., Khodas, M. & Zaliznyak, I. The experimental observation of quantum Hall effect of $l=3$ chiral quasiparticles in trilayer graphene. *Nat. Phys.* **7**, 953 (2011).
- 36 Taychatanapat, T., Watanabe, K., Taniguchi, T. & Jarillo-Herrero, P. Quantum Hall effect and Landau level crossing of Dirac fermions in trilayer graphene. *Nat. Phys.* **7**, 621 (2011).
- 37 Lui, C. H. *et al.* Imaging stacking order in few-layer graphene. *Nano Lett.* **11**, 164-169 (2011).
- 38 Velasco Jr, J. *et al.* Quantum transport in double-gated graphene devices. *Solid State Communications* **152**, 1301-1305, doi:[http://dx.doi.org/10.1016/j.ssc.2012.04.024](https://dx.doi.org/10.1016/j.ssc.2012.04.024) (2012).

Chapter 5 : Quantum Hall state in ABA trilayer graphene

As a fascinating two-dimensional (2D) system with chiral charge carriers and spectacular electronic, mechanical and thermal properties, graphene and its multilayer counterparts¹⁻³ have emerged as new platforms for investigation of quantum Hall(QH) physics. A number of novel phenomena have been observed, such as multicomponent fractional QH effect in monolayer graphene(MLG)⁴⁻⁷, insulating $\nu=0$ states in MLG and bilayer graphene(BLG)⁸⁻¹⁷, electric field-driven transitions among symmetry-broken QH states in BLG^{14,15}, and chiral charge carriers with berry phase of 3π ¹⁸ and Lifshitz transition in ABC-stacked trilayer graphene (TLG)¹⁹.

In this chapter, we will discuss transport measurements on high quality ABA TLG in the QH regime. Section 5.1 describes the fabrication and characterization of the high mobility dual-gated ABA TLG devices. Section 5.2 present the single particle QH states at filling factors $\nu=-8, -2, 2, 6$, and 10 at low magnetic field $B<4T$, at filling factors $\nu=-8, -2, 2, 6$, and 10, which can be accounted for by the “2+1” tight-binding model that includes all hopping parameters³⁶. Section 5.3 discusses additional states at $\nu=\pm 1, \pm 3, -4$ and -5 , indicating almost complete lifting of the degeneracy of the lowest landau level (LL) at higher B . In section 5.4 at constant B , application of an out-of-plane electric field E_{\perp} gives rise to degeneracy breaking and transitions between QH plateaus, suggesting the interplay of layer polarization induced by E_{\perp} and B -enhanced exchange interactions of these states. Finally, depending on its polarity, we find the E_{\perp} selectively breaks the LL degeneracy in the electron-doped or hole-doped regimes⁴⁹.

5.1: Device characterization

TLG sheets are isolated via mechanical exfoliation on Si/SiO₂ substrates, identified by optical contrast and Raman spectroscopy³⁷, and coupled to Cr/Au electrodes and Cr suspended top gates^{38,39}. The stacking order is ascertained by Raman spectroscopy⁴⁰, the very strong $\nu=2$ quantum Hall plateau³³ and absence of Lifshitz transition¹⁹. The devices are completed by removal of SiO₂ under the graphene with hydrofluoric acid (HF) etching in figure 5.1a. A typical device has source-drain separation 1.3 μm , and width 1.4 - 1.6 μm . All data are taken at 300mK in He³ refrigerators.

An important advantage of the suspended top-gate structure is its compatibility with post-fabrication annealing that may dramatically improve sample quality. Figure 5.1b displays the two-terminal conductance G as a function of back gate V_{bg} before (black curve) and after (red curve) current annealing. After annealing, the curve becomes ‘V’-shaped, with charge neutrality close to zero, drastically lower minimum conductance, and high field effect mobility of $\sim 15,000 \text{ cm}^2/\text{Vs}$. We note that the typical contact resistance of our two-terminal device is less than 200 Ω , which can be ascertained from the deviation of the QH plateaus from their expected values.

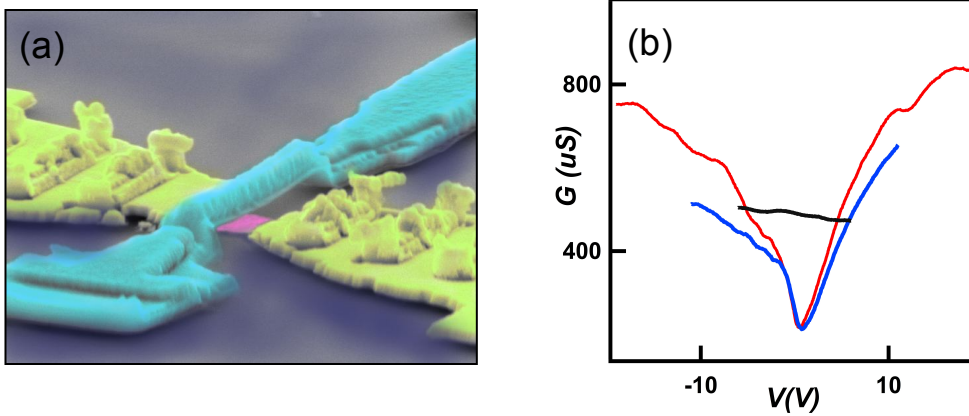


Figure 5.1: (a) SEM image of a dual-gated suspended TLG device. (b) $G(V_{bg})$ before (black) and after (red) current annealing and $G(V_{tg})$ after (blue) current annealing

5.2: Energy band structure in ABA TLG

In the simplest tight binding model that includes only the nearest neighbor in-plane and inter-plane hopping parameters γ_0 and γ_1 , the band structure of ABA-stacked TLG consists of the MLG-like and BLG-like branches touching at a single point in figure 5.2a. In sufficiently large applied B , the charges' cyclotron orbits coalesce to form discrete LLs, with energy given by^{20,41-43}:

$$E_{M,N} = \pm \sqrt{2\hbar v_F^2 e B |N|} \quad \text{and} \quad E_{B,N} = \pm \frac{\hbar e B}{m^*} \sqrt{N(N-1)} \quad (5.1)$$

The lowest LL is 12-fold degenerate, giving rise to quantized plateaus at filling factors $\nu = nh/Be = \dots -10, -6, 6, 10, 14, \dots$. Here e is electron charge, n the induced charge density,

h Planck's constant, $v_F \sim 10^6$ m/s the Fermi velocity, $m^* = \frac{\gamma_1}{\sqrt{2}v_F^2} \sim 0.02-0.04 m_e$, m_e the

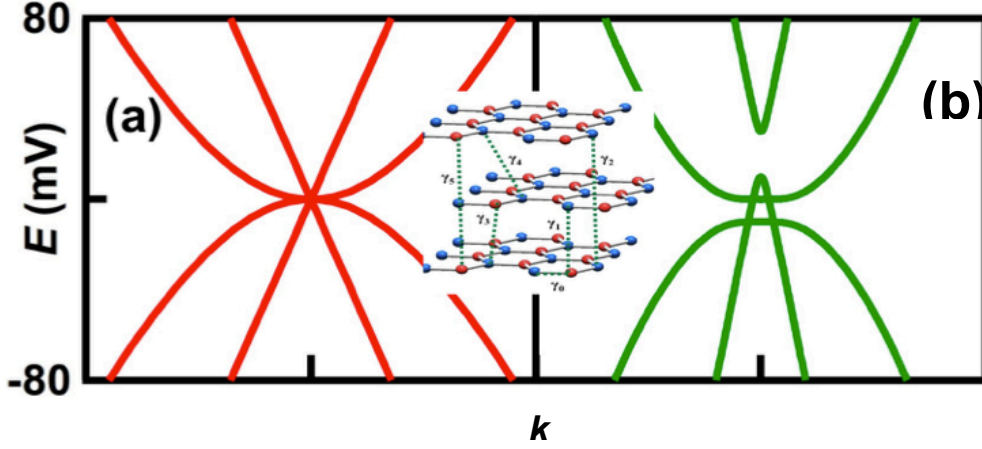


Figure 5.2: (a) Low energy band structure of ABA-stacked TLG calculating using only γ_0 and γ_1 , (b) using $\gamma_0 - \gamma_5$. Inset: ABA-stacked TLG lattice with hopping parameters $\gamma_1 - \gamma_5$.

electron rest mass, $\gamma_1 \sim 0.3$ eV is the interlayer coupling, and N is an integer denoting the LL index.

5.3: Quantum Hall state of ABA TLG in single particle picture

Figure 5.3a shows the standard LL “fan diagram” of the device, *i.e.* G (color scale) as a function of V_{bg} (horizontal axis) and B (vertical axis). The QH plateaus appear as the colored bands that diverge from $B=0$ and the charge neutrality point (CNP). The small apparent curvature in the fan diagram for small B arises from the smeared crossing between MLG-like and BLG-like bands, which will be discussed further below. From the fan diagram, the back gate’s coupling efficiency is estimated to be $\alpha_{bg} \sim 3.8 \times 10^{10} \text{ cm}^{-2}/\text{V}$, which also agrees with that calculated from device geometry.

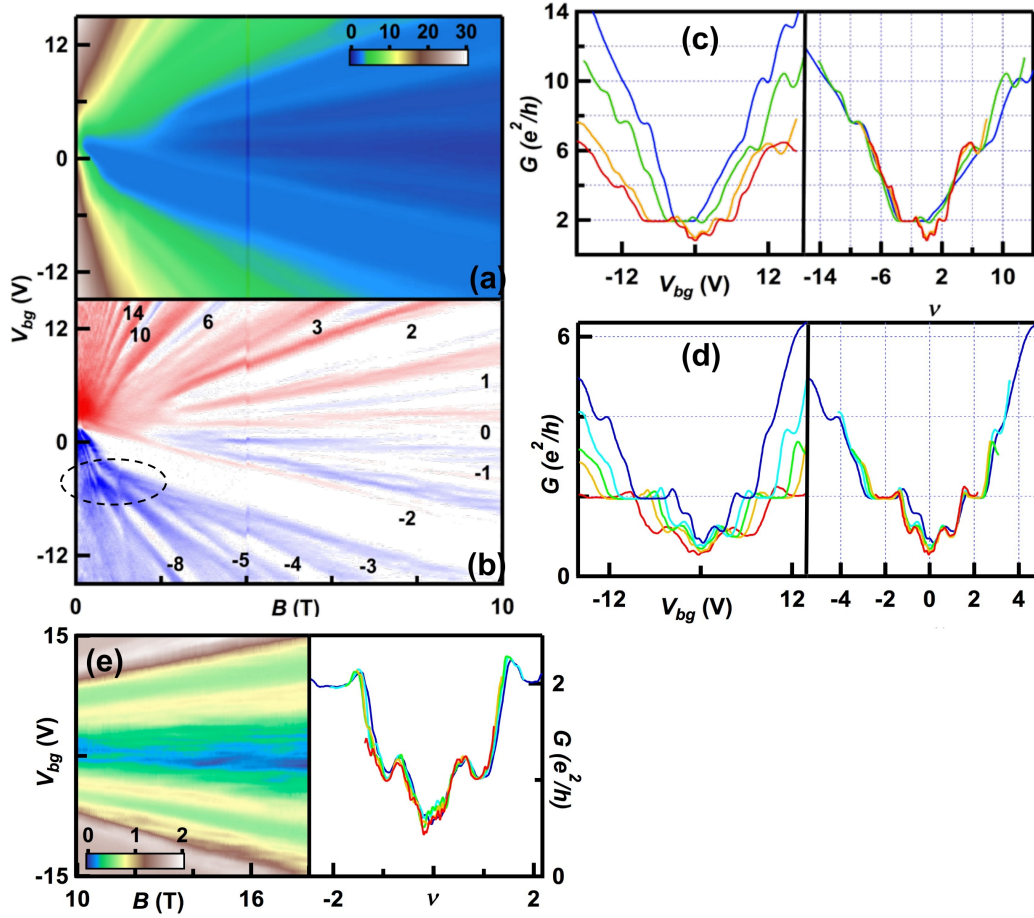


Figure 5.3: (a-b). $G(V_{bg}, B)$ and dG/dV_{bg} of a TLG device. Numbers indicate filling factors. The color scale in a indicate conductance in units of e^2/h . (c). $G(V_{bg})$ and $G(\nu)$ at $B=1.5, 2.2, 3.5$ and 4.2 T, respectively (from blue to red). (d). $G(V_{bg})$ and $G(\nu)$ at $B=4.5, 6, 7, 8$ and 10 T (from blue to red). (e). $G(V_{bg}, B)$ and $G(\nu)$ at $B=10, 12, 14, 16$ and 18 T (from blue to red).

To accentuate the evolution of the QH plateaus with V_{bg} and B , we plot dG/dV_{bg} (V_{bg}, B) of the same data set in figure 5.3b. The filling factor of each plateau, which appears as a white band, $\nu = nh/Be = a_{bg}V_{bg}h/Be$, is calculated from its slope in the V_{bg} - B plane and labeled in figure 5.3b. The most prominent feature is the very strong $\nu = -2$ plateau in the hole-doped regime, which is resolved at B as small as 0.25 T. (Here we

define hole-doped and electron-doped regime to have negative and positive filling factors, respectively.) Line traces $G(V_{bg})$ at several B values for $B < 4.2\text{T}$ are shown in figure 5.3c. When replotted as a function of ν , the traces nearly collapse into a single curve, with properly quantized plateaus at $\nu = -2, 2, 6$ and 10 .

The appearance of robust $\nu = 6$ and 10 states agrees with equation 5.1 as well as prior reports^{30,33,35}. On the other hand, our observation of the $\nu = 2$ and in particular the exceedingly robust $\nu = -2$ plateaus, is unexpected from equation 5.1. This can however be accounted for by the “2+1” model that takes remote hopping into account – instead of MLG-like and BLG-like bands both touching at a single point, including next-nearest hopping parameters (γ_2 and γ_5) leads to bands that are individually gapped, with a relative vertical offset between the MLG-like and BLG-like bands, whose tops of valence bands are located at $-\gamma_2/2$ and $\gamma_2/2$, respectively in figure 5.2b. Consequently, the LL spectrum of such a band structure is modified from equation 5.1 as follows: (i). since ABA stacked TLG obeys mirror symmetry but not inversion symmetry³⁶, its valley degeneracy is not protected; the broken valley degeneracy of the lowest LL³⁶ manifests as $\nu = \pm 2$ plateaus, as observed experimentally; (ii). the spectrum is particle-hole asymmetric, and (iii). LLs originating from the MLG-like and BLG-like bands cross at energy $\sim \pm \gamma_2/2$.

All three features are observed in our experimental data. Apart from the robust $\nu = \pm 2$ plateaus, the particle-hole asymmetry is clearly reflected in the sequence of resolved plateaus the $\nu = 6$ and 10 plateau is observed only in the electron doped regime, and $\nu = -8$ solely in the hole-doped regime. The dark blue feature at $V_{bg} \sim -5\text{V}$, indicated by the dotted circle in figure 5.3b, corresponds to the crossings between LLs that belong to

the MLG and BLG-like spectra³⁶. From the data, the crossings occur at $\sim 1.9 \times 10^{11} \text{ cm}^{-2}$, corresponding to $\sim 8 \text{ meV}$. Thus our data suggest $\gamma_2 \sim 16 \text{ meV}$ in TLG, in reasonable agreement with the value from bulk graphite, 20 meV ⁴⁴.

5.4: Quantum Hall state of ABA TLG in electronic interaction

At larger B , we also observe additional plateaus at $\nu = \pm 1, \pm 3, -4$ and -5 , which indicate almost complete lifting of spin, valley and orbital degeneracies in the lowest LL. The $\nu = 0$ plateau, although resolved, is $\sim 0.3 e^2/h$ at 18T. This lack of true insulating behavior is likely due to the presence of small amount of residual impurities. Figure 5.3c-d plots $G(V_{bg})$ and $G(n)$ at $B = 4.5, 6, 7, 8$ and 10T, respectively, showing satisfactory conductance quantization. The $\nu = \pm 1$ plateaus are resolved at B as low as 4.5T, and persists to 18T in figure 5.3e-f, the highest available field. These additional plateaus, particularly those at odd filling factors, cannot be accounted for by any tight binding model or simple breaking of layer symmetry due to any presence of an out-of-plane electric field. Instead, the plateaus' appearance at high B values in samples with high mobility ($\geq 10,000 \text{ cm}^2/\text{Vs}$) strongly suggests symmetry breaking arising from electronic interactions. In fact, they can be qualitatively understood in terms of QH ferromagnetism and Hund's rule-like filling of the 12-fold degenerate lowest LL⁴⁵. Within this model, the LLs between $\nu = -6$ and 6 are filled in the order of maximizing spin, chirality (BLG-like branch first), valley and orbital indices. At large B , the $\nu = -5, -4, -3, -2, 1, 2, \text{ and } 3$ states belong to the BLG-like branch, while the $\nu = -1, 0, +4$ and $+5$ states to the MLG-like branch². (The $\nu = 4$ is a marginal case as it separates a series of bilayer-like LL's and a

series of monolayer-like LL's; at $\nu=4$, for positive energies, the last $N=0$ bilayer-like LL is filled or the first $N=0$ MLG-like LL is empty.) As observed experimentally, all the BLG-like states are fully resolved, whereas only the $\nu=-1$ (and to some extent the $\nu=0$) state in the SLG-like branches is observed. This is consistent with previous observations that the QH ferromagnetic states in BLG are more easily resolved, due to its enhanced density of states and stronger electronic interactions near charge neutrality that readily quench the charges' kinetic energies in finite magnetic fields. Such electronic interaction may also be responsible for the absence of the $\nu=-6$ state, whose gap could be diminished by the splitting of LLs at $\nu=-3$, -4 and -5 .

5.5: Quantum Hall state of ABA TLG in the effect of E_{\perp}

We now focus on the QH states in the presence of both top and back gates. Sweeping both top and back gate voltages enables independent modulation of the electric field E_{\perp} and total charge carrier density n in TLG, which has emerged as a critical tool to study the broken symmetry states in bilayer graphene¹⁴⁻¹⁶. For ABA-stacked TLG, E_{\perp} breaks its mirror reflection symmetry, and is expected to give rise to otherwise unresolved plateaus or the stabilization of existing plateau with finite E_{\perp} .

In figure 5.4a-c, G (color scale) is plotted as a function of E_{\perp} (vertical axis) and n (horizontal axis) at $B=5.5$, 8 and 14 T, respectively. Here n and E_{\perp} are calculated by

$$n = \alpha_{bg}(V_{bg} - V_{bg}^D) + \alpha_{tg}(V_{tg} - V_{tg}^D) \equiv n_{bg} + n_{tg} \quad (5.3)$$

$$E_{\perp} = \frac{(n_{bg} - n_{tg})e}{2\epsilon_0} \quad (5.4)$$

where V^D is the Dirac point, α is the coupling efficiency, ϵ_0 the permittivity of vacuum, and the subscripts indicate back gate and top gate, respectively. The vertical color bands correspond to the conductance plateaus at different filling factors. Figure 5.4d plots $G(n)$ at $B=8\text{T}$ and $E_{\perp}=0, 43$ and 73 mV/nm, respectively. At $E_{\perp}=0$, plateaus $\nu=0, 1, 2$ and 3 are observed. At $E_{\perp}=43$ mV/nm, the first 3 plateaus remain relatively unchanged, whereas the $\nu=3$ plateau is better resolved, and the $\nu=4$ plateau emerges. Thus, our data suggest that layer polarization is an important component in the $\nu=3$ and 4 states.

In contrast to the electron-doped regimes, the hole plateaus in figure 5.4d, though resolved, are not perfectly quantized: conductance at filling factor $\nu=-1, -2$ and -4 are $\sim 1, 1.7$ and 2.8 , respectively. This arises from the slightly lower hole mobility (25% lower than electrons) in this particular device, which may result from the presence of scatterers that preferentially scatter holes.

Another striking feature in these $G(n, E_{\perp})$ plots is the dependence of the $\nu=0$ plateau on E_{\perp} : it abruptly increases from 0.3 to $\sim 1 e^2/h$ at a critical $E_{\perp,c}$ value, and decreases to 0.3 again for a larger E_{\perp} in figure 5.4d. The $G(n)$ trace at $E_{\perp,c}$ is characterized by the absence of the $\nu=0$ plateau (figure 5.4d, blue line). Taken together, our data suggest a transition from spin-ordered to layer-polarized states driven by B and E_{\perp} , respectively, and is highly reminiscent of that in BLG¹⁴⁻¹⁶.

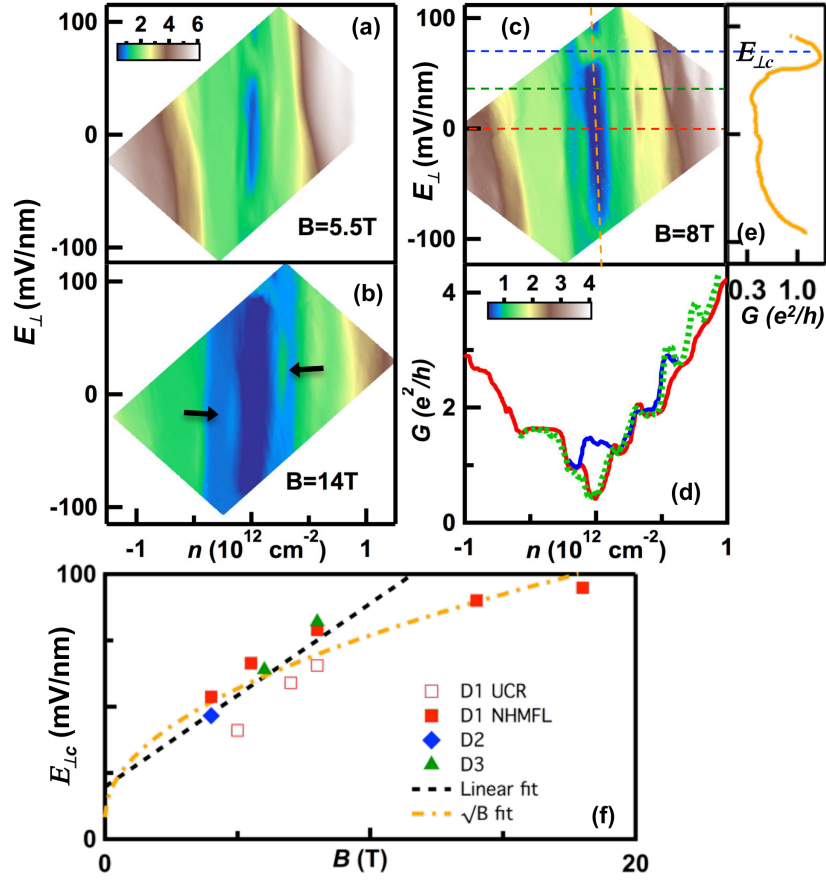


Figure 5.4: (a-c). $G(n, E_{\perp})$ at $B=5.5, 14$ and 8T . (a) and (b) has the same color scale, and color scale of c is shown in panel (d). The arrows in (b) indicate the asymmetry in E_{\perp} in electron- and hole-doped regimes. (d). $G(n)$ along the horizontal lines in (c) at $E_{\perp}=0$ (red), 43 (green dotted line) and 73 mV/nm (blue), respectively. Color scales: G in units of e^2/h . (e). $G(E_{\perp})$ along the vertical line in (c) at $n=0$. (f). $E_{\perp,c}(B)$ from 3 different devices. The black and orange lines correspond to linear and $B^{1/2}$ fits, respectively.

To further investigate the transition between the LLs, we examine the dependence of $E_{\perp,c}$ on B . In BLG, $E_{\perp,c}$ is linearly dependent on B , with a slope ~ 13 mV/nm/T and extrapolates to a finite value ~ 12 mV/nm at $B=0$ ¹⁴⁻¹⁶. Figure 5.4f plots $E_{\perp,c}$ vs. B for 3 different devices (device D1 was measured at 2 separate locations). For $B < 8\text{T}$, within the scatter in the data, $E_{\perp,c}$ is approximately linear in B , with a best-fit equation $E_{\perp,c}$ (mV/nm) =

$19.7 + 6.9B$. Interestingly, when B is extended to 18T, the data points are no longer linear; instead, they can be adequately fitted to the equation $E_{\perp c}(\text{mV/nm}) = 8.3 + 21.7 B^{1/2}$, suggesting that Coulomb interactions play an essential role at higher B . There is little theoretical work on LL transitions in ABA-stacked TLG in the presence of electric and magnetic fields, and this phenomenon warrants further experimental and theoretical investigation.

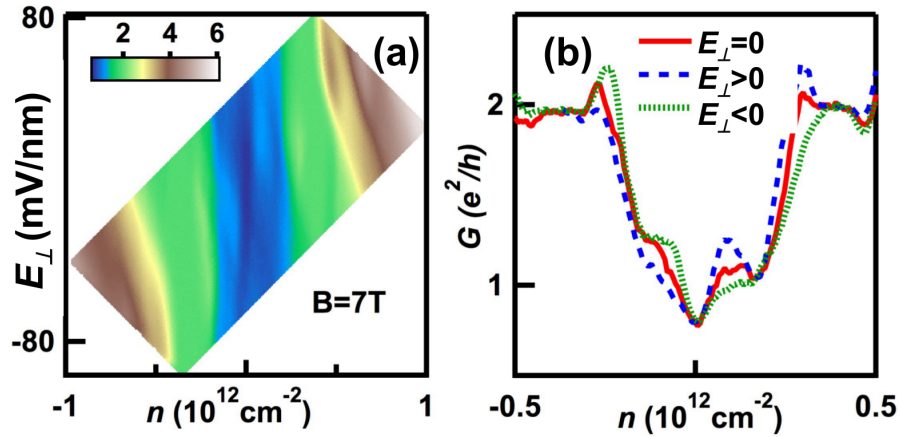


Figure 5.5: (a). $G(n, E_{\perp})$ at $B=7\text{T}$ in units of e^2/h . (b). $G(n)$ at $E_{\perp}=0$ (red solid line), -17 (green dotted line) and 13.6 mV/nm (blue dashed line).

Finally, we focus on a peculiar feature of the conductance in the presence of E_{\perp} and B . Figure 5.5 plots $G(E_{\perp}, n)$ at $B=7\text{T}$. At finite E_{\perp} , the $G(n)$ traces are asymmetric with respect to electrons and holes. Interestingly, such asymmetry depends on the direction of the applied E_{\perp} , and reverses upon reversal of the sign of E_{\perp} . In figure 5.5a, this asymmetry can be seen as the asymmetric appearance of the bright blue band to the right (left) of the

charge neutrality point for positive (negative) E_{\perp} . A similar asymmetry can be seen in figure 5.4a, as indicated by the dotted ovals. Figure 5.5b plots the $G(n)$ curves at $E_{\perp}=0$, -17 and 13.6 mV/nm, respectively. The $\nu=-1$ plateau was only resolved for $E_{\perp}<0$, whereas the $\nu=1$ state was better resolved for $E_{\perp}>0$. Thus, E_{\perp} appears to selectively break the symmetry of LLs of the electron- or hole- doped regimes, depending on its polarity. We currently do not have an explanation for this phenomenon. It may be related to the particle-hole asymmetry in few layer graphene's band structure⁴⁶, or to more intriguing phenomena such as spin-orbit interactions or magneto-electric effects^{47,48}. Further experimental investigation will be necessary to fully elucidate its origin.

Conclusion

In conclusion, using dual-gated high mobility samples, we observe several intriguing phenomena related to the broken symmetry QH states in ABA-stacked TLG, including almost complete lifting of the spin, valley and orbital degeneracies of the lowest LL, stabilization of some of these states by E_{\perp} , transition between LLs driven by E_{\perp} and B , and a particle-hole asymmetry that depends on the polarity of E_{\perp} . Our study demonstrates the rich interaction physics in ABA TLG in the E_{\perp} - B - n phase space. A number of unresolved questions, such as the dependence of $E_{\perp c}$ on B at large field, and dependence of the electron-hole asymmetry on E_{\perp} .

Reference

- 1 Novoselov, K. S.; Geim, A. K.; Morozov, S. V.; Jiang, D.; Zhang, Y.; Dubonos, S. V.; Grigorieva, I. V.; Firsov, A. A. *Science* 2004, *306*, 666–669.
- 2 Fuhrer, M. S.; Lau, C. N.; MacDonald, A. H. *MRS Bull.* 2010, *35*, 289–295.
- 3 Lau, C. N.; Bao, W.; Velasco, J., Jr. *Materials Today* 2012, *15*, 238–245.
- 4 Du, X.; Skachko, I.; Duerr, F.; Luican, A.; Andrei, E. Y. *Nature* 2009, *462*, 192–195.
- 5 Bolotin, K. I.; Ghahari, F.; Shulman, M. D.; Stormer, H. L.; Kim, P. *Nature* 2009, *462*, 196–199.
- 6 Dean, C. R.; Young, A. F.; Cadden-Zimansky, P.; Wang, L.; Ren, H.; Watanabe, K.; Taniguchi, T.; Kim, P.; Hone, J.; Shepard, K. L. *Nature Physics* 2011, *7*, 693–696.
- 7 Young, A. F.; Dean, C. R.; Wang, L.; Ren, H.; Cadden-Zimansky, P.; Watanabe, K.; Taniguchi, T.; Hone, J.; Shepard, K. L.; Kim, P. *Nature Physics* 2012, *8*, 550–556.
- 8 Checkelsky, J. G.; Li, L.; Ong, N. P. *Phys. Rev. Lett.* 2008, *100*, 206801.
- 9 Checkelsky, J. G.; Li, L.; Ong, N. P. *Phys. Rev. B* 2009, *79*, 115434.
- 10 Zhao, Y.; Cadden-Zimansky, P.; Jiang, Z.; Kim, P. *Phys. Rev. Lett.* 2010, *104*, 066801.
- 11 Feldman, B. E.; Martin, J.; Yacoby, A. *Nature Physics* 2009, *5*, 889–893.
- 12 Veligura, A.; van Elferen, H. J.; Tombros, N.; Maan, J. C.; Zeitler, U.; van Wees, B. J. *Phys. Rev. B* 2012, *85*, 155412.
- 13 Freitag, F.; Trbovic, J.; Weiss, M.; Schonenberger, C. *Phys. Rev. Lett.* 2012, *108*, 076602.
- 14 Weitz, R. T.; Allen, M. T.; Feldman, B. E.; Martin, J.; Yacoby, A. *Science* 2010, *330*, 812–816.

- 15 Velasco, J.; Jing, L.; Bao, W.; Lee, Y.; Kratz, P.; Aji, V.; Bockrath, M.; Lau, C. N.; Varma, C.; Stillwell, R.; Smirnov, D.; Zhang, F.; Jung, J.; MacDonald, A. H. *Nat Nanotechnol* 2012, 7, 156.
- 16 Maher, P.; Dean, C. R.; Young, A. F.; Taniguchi, T.; Watanabe, K.; Shepard, K. L.; Hone, J.; Kim, P. *Nature Physics* 2013, 9, 1–5.
- 17 Bao, W.; Velasco, J.; Zhang, F.; Jing, L.; Standley, B.; Smirnov, D.; Bockrath, M.; MacDonald, A. H.; Lau, C. N. *Proceedings of the National Academy of Sciences* 2012, 109, 10802–10805.
- 18 Zhang, L.; Zhang, Y.; Camacho, J.; Khodas, M.; Zaliznyak, I. A. *Nat. Phys.* 2011, 7, 953–957.
- 19 Bao, W.; Jing, L.; Lee, Y.; Velasco, J., Jr.; Kratz, P.; Tran, D.; Standley, B.; Aykol, M.; Cronin, S. B.; Smirnov, D.; Koshino, M.; McCann, E.; Bockrath, M.; Lau, C. N. *Nat. Phys.* 2011, 7, 948–952.
- 20 Guinea, F.; Castro Neto, A. H.; Peres, N. M. R. *Phys. Rev. B* 2006, 73, 245426.
- 21 Aoki, M.; Amawashi, H. *Solid State Communications* 2007, 142, 123–127.
- 22 Koshino, M.; McCann, E. *Phys. Rev. B* 2009, 79, 125443.
- 23 Zhang, F.; Sahu, B.; Min, H. K.; MacDonald, A. H. *Phys. Rev. B* 2010, 82, 035409.
- 24 Manes, J. L.; Guinea, F.; Vozmediano, M. A. H. *Phys. Rev. B* 2007, 75, 155424.
- 25 Partoens, B.; Peeters, F. M. *Phys. Rev. B* 2006, 74, 075404.
- 26 Latil, S.; Henrard, L. *Phys. Rev. Lett.* 2006, 97, 036803.
- 27 Koshino, M. *Phys. Rev. B* 2010, 81, 125304.
- 28 Yuan, S.; Roldaan, R.; Katsnelson, M. I. *Phys. Rev. B* 2011, 84, 125455.
- 29 Bao, W.; Zhao, Z.; Zhang, H.; Liu, G.; Kratz, P.; Jing, L.; Velasco, J.; Smirnov, D.; Lau, C. *Phys. Rev. Lett.* 2010, 105, 246601.
- 30 Taychatanapat, T.; Watanabe, K.; Taniguchi, T.; Jarillo-Herrero, P. *Nat. Phys.* 2011, 7, 621.

- 31 Lui, C. H.; Li, Z.; Mak, K. F.; Cappelluti, E.; Heinz, T. F. *Nat. Phys.* 2011, 7, 944.
- 32 Craciun, M. F.; Russo, S.; Yamamoto, M.; Oostinga, J. B.; Morpurgo, A. F.; Thrucha, S. *Nat Nanotechnol* 2009, 4, 383–388.
- 33 Henriksen, E. A.; Nandi, D.; Eisenstein, J. P. *Phys. Rev. X* 2012, 2, 011004.
- 34 Jhang, S. H.; Craciun, M. F.; Schmidmeier, S.; Tokumitsu, S.; Russo, S.; Yamamoto, M.; Skourski, Y.; Wosnitza, J.; Tarucha, S.; Eroms, J.; Strunk, C. *Phys. Rev. B* 2011, 84, 161408.
- 35 Khodkov, T.; Withers, F.; Hudson, D. C.; Craciun, M. F.; Russo, S. *Appl. Phys. Lett.* 2012, 100, 013114.
- 36 Koshino, M.; McCann, E. *Phys. Rev. B* 2011, 83, 165443.
- 37 Ferrari, A. C.; Meyer, J. C.; Scardaci, V.; Casiraghi, C.; Lazzeri, M.; Mauri, F.; Piscanec, S.; Jiang, D.; Novoselov, K. S.; Roth, S.; Geim, A. K. *Phys. Rev. Lett.* 2006, 97, 187401.
- 38 Liu, G.; Velasco, J.; Bao, W.; Lau, C. N. *Appl. Phys. Lett.* 2008, 92, 203103.
- 39 Velasco, J., Jr; Liu, G.; Bao, W.; Ning Lau, C. *New J. Phys.* 2009, 11, 095008.
- 40 Lui, C. H.; Li, Z.; Chen, Z.; Klimov, P. V.; Brus, L. E.; Heinz, T. F. *Nano Lett.* 2011, 11, 164–169.
- 41 McClure, J. W. *Phys Rev* 1956, 104, 666–671.
- 42 McCann, E.; Fal'ko, V. I. *Phys. Rev. Lett.* 2006, 96, 086805.
- 43 Ezawa, M. *J. Phys. Soc. Jpn.* 2007, 76, 094701.
- 44 Dresselhaus, M. S.; Dresselhaus, G. *Advances in Physics* 2002, 51, 1–186.
- 45 Zhang, F.; Tilahun, D.; MacDonald, A. H. *Phys. Rev. B* 2012, 85, 165139.
- 46 Zhang, L. M.; Fogler, M. M.; Arovas, D. P. *Phys. Rev. B* 2011, 84, 075451.
- 47 Zhu, L.; Aji, V.; Varma, C. M. 2012, arXiv:1202.0821v1.

- 48 Winkler, R.; Zuelicke, U. *preprint* 2012, arxiv:1206.4761.
- 49 Lee, Y. *et al.* Broken symmetry quantum Hall states in dual-gated ABA trilayer graphene. *Nano Lett* **13**, 1627-1631, doi:10.1021/nl4000757 (2013).

Chapter 6 : The intrinsic gap in ABC Trilayer graphene

Many physical phenomena can be understood by single particle physics, i.e. treating particles as non-interacting entities. When this fails, many-body interactions leads to spontaneous symmetry breaking and phenomena such as fundamental particles' mass generation, superconductivity and magnetism. Competition between single-particle and many-body physics leads to rich phase diagrams.

In this chapter, we will discuss transport measurement on high quality rhombohedral-stacked trilayer graphene(r-TLG) at the charge neutrality point(CNP). Section 6.1 describes the fabrication and characterization of the high mobility dual-gated ABC TLG devices. Section 6.2 to 6.4 present the experimental evidence for the presence of a giant intrinsic gap $\sim 42\text{meV}$ at the charge neutrality point that can be partially suppressed by an interlayer potential, a parallel magnetic field or a critical temperature $\sim 36\text{K}$. In section 6.5 and section 6.6, we discuss the theoretical calculation of the screening length and the antiferromagnetic gap. In section 6.7, we discuss the possible candidates for this gapped state, and conclude that among the proposed correlated phases with spatial uniformity, our results are most consistent with a layer antiferromagnetic state with broken time reversal symmetry. These results reflect the interplay between externally induced and spontaneous symmetry breaking whose relative strengths are tunable by external fields, and provide insight into other low dimensional systems¹.

6.1: Device characterization

Trilayer Graphene sheets are mechanically exfoliated onto 300nm SiO₂ wafers layer grown over degenerately doped Si. ABC or rhombohedral stacked trilayer (r-TLG) sheets are selected by color contrast in optical microscope² and Raman spectroscopy^{3,4}, coupled to electrodes and top gates using multi-level lithography^{5,6}, and etched in HF to partially removes the SiO₂ layer. All devices have source-drain separation $\sim 1.1\mu\text{m}$ and width $\sim 1.1\text{-}1.4\mu\text{m}$.

Most as-fabricated devices have low mobility, and current annealing is performed at 4 K to improve sample quality^{7,8}. Typically the optimal annealing results are achieved when current starts to saturate, at $\sim 0.3\text{-}0.4\text{mA}\mu\text{m}^{-1}\text{layer}^{-1}$. After annealing, device mobility is as high as $90,000\text{cm}^2\text{V}^{-1}\text{s}^{-1}$. Figure 6.1 displays the conductance G of a typical r-TLG device as a function of back gate voltage V_{bg} before and after annealing. The field-effect mobility of this device after annealing is $\sim 50,000\text{cm}^2\text{V}^{-1}\text{s}^{-1}$, with a minimum conductivity ~ 0 . The devices are measured in helium-3 refrigerators using standard lock-in techniques. All measurements are taken at $T=260\text{mK}$, unless otherwise specified.

For a given device, the induced charge density n and interlayer potential U_{\perp} are calculated from the back gate and top gate voltages, $n = (C_{\text{bg}}V_{\text{bg}} + C_{\text{tg}}V_{\text{tg}})/e$ and $U_{\perp} = (C_{\text{bg}}V_{\text{bg}} - C_{\text{tg}}V_{\text{tg}})d/2\epsilon_0$. Here e is electron charge, ϵ_0 the permittivity of vacuum, $d=0.67\text{nm}$ is the distance between the top and bottom layers, V_{bg} and V_{tg} are the voltage applied to back gate and top gate, respectively, and C_{bg} (C_{tg}) is the capacitance per unit area between graphene and back (top) gate. Capacitances are estimated from geometric

considerations, as well as from standard Landau level fan diagrams. For typical devices, C_{bg}/e ranges from 3×10^{10} to $5 \times 10^{10} \text{ cm}^{-2}$, and C_{tg}/e from 1×10^{10} to $7 \times 10^{10} \text{ cm}^{-2}$.

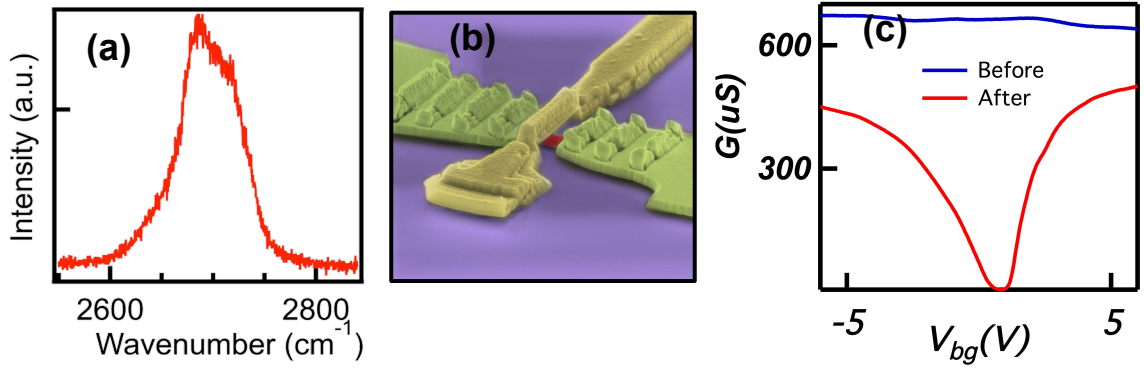


Figure 6.1: Raman spectroscopy, SEM image and current annealing (a) Raman spectroscopy of r-TLG sheet. (b) SEM image of a dual-gated suspended device. (c) Device conductance G vs V_{bg} before and after current annealing.

6.2: Gapped insulating state at the CNP

In the single particle picture, r-TLG hosts chiral charge carriers with Berry's phase 3π , and an energy-momentum dispersions $\varepsilon(k) \sim k^3$, thus they are gapless semiconductors (Figure 6.2b inset)⁹⁻¹⁶. An energy gap can be generated via two different mechanisms – in the single particle picture, upon applying a potential difference U_{\perp} between the outmost layers, the band structure adopts a gap that scales with U_{\perp} ⁹⁻¹⁶. Alternatively, close to CNP, the diverging density of states leads to strong electronic interactions, and the gapless semiconductor is expected to give way to phases with spontaneous broken symmetries; in particular, gapped phases such as layer

antiferromagnetic (LAF) and quantum anomalous Hall states with broken time reversal symmetry are expected to be favored¹⁷⁻²².

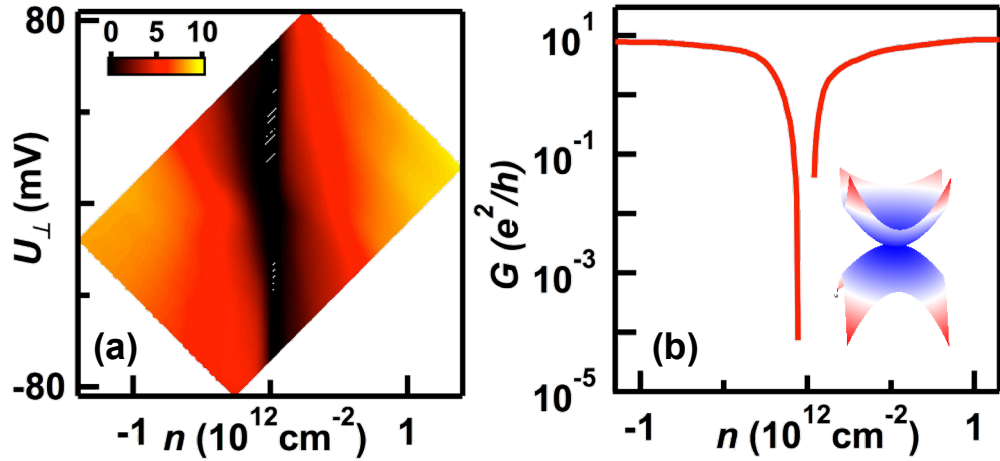


Figure 6.2: Transport data of ABC trilayer device. (a) $G(U_{\perp}, n)$ in units of e^2/h . Inset: Energy-momentum dispersion of r-TLG. (b) $G(n)$ at $U_{\perp}=0$. Note the logarithmic scale of G

At low temperatures and $B=0$, r-TLG devices become insulating in the vicinity of the CNP. In figure 6.2a, the two-terminal differential conductance $G=dI/dV$ from device 1 is plotted as n and U_{\perp} . At $U_{\perp}=0$, as n approaches the CNP, $G(n)$ decreases by more than 5 orders of magnitude to $<10^{-4} e^2/h$, where e is electron charge and h is Planck's constant in figure 6.2b. This insulating state at the CNP is extremely robust, as it persists for the entire gate ranges, up to the highest applied U_{\perp} (~ 65 mV).

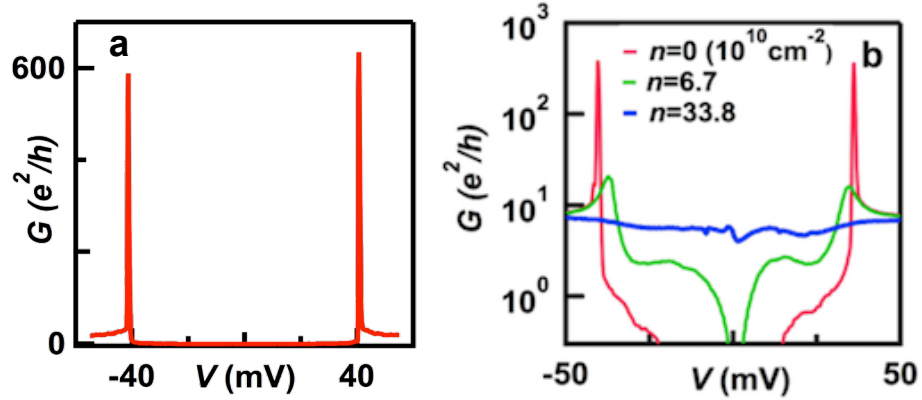


Figure 6.3: Transport data at $B_{\perp}=0$ (a) $G(V)$ at $U_{\perp}=n=0$. (b) $G(V)$ at $U_{\perp}=0$ and different n

Transport spectroscopy^{23,24} at $n=U_{\perp}=0$ reveals intriguing features: at small source-drain bias V , the device stays insulating; but as V increases ± 42 mV, G rises by more than 6 orders of magnitude to extremely sharp peaks, then decreases to $\sim 15 e^2/h$ for larger V in figure 6.3a. Such a $G(V)$ curve strongly resembles the density of state of a gapped phase, suggesting the presence of an energy gap $\Delta \sim 42$ meV at $n=U_{\perp}=B=0$. With increasing charge density n , the gap diminishes and eventually disappears entirely as shown in figure 6.3b. At $n=3 \times 10^{11} \text{ cm}^{-2}$, $G(V)$ is flat, indicating that r-TLG becomes gapless at high density.

The gapped, insulating state near the CNP in the absence of external fields is unexpected from tight-binding calculations, but instead suggests a phase arising from electronic interactions with spontaneous broken symmetries²⁵. The magnitude of the gap, ~ 42 meV, is exceedingly large for an interaction-induced state. It is more than an order of magnitude larger than that found in BLG^{23,26}, reflecting the divergent nature of the density of states and strong electronic interactions in r-TLG at the CNP. It also a factor of

7 larger than that previously observed in singly-gated devices²⁷, likely due to improved device geometry and quality.

6.3: Temperature dependence of the gapped state

To further establish the magnitude of the gap, we examine temperature dependence of $G(V)$ at $n=U_{\perp}=0$ as shown in figure 6.4a. Figure 6.4b plots minimum conductance $G_{\min}=G(V=0)$ as a function of T . At high temperatures $T>40\text{K}$, the device is conductive – $G_{\min} \sim 15 e^2/h$ with a small linear T -dependence. The $G(V)$ curves are approximately constant, similar to that of a conventional resistor. However, when $T < \sim 40\text{K}$, G_{\min} drops precipitously and becomes insulating for $T < 30\text{K}$, and $G(V)$ curves develop prominent peaks at finite V . In the transition region $30 < T < 40\text{K}$, the $G_{\min}(T)$ curve is well-described by the thermal activation equation, $G_{\min} = G_0 e^{-\Delta/2k_B T}$ in figure 6.4c, where k_B is the Boltzmann's constant and $\Delta \sim 43 \text{ meV}$ is obtained as a fitting parameter. This is in excellent agreement with the value of Δ obtained from $G(V)$ curves at $T=300 \text{ mK}$, thus confirming the presence of an insulating state with $\sim 42 \pm 1 \text{ meV}$ gap.

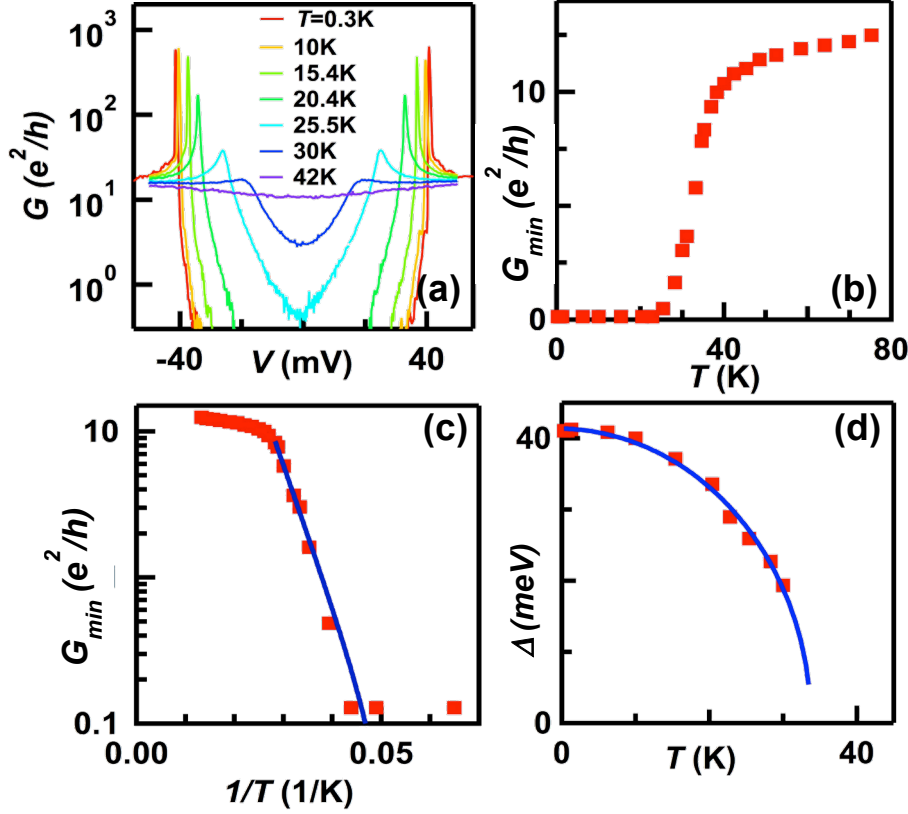


Figure 6.4: Transport data at $B_{\perp}=0$ (a) $G_{\min}(V)$ at $U_{\perp}=n=0$ and different temperatures. (b) G_{\min} at $V=0$ vs. T . (c) G_{\min} vs. $1/T$ in Arrhenius scale. The blue line is a fit to the equation $G_{\min} = G_0 e^{-\Delta/2k_B T}$ for $30\text{K} < T < 40\text{K}$. (d) Measured Δ as a function of T . The solid line is a fit to equation 6.1.

Using $G(V)$ curves, we can also directly measure the evolution of Δ (taken as half of the peak-to-peak separation in V) as a function of T . As shown in figure 6.4d, Δ is almost constant for $T < 10$ K, but drops precipitously for $T > 30$ K. This behavior is characteristic of order parameters during phase transitions in mean field theories. Thus we fit $\Delta(T)$ to the function²⁸

$$\Delta(T) = \Delta(0) \left[A \left(1 - \frac{T}{T_c} \right) + B \left(1 - \frac{T}{T_c} \right)^2 \right]^{1/2} \quad (6.1)$$

where T_c is the critical temperature. Equation 6.1 reduces to the usual mean-field

functional form $\sqrt{1 - \frac{T}{T_c}}$ for T/T_c sufficiently close to 1, and the second term $\left(1 - \frac{T}{T_c}\right)^2$ is

inserted to capture the vanishingly small dependence on T as $T \rightarrow 0$. Excellent agreement with data is obtained, yielding $A=2.0$, $B=-1.0$ and $T_c=34\text{K}$. The energy scale of the gap, $\Delta(0)/k_B=500\text{K}$, which is much larger than that associated with the critical temperature, signifies that this insulating state observed at the CNP is a correlated phase.

6.4: E_{\perp} and B_{\parallel} field dependence of the gapped state

To elucidate the nature of this correlated phase, we examine how it is modified in the presence of an external field that selectively breaks one of the degeneracies. For instance, application of U_{\perp} breaks the inversion (which-layer) symmetry, and in the single particle picture, gives rise to a proportionally-scaled energy gap. Figure 6.5a displays G as a function of V and U_{\perp} at $n=0$. As U_{\perp} is the externally imposed potential bias, it will be heavily screened due to r-TLG's large density of states near the CNP²⁹⁻³¹. Thus we expect the screened interlayer potential bias $U_{\perp}^s \ll U_{\perp}$. Using a simplified two-band Hamiltonian for r-TLG and assuming that the dielectric constant of r-TLG is 1, We self-consistently calculate screening of ABC-stacked TLG using a procedure similar to that for bilayer graphene³². In the presence of voltages applied to the gates, from Gauss' Law, we have

$$n = n_1 + n_3 = \frac{\epsilon_o \epsilon_b V_b}{eh_b} + \frac{\epsilon_o \epsilon_t V_t}{eh_t} \quad (6.2)$$

$$U_{\perp}^s = -\frac{\varepsilon_t V_t d e}{\varepsilon_r h_t} + \frac{d e^2 n_3}{\varepsilon_o \varepsilon_r} \quad (6.3)$$

In these equations, e the electron charge, ε the dielectric constant, V the voltage applied to the gate, ε_o the permittivity of vacuum, $d = 0.67$ nm is the distance between the outmost layers, h the distance between graphene and the gate, n_1 and n_3 are the charge densities on the bottom and top layers of the trilayer, and ε_r is the dielectric constant of the trilayer itself. The subscripts b and t indicate the back gate and top gate, respectively. U_{\perp}^s is the potential across the trilayer that is to be determined. Now the externally imposed interlayer potential is given by,

$$U_{\perp} = \left(\frac{\varepsilon_b V_b}{h_b} - \frac{\varepsilon_r V_t}{h_t} \right) \frac{e d}{2} \quad (6.4)$$

which gives

$$U_{\perp}^s = U_{\perp} + \frac{d e^2}{2 \varepsilon_o \varepsilon_r} (n_3 - n_1) \quad (6.5)$$

In r-TLG, inequivalent sublattices A_i and B_i are arranged in following sequence: one of the two-carbon atom sites in both the top and bottom layer $B_1(A_3)$ has a different near-neighbor carbon atom site in the middle layer $A_2(B_2)$, which leaves one-carbon atom site in the top and bottom layers $A_1(B_3)$ without a near-neighbor in the middle layer.

Interlayer hopping on adjacent layer near-neighbor carbon atom sites leads to the formation of high-energy dimer bands, which push the electron energy away from the Fermi surface, leaving one low-energy sublattice site per π -carbon orbital in the outermost layers. The effective two-band Hamiltonian for r-TLG³³

$$\begin{pmatrix} -\frac{U_{\perp}^s}{2} & \frac{v^3}{\gamma_1^2}(p_x - ip_y)^3 \\ \frac{v^3}{\gamma_1^2}(p_x + ip_y)^3 & \frac{U_{\perp}^s}{2} \end{pmatrix} \quad (6.6)$$

operates on the pseudospinor $\psi_K^{\dagger} = (\psi_{A_1,K}^{\dagger}, \psi_{B_3,K}^{\dagger})$, where $\psi_{i,K}^{\dagger}$ is the envelop

wavefunction of sublattice i at valley K , with the pseudospinor in valley K' $\psi_{K'}^{\dagger} = \hat{\tau}^x \psi_K^{\dagger}$,

$\hat{\tau}^x$ is the Pauli matrix in pseudospin space. The eigenvalues and wave functions are

$$\begin{aligned} E &= \pm \sqrt{\frac{(U_{\perp}^s)^2}{4} + \frac{v^6 |p|^6}{\gamma_1^4}}, \psi = \begin{pmatrix} \psi_{A_1} \\ \psi_{B_3} \end{pmatrix} \\ &= \sqrt{\frac{E - \frac{U_{\perp}^s}{2}}{2E}} \begin{pmatrix} 1 \\ -\frac{v^3 |p|^3}{\gamma_1^2} \frac{1}{\left(E - \frac{U_{\perp}^s}{2}\right)} e^{3i\varphi} \end{pmatrix} e^{i\vec{p}\cdot\vec{r}/\hbar} \quad (6.7) \end{aligned}$$

here v is the Fermi velocity of monolayer graphene, p is the momentum, $\gamma_1 \sim 0.4$ eV is

the nearest neighbour interlayer hopping energy, $\varphi = \tan^{-1}(p_y/p_x)$, and $\hbar = h/2\pi$ where h

is Planck's constant. The layer densities can be calculated from

$$n_1 = \frac{2}{\pi\hbar^2} \int |\psi_{A_1}|^2 p dp \quad n_3 = \frac{2}{\pi\hbar^2} \int |\psi_{B_3}|^2 p dp \quad (6.8)$$

For the hole-doped regime, the Fermi level is in the valence band, so

$$n_1 = \frac{2}{\pi\hbar^2} \int_{p_F}^{\infty} \left(\frac{E - \frac{U_{\perp}^s}{2}}{2E} \right) p dp = \frac{n}{2} + \frac{2}{\pi\hbar^2} \frac{U_{\perp}^s}{4} \int_{p_F}^{\infty} \frac{p dp}{\frac{U_{\perp}^s}{2} \sqrt{1 + \frac{4v^6 |p|^6}{\gamma_1^4 (U_{\perp}^s)^2}}} \quad (6.9)$$

Defining $x_F = \left(\frac{4}{U_{\perp}^s \gamma_1^2}\right)^{\frac{1}{3}} v^2 \pi \hbar^2 n$, we can express n_1 as

$$\begin{aligned} n_1 &= \frac{n}{2} + \frac{1}{2\pi\hbar^2} \left(\frac{(U_{\perp}^s)^2 \gamma_1^4}{4v^6}\right)^{\frac{1}{3}} \int_{x_F}^{\infty} \frac{dx}{\sqrt{1+x^3}} \\ &= \frac{n}{2} + \frac{1}{2\pi\hbar^2} \left(\frac{(U_{\perp}^s)^2 \gamma_1^4}{4v^6}\right)^{\frac{1}{3}} \left(2.8 - \int_0^{x_F} \frac{dx}{\sqrt{1+x^3}}\right) \end{aligned} \quad (6.10)$$

Similarly,

$$n_3 = \frac{n}{2} - \frac{1}{2\pi\hbar^2} \left(\frac{(U_{\perp}^s)^2 \gamma_1^4}{4v^6}\right)^{\frac{1}{3}} \left(2.8 - \int_0^{x_F} \frac{dx}{\sqrt{1+x^3}}\right) \quad (6.11)$$

So that

$$n_3 - n_1 = \frac{1}{\pi} \left(\frac{\gamma_1}{\hbar v}\right)^2 \left(\frac{U_{\perp}^s}{2\gamma_1}\right)^{\frac{2}{3}} \left[\int_0^{x_F} \frac{dx}{\sqrt{1+x^3}} - 2.8 \right] \quad (6.12)$$

Substituting into equation 6.5, we obtain,

$$U_{\perp}^s = U_{\perp} + \frac{de^2}{2\varepsilon_o \varepsilon_r} \left(\frac{1}{\pi}\right) \left(\frac{\gamma_1}{\hbar v}\right)^2 \left(\frac{U_{\perp}^s}{2\gamma_1}\right)^{\frac{2}{3}} \left[\int_0^{x_F} \frac{dx}{\sqrt{1+x^3}} - 2.8 \right] \quad (6.13)$$

that can be solved numerically for U_{\perp}^s for given U_{\perp} and n (the dependence on n comes through x_F). Note that screening is more effective for smaller n , due to the larger density of states near the charge neutrality point.

The screening-corrected data $G(V, U_{\perp}^s)$ are shown in figure 6.5b. The sharp peaks in $G(V)$, *i.e.* the gap edges, appear as red curves that separate the insulating (dark blue) and conductive (light blue) regions in figure 6.5a and 6.5b. Δ decreases symmetrically and linearly with applied U_{\perp}^s of either polarity, to ~ 30 meV at $|U_{\perp}|=50$ meV or $|U_{\perp}^s|=3$ mV as shown in figure 6.5b, though not yet completely closed at the largest

applied $|U_{\perp}|$. (In other devices with lower mobility, we also observe that the device conductance increases from $<0.1 e^2/h$ with increasing $|U_{\perp}|$, exceeding $1.5e^2/h$ at $|U_{\perp}|=85$ mV.)

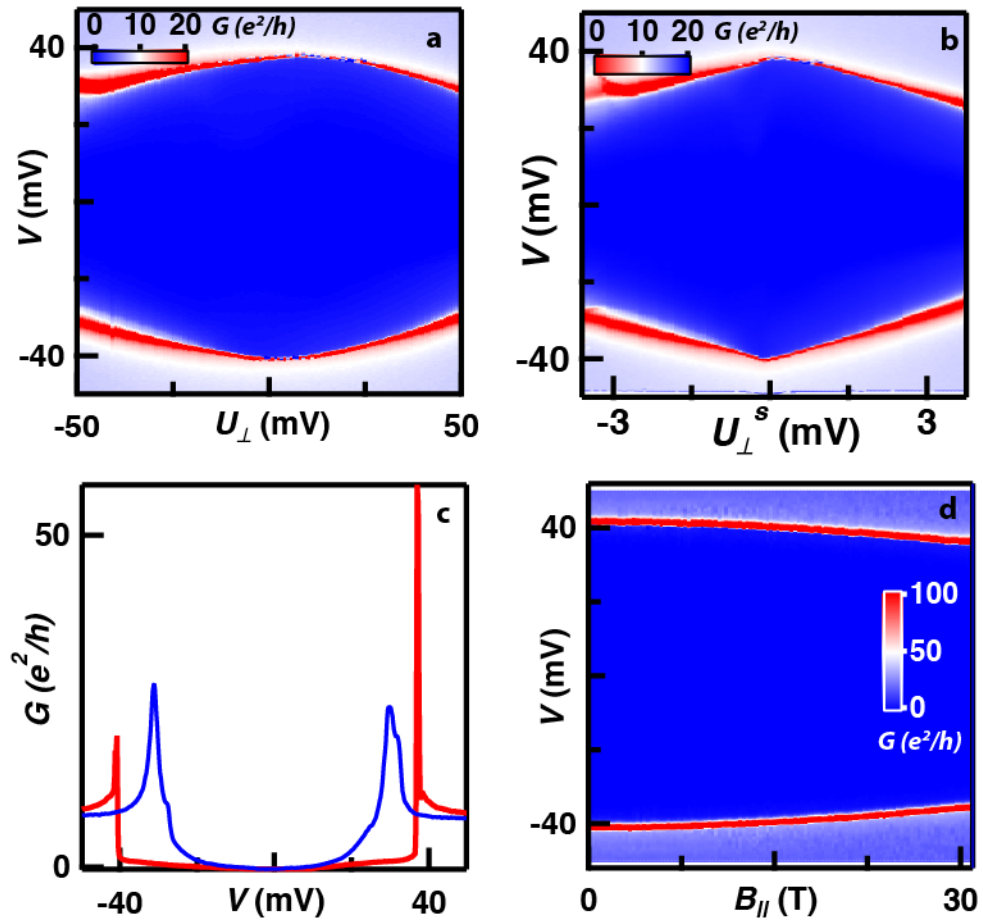


Figure 6.5: Transport data at $n=0$ and finite U_{\perp} and B_{\parallel} . (a)-(b) $G(V, U_{\perp})$ and $G(V, U_{\perp}^s)$ in units of e^2/h from Device 1. (c) Line traces $G(V)$ at $U_{\perp}=0$ and $U_{\perp}=-50$ mV. (d) $G(V, B_{\parallel})$ in units of e^2/h from Device 2

On the other hand, an in-plane magnetic field B_{\parallel} couples to the spin but not orbital degrees of freedom and raises the Zeeman energy. Figure 6.5d plots $G(V, B_{\parallel})$ for $B_{\parallel}=0$ to 31T. Δ stays almost constant for $B_{\parallel}<10$ T, but decreases to 35 mV at $B_{\parallel}=31$ T. Thus addition of Zeeman energy suppresses the gapped phase, suggesting that the phase has spin-ordering, but no net magnetic moment.

6.5: Discussion of screening length

The interplay between band structure effects and interactions in an ABC trilayer allows us to define at least four important length scales: i) The scale associated to the momentum beyond which the effects of the main interlayer hopping term, γ_1 , are small, and the bands resemble those of three independent graphene layers, $l_{\perp} \approx v_F/\gamma_1$, where $v_F = 3\gamma_0 a/2$, and $a \approx 1.4 \text{ \AA}$ is the distance between neighboring carbon atoms in a given plane, ii) The inverse of the momentum at which the band structure changes smoothly from a cubic to a quadratic dispersion, l_{BS} , iii) The Fermi-Thomas screening length, l_{FT} . This length goes to zero at the edge of a band which a cubic dispersion on momentum, so that it should be estimated at the crossover momentum $k \approx l_{BS}^{-1}$. Finally, iv) the ABC trilayer has a finite width, $d \approx 2 \times d_{BLG}$, where d_{BLG} is the interlayer distance in bilayer graphene. We assume in the following that $\gamma_4 \ll \gamma_3 \approx \gamma_1 \ll \gamma_0$. The value of l_{\perp} is

$$l_{\perp} \approx a \frac{3\gamma_0}{2\gamma_1} \quad (6.14)$$

The bands at low energies are

$$\varepsilon_k \approx \pm \frac{3}{2} \left| \frac{9\gamma_0^3}{4\gamma_2^2} (ka)^3 e^{3i\phi_k} + \frac{3\gamma_0\gamma_3}{2\gamma_1} (ka)^2 \right| \quad (6.15)$$

where $\phi_k = \arctan(k_y/k_x)$. Using this expression, we obtain

$$l_{BS} \approx a \frac{3\gamma_0^2}{4\gamma_1\gamma_3} \quad (6.16)$$

The Fermi Thomas wavelength is

$$k_{FT} \approx \frac{8e^2\gamma_1^2}{81\varepsilon_0\gamma_0^3 k_{BS}} \quad (6.17)$$

where ε_0 is the dielectric constant, and $k_{BS} = l_{BS}^{-1}$. Using equation 6.16, we find

$$l_{FT} \approx a \frac{9\gamma_3}{\alpha\gamma_1} \quad (6.18)$$

where $\alpha = \frac{e^2}{\varepsilon_0 V_F}$ is the fine structure constant of graphene.

We take $\gamma_0 = 2.7$ eV, $\gamma_1 = 0.4$ eV, and $\gamma_3 = 0.3$ eV. In order to estimate the screening length, we assume that in a suspended sample, $\varepsilon_0 = 1$, and $\alpha \sim 2.4$. We finally take $d_{BLG} \approx 0.34$ nm. Then, the previous analysis leads to

$$l_{\perp} \approx 1.4 \text{ nm}$$

$$l_{BS} \approx 6.4 \text{ nm} \quad (6.19)$$

$$l_{FT} \approx 0.4 \text{ nm}$$

$$d \approx 0.7 \text{ nm}$$

This analysis gives $l_{FT} \lesssim d$. This overestimates screening in the perpendicular direction, as the electronic states which give rise to the screening cloud are given by a coherent superposition of waves localized in the top and bottom layers. This state cannot be polarized in the direction normal to the layers. Screening in the perpendicular direction should be such that $l_{FT} \lesssim d$.

6.6: Estimation of the Antiferromagnetic Gap

The cubic dispersion of r-TLG's bands at low energies leads to a density of states that diverges as $D(\varepsilon) \propto \varepsilon^{-1/3}$ at low energies. Local interactions give rise to perturbations which should lead to a broken symmetry phase at low temperatures. The divergence encountered when studying interaction effects within perturbation theory is more severe than the logarithmic divergence found in graphene bilayers. We expect the broken symmetry phase to be more stable in a graphene trilayer than in a graphene bilayer. The renormalization group methods that can be applied in a bilayer³⁴ do not work for a trilayer, but, on the other hand, we expect that a mean field analysis should be more reliable, as the low temperature phase is more robust. A classification of possible gapped phases in an ABC trilayer has been discussed in ref³⁵, and a calculation of relative energies can be found in ref³⁶. For a bilayer with short range interactions the most likely phase is either a layer antiferromagnet or a nematic phase^{37,38}. In particular, an on site Hubbard interaction leads to a layer antiferromagnet³⁹. We present here a simple analysis of a gapped layered antiferromagnetic phase (note that a nematic phase is gapless) using mean field theory, see also³⁶. The magnitude of the local interactions in graphene and graphite is not determined, but different estimates suggest that the Hubbard onsite

interaction is $U \approx 5-10\text{eV}^{40,41}$. We use an effective Hamiltonian reduced to two sites, one in the top and the other in the bottom layer (see equation 6.6) and a local Hubbard interaction

$$H_{int} = U \sum_i \left(n_{i\uparrow} - \frac{1}{2} \right) \left(n_{i\downarrow} - \frac{1}{2} \right) \quad (6.20)$$

where the level i runs over all sites in the reduced hamiltonian. We assume that an antiferromagnetic gap, Δ , emerges at low temperatures. The mean field equations give

$$\Delta = U(\langle n_{\uparrow} \rangle - \langle n_{\downarrow} \rangle) \quad (6.21)$$

$$1 = \frac{U\Omega}{2\pi} \int_0^{\infty} \frac{kdk}{\sqrt{\left(\frac{\hbar^3 v_F^3 k^3}{\gamma_1^2}\right)^2 + \frac{\Delta^2}{4}}}$$

where $\Omega = (3\sqrt{3}a^2)/2$ is the area of the unit cell. Thus we find

$$\Delta \approx 2 \times \left(\frac{cU\Omega}{2\pi\hbar^2 v_F^2} \right)^3 \gamma_1^4 = 2 \times \left(\frac{c}{\pi\sqrt{3}} \right)^3 \frac{\gamma_1^4 U^3}{\gamma_6^6} \quad (6.22)$$

where $c = \int_0^{\infty} \frac{dx}{\sqrt{1+x^3}} = \left[2\Gamma\left(\frac{1}{3}\right)\Gamma\left(\frac{7}{6}\right) \right] / \sqrt{\pi} \approx 2.8$. We note that U has only been theoretically estimated, but never experimentally measured for graphene. For $\gamma_0 \approx 2.7\text{eV}$, $\gamma_1 \approx 0.4\text{eV}$, and $U \approx 10\text{eV}$, the antiferromagnetic gap $\Delta \approx 18\text{meV}$. This value is lower than the experimental result. The previous analysis, however, neglects the long range part of the interaction. In single layer and in multilayered graphene, exchange processes

associated to the $q \rightarrow 0$ part of the interaction can enhance preexisting gaps, or even trigger their existence^{42,43}. Screening in an ABC trilayer is determined by the polarizability⁴⁴

$$\chi(\vec{q}) = N \sum_{\vec{k}} \left[\frac{1 - \cos(3\theta_{\vec{k}+\vec{q}/2, \vec{k}-\vec{q}/2})}{2} \right] \frac{1}{\hbar^3 v_F^3 / \gamma_1^2 (|\vec{k} + \frac{\vec{q}}{2}|^3 + |\vec{k} - \frac{\vec{q}}{2}|^3)} = \frac{c_\chi \gamma_1^2}{\hbar^3 v_F^3 |\vec{q}|} \quad (6.23)$$

where $c_\chi \approx 0.24$, $N = 4$, and $\theta_{\vec{k}+\vec{q}/2, \vec{k}-\vec{q}/2}$ is the angle between vectors $\vec{k} + \frac{\vec{q}}{2}$ and $\vec{k} - \frac{\vec{q}}{2}$. Using RPA, the effective interaction becomes $v_{\vec{q}} \approx \chi^{-1}(\vec{q})$. The correction to the gap can be written as

$$\delta\Delta(\vec{q}) \approx \sum_{\vec{q}'} v_{\vec{q}-\vec{q}'} \frac{\Delta_0(\vec{q}')}{(\hbar^3 v_F^3 q'^3) / \gamma_1^2} \quad (6.24)$$

We make the ansatz that Δ_0 is independent of \vec{q} . Then, we obtain the approximate scaling equation

$$\frac{\Lambda}{\Delta} \frac{\partial \Delta}{\partial \Lambda} \approx \frac{1}{2\pi c_\chi} \quad (6.25)$$

where Λ is a high momentum cutoff. This equation leads to the new, Δ , including self consistently the exchange effects

$$\Delta_{ex} \approx \Delta \left(\frac{\gamma_1}{\Delta} \right)^{\frac{\alpha}{1+\alpha}} \quad (6.26)$$

where $\alpha \approx \frac{1}{6\pi c\chi}$, and we assume that the high momentum cutoff is such that $\frac{\hbar^3 v_F^3 \Lambda^3}{\gamma_1^2} \approx \gamma_1$.

This analysis leads to an enhancement of the gap by about a factor of two. Finally, the total spin per carbon atom in a given layer is

$$s = \pm \frac{\Delta}{U} \times \mu_B \quad (6.27)$$

where μ_B is Bohr's magneton. For the gap estimated in equation 6.21 we find $s \approx \pm 10^{-3} \mu_B$.

6.7: Discussion and Possible Phase Diagram

To summarize our experimental findings: we observe an insulating state in r-TLG at $n = U_{\perp} = B = 0$, with an energy gap $\Delta(T=0) \sim 42$ meV. This gap can be suppressed by increasing charge density n , a critical temperature $T_c \sim 34$ K, by an interlayer potential U_{\perp} of either polarity, and by an in-plane magnetic field. Among the spatially uniform correlated phases in r-TLG discussed in the literature¹⁷⁻²², only LAF, in which the top and bottom layers have equal number of electrons with opposite spin polarization, is consistent with our experimental observations. For instance, the presence of an energy gap eliminates the mirror-breaking, inversion breaking, interlayer current density wave or layer polarization density wave states²¹, and the zero conductance eliminates the superconductor, quantum spin Hall and quantum anomalous Hall states that host finite (or even infinite) conductance. Furthermore, the symmetrical suppression of the gap by U_{\perp} of

either polarity suggests that charges in the insulating state are layer-balanced, since the device would otherwise exhibit opposite dependence on U_{\perp} of opposite polarities. This excludes all layer-polarized states, including the quantum valley Hall and layer polarization density wave states, and any single particle state that arises from inadvertent doping of one of the surface layers.

Thus, based on the above experimental observations, we identify LAF with broken time reversal and spin rotation symmetries as the most likely candidate among the proposed ground states in r-TLG. Theoretically, an LAF ground state can be justified by the following considerations. The strong screening due to the large density of states in r-TLG leads to very short range Coulomb repulsions among electrons (See section 6.5). For such local interactions, the most likely symmetry-broken states are the LAF and nematic phases, and the gapless and conductive nematic phase is incompatible with our observation of a gapped insulator, leaving LAF as the only viable alternative. Moreover, mean field arguments that generally favor the LAF phase should be more robust in r-TLG than that in bilayer graphene, due to the divergent density of states and stronger interactions near the CNP that suppresses fluctuations. Finally, recent works^{45,46} report formation of magnetic moments in graphene that results from interactions among the p-electrons of graphene in the presence of hydrogen and fluorine atoms and vacancies, thus it is not unreasonable to expect emergent magnetism arising from strong electronic interactions in r-TLG.

Within the mean-field framework, a simple estimate of the LAF gap yields (See section 6.6)

$$\Delta \approx 2 \times \left(\frac{c}{\pi\sqrt{3}} \right)^3 \frac{\gamma_1^4 U^3}{\gamma_0^6} \quad (6.28)$$

where $\gamma_0 \approx 2.7$ eV, $\gamma_1 \approx 0.4$ eV are tight binding parameters, $c \approx 2.8$, and U is the Hubbard onsite interaction. Using these parameters, and substituting the experimentally obtained value $\Delta=42$ meV, we obtain $U \sim 13$ eV, not too different from theoretically predicated values of 5-10 eV^{40,47,48}. Alternatively, the gap can be further enhanced by exchange processes associated to the long range part of the interaction³¹.

A possible phase diagram for charge neutral r-TLG that is consistent with our experimental results, together with schematics for electron configurations, is summarized in figure 6.6. In the absence of external fields, a charge neutral r-TLG is an LAF with broken time reversal and spin rotation symmetries. Increasing U_{\perp} of either polarity pushes electrons to one of the surface layers and suppresses the gap. For sufficiently large $|U_{\perp}|$, all charges reside in either the top or bottom layer, giving rise to a quantum valley Hall (QVH) insulator with broken inversion symmetry. We note that the different broken symmetries of the QVH and LAF states preclude a continuous phase transition between them^{13,49,50}. On the other hand, as B_{\parallel} increases from 0, the competition between the Zeeman and the exchange energies tilts the electron spins, and r-TLG crosses over to the CAF phase. For very large B_{\parallel} , we expect that the electrons eventually form a ferromagnet (F); in the quantum Hall regime, this ferromagnet is analogous to a quantum spin Hall state, with counter-propagating edge states and conductance $\sim 6e^2/h$.⁵¹

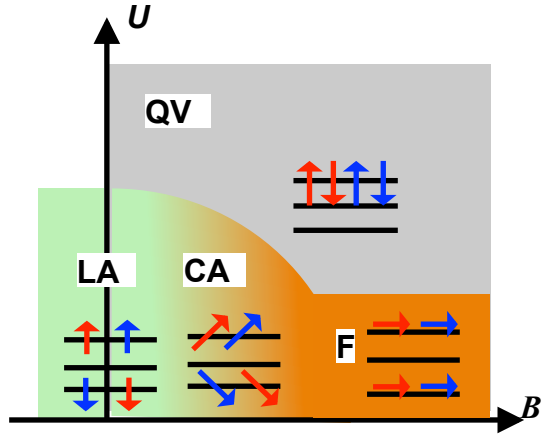


Figure 6.6: Possible phase diagram and schematics of electronic configurations for r-TLG. The blue and red arrows indicate charges from K and K' valleys, respectively. (QVH: quantum valley Hall; LAF: layer antiferromagnet; CAF: canted antiferromagnet; F: Ferromagnet).

6.8: Conclusion and outlook

We have demonstrated that the unusually large density of states and competing symmetries in r-TLG gives rise to phases with different broken symmetries both at zero and finite external fields, with transitions that can be tuned by T , U_{\perp} , $B_{||}$, B_{\perp} and/or n . The natures of the gapped states at zero and finite magnetic field may be explored by future transport, optical and STM studies. Similar measurements can be also extended to ABC stacked tetralayer graphene, which is ~ 1 nm thick, has a quartic dispersion $\varepsilon(k) \sim k^4$ extremely large density of states at the charge neutrality point.

References

Reference

- 1 Lee, Y. *et al.* Competition between spontaneous symmetry breaking and single-particle gaps in trilayer graphene. *Nat Commun* **5** (2014).
- 2 Craciun, M. F. *et al.* Trilayer graphene is a semimetal with a gate-tunable band overlap. *Nat. Nanotechnol.* **4**, 383-388, doi:[10.1038/nnano.2009.89](https://doi.org/10.1038/nnano.2009.89) (2009).
- 3 Lui, C. H. *et al.* Imaging stacking order in few-layer graphene. *Nano Lett.* **11**, 164-169 (2011).
- 4 Ferrari, A. C. *et al.* Raman spectrum of graphene and graphene layers. *Phys. Rev. Lett.* **97**, 187401 (2006).
- 5 Liu, G., Velasco, J., Bao, W. Z. & Lau, C. N. Fabrication of graphene p-n-p junctions with contactless top gates. *Appl. Phys. Lett.* **92**, 203103 (2008).
- 6 Velasco, J., Liu, G., Bao, W. Z. & Lau, C. N. Electrical transport in high-quality graphene pnp junctions. *New J. Phys.* **11**, 095008, doi:[09500810.1088/1367-2630/11/9/095008](https://doi.org/10.1088/1367-2630/11/9/095008) (2009).
- 7 Moser, J., Barreiro, A. & Bachtold, A. Current-induced cleaning of graphene. *Appl. Phys. Lett.* **91**, 163513 (2007).
- 8 Bao, W. *et al.* Evidence for a spontaneous gapped state in ultraclean bilayer graphene. *Proc. Nat. Acad. Sci.* **109**, 10802-10805, doi:[10.1073/pnas.1205978109](https://doi.org/10.1073/pnas.1205978109) (2012).
- 9 Koshino, M. & McCann, E. Trigonal warping and Berry's phase $N\pi$ in ABC-stacked multilayer graphene. *Phys. Rev. B* **80**, 165409, doi:[10.1103/PhysRevB.80.165409](https://doi.org/10.1103/PhysRevB.80.165409) (2009).
- 10 Guinea, F., Castro Neto, A. H. & Peres, N. M. R. Electronic states and Landau levels in graphene stacks. *Phys. Rev. B* **73**, 245426 (2006).
- 11 Avetisyan, A. A., Partoens, B. & Peeters, F. M. Stacking order dependent electric field tuning of the band gap in graphene multilayers. *Phys. Rev. B* **81**, 115432, doi:[10.1103/PhysRevB.81.115432](https://doi.org/10.1103/PhysRevB.81.115432) (2010).
- 12 Aoki, M. & Amawashi, H. Dependence of band structures on stacking and field in layered graphene. *Sol. State Commun.* **142**, 123-127 (2007).

- 13 Zhang, F., Sahu, B., Min, H. K. & MacDonald, A. H. Band structure of ABC-stacked graphene trilayers. *Phys. Rev. B* **82**, 035409, doi:[10.1103/PhysRevB.82.035409](https://doi.org/10.1103/PhysRevB.82.035409) (2010).
- 14 Zou, K., Zhang, F., Capp, C., MacDonald, A. H. & Zhu, J. Transport Studies of Dual-Gated ABC and ABA Trilayer Graphene: Band Gap Opening and Band Structure Tuning in Very Large Perpendicular Electric Fields. *Nano Lett.* **13**, 369-373, doi:[10.1021/nl303375a](https://doi.org/10.1021/nl303375a) (2013).
- 15 Lui, C. H., Li, Z., Mak, K. F., Cappelluti, E. & Heinz, T. F. Observation of an electrically tunable band gap in trilayer graphene. *Nat. Phys.* **7**, 944 (2011).
- 16 Lui, C. H., Li, Z., Mak, K. F., Cappelluti, E. & Heinz, T. F. Observation of an electrically tunable band gap in trilayer graphene. *Nat. Phys.* **7**, 944 (2011).
- 17 Castro, E. V., Pilar Lopez-Sancho, M. & Vozmediano, M. A. H. Vacancy induced zero energy modes in graphene stacks: The case of ABC trilayer. *Solid State Commun.* **152**, 1483-1488, doi:[10.1016/j.ssc.2012.04.027](https://doi.org/10.1016/j.ssc.2012.04.027) (2012).
- 18 Olsen, R., van Gelderen, R. & Smith, C. M. Ferromagnetism in ABC-stacked trilayer graphene. *Phys. Rev. B* **87**, doi:[10.1103/PhysRevB.87.115414](https://doi.org/10.1103/PhysRevB.87.115414) (2013).
- 19 Liu, H., Jiang, H., Xie, X. C. & Sun, Q.-f. Spontaneous spin-triplet exciton condensation in ABC-stacked trilayer graphene. *Phys. Rev. B* **86**, 085441, doi:[10.1103/PhysRevB.86.085441](https://doi.org/10.1103/PhysRevB.86.085441) (2012).
- 20 Jung, J. & MacDonald, A. H. Gapped broken symmetry states in ABC trilayer graphene. *preprint*, arXiv:1208.0116 (2012).
- 21 Cvetkovic, V. & Vafeek, O. Topology and symmetry breaking in ABC trilayer graphene. *preprint*, arXiv:1210.4923 (2012).
- 22 Scherer, M. M., Uebelacker, S., Scherer, D. D. & Honerkamp, C. Interacting electrons on trilayer honeycomb lattices. *Phys. Rev. B* **86**, 155415, doi:[10.1103/PhysRevB.86.155415](https://doi.org/10.1103/PhysRevB.86.155415) (2012).
- 23 Velasco, J. *et al.* Transport spectroscopy of symmetry-broken insulating states in bilayer graphene. *Nature Nanotechnol.* **7**, 156-160 (2012).
- 24 Velasco Jr., J. *et al.* Transport Measurement of Landau level Gaps in Bilayer Graphene with Layer Polarization Control. *Nano Lett.* **14**, 1324-1328 (2014).
- 25 Jia, J., Gorbar, E. V. & Gusynin, V. P. Gap generation in ABC-stacked multilayer graphene: Screening versus band flattening. *Phys. Rev. B* **88**, 205428 (2013).

- 26 Freitag, F., Trbovic, J., Weiss, M. & Schonenberger, C. Spontaneously gapped ground state in suspended bilayer graphene. *Phys. Rev. Lett.* **108**, 076602 (2012).
- 27 Bao, W. *et al.* Stacking-Dependent Band Gap and Quantum Transport in Trilayer Graphene. *Nat. Phys.* **7**, 948-952 (2011).
- 28 Ferrell, R. A. Temperature Dependence of the Superconductivity Energy Gap. *Zeitschrift fur Physik* **182**, 1 (1964).
- 29 van Gelderen, R., Olsen, R. & Smith, C. M. Screening in multilayer graphene. *preprint*, arXiv:1304.5501 (2013).
- 30 Koshino, M. Interlayer screening effect in graphene multilayers with ABA and ABC stacking. *Physical Review B* **81**, 125304, doi:10.1103/PhysRevB.81.125304 (2010).
- 31 Min, H., Hwang, E. H. & Das Sarma, S. Polarizability and screening in chiral multilayer graphene. *Phys. Rev. B* **86**, 081402, doi:10.1103/PhysRevB.86.081402 (2012).
- 32 McCann, E. & Koshino, M. The electronic properties of bilayer graphene. *Reports on Progress in Physics* **76**, 1-28, doi:10.1088/0034-4885/76/5/056503 (2013).
- 33 Zhang, F., Sahu, B., Min, H. & MacDonald, A. Band structure of stacked graphene trilayers. *Physical Review B* **82**, 035409 (2010).
- 34 Nilsson, J., Castro Neto, A., Peres, N. & Guinea, F. Electron-electron interactions and the phase diagram of a graphene bilayer. *Physical Review B* **73**, 214418 (2006).
- 35 Zhang, F., Jung, J., Fiete, G., Niu, Q. & MacDonald, A. Spontaneous Quantum Hall States in Chirally Stacked Few-Layer Graphene Systems. *Physical Review Letters* **106**, 156801 (2011).
- 36 Jeil, J. & MacDonald, A. H. Gapped broken symmetry states in ABC-stacked trilayer graphene. *Physical Review B: Condensed Matter & Materials Physics* **88**, 075408-075401-075408-075407, doi:10.1103/PhysRevB.88.075408 (2013).
- 37 Throckmorton, R. & Vafeek, O. Fermions on bilayer graphene: Symmetry breaking for. *Physical Review B* **86**, 115447 (2012).
- 38 Lemonik, Y., Aleiner, I. & Fal'ko, V. Competing nematic, antiferromagnetic, and spin-flux orders in the ground state of bilayer graphene. *Physical Review B* **85**, 245451 (2012).

- 39 Lang, T. *et al.* Antiferromagnetism in the Hubbard Model on the Bernal-Stacked Honeycomb Bilayer. *Physical Review Letters* **109**, 126402 (2012).
- 40 Verges, J. A., SanFabián, E., Chiappe, G. & Louis, E. Fit of Pariser-Parr-Pople and Hubbard model Hamiltonians to charge and spin states of polycyclic aromatic hydrocarbons. *Phys. Rev. B* **81**, 085120 (2010).
- 41 Schüler, M., Rösner, M., Wehling, T., Lichtenstein, A. & Katsnelson, M. Optimal Hubbard Models for Materials with Nonlocal Coulomb Interactions: Graphene, Silicene, and Benzene. *Physical Review Letters* **111**, 036601 (2013).
- 42 Khveshchenko, D. Ghost Excitonic Insulator Transition in Layered Graphite. *Physical Review Letters* **87**, 246802 (2001).
- 43 Gorbar, E., Gusynin, V., Miransky, V. & Shovkovy, I. Magnetic field driven metal-insulator phase transition in planar systems. *Physical Review B* **66**, 045108 (2002).
- 44 van Gelderen, R., Olsen, R. & Smith, C. M. Screening in multilayer graphene. *Physical Review B* **88**, 115414 (2013).
- 45 Nair, R. R. *et al.* Spin-half paramagnetism in graphene induced by point defects. *Nat. Phys.* **8**, 199-202, doi:10.1038/nphys2183 (2012).
- 46 Nair, R. R. *et al.* Dual origin of defect magnetism in graphene and its reversible switching by molecular doping. *Nat. Commun.* **4**, 2010, doi:10.1038/ncomms3010 (2013).
- 47 Wehling, T. O. *et al.* Strength of Effective Coulomb Interactions in Graphene and Graphite. *Phys. Rev. Lett.* **106**, 236805 (2011).
- 48 Schüler, M., Rösner, M., Wehling, T. O., Lichtenstein, A. I. & Katsnelson, M. I. *Phys. Rev. Lett.* **111**, 036601 (2013).
- 49 Jung, J., Zhang, F. & MacDonald, A. H. Lattice theory of pseudospin ferromagnetism in bilayer graphene: Competing interaction-induced quantum Hall states. *Phys. Rev. B* **83**, 115408, doi:10.1103/PhysRevB.83.115408 (2011).
- 50 Zhang, F., Tilahun, D. & MacDonald, A. H. Hund's rules for the N=0 Landau levels of trilayer graphene. *Phys. Rev. B* **85**, 165139, doi:10.1103/PhysRevB.85.165139 (2012).
- 51 Maher, P. *et al.* Evidence for a spin phase transition at charge neutrality in bilayer graphene. *Nat. Phys.* **9**, 154-158 (2013).

Chapter 7 : Quantum Hall state in ABC Trilayer graphene

Quantum Hall (QH) effect is a two-dimensional (2D) phenomenon that results from Landau quantization of electrons. The isolation of 2D crystals has enabled observation of novel QH phenomena, such as the “half-integer” quantum Hall effect in graphene^{1,2} that confirmed the massless and massive characters of Dirac electrons in graphene and its few-layer counterparts¹⁻⁶. More fundamentally, electron-electron interactions can lead to additional integer or fractional QH plateaus not expected by Landau quantization alone^{7,8}. In these systems the additional degrees of freedom (spin and valley) along with the Dirac nature of electrons may leads to new types of exotic states such as skyrmions and Wigner crystal⁹⁻¹⁸, and the $\nu=0$ state with unusual spin and valley textures¹⁹⁻³¹ which does not have a counterpart in conventional semiconducting two-dimensional electron gases. With the advent of high mobility samples that may be either suspended^{32,33} or supported on boron-nitride (BN) substrates³⁴, and advanced device geometry such as dual-gates or split top gates, few-layer graphene is emerging as platforms for discovering and understanding QH-related phenomena, with unprecedented tunability and control.

In this chapter we will discuss transport on high mobility dual-gated rhombohedral-stacked trilayer graphene(r-TLG) devices in the transitions and crossings between symmetry-broken Landau Levels (LL) via careful control of U , B and n . Section 7.1 describes the fabrication and characterization of the high mobility dual-gated ABC TLG devices. Section 7.2 and 7.3 present the QH states in singly-gated device and the

degeneracy in the orbital degrees of freedom is broken prior to that in spin/layer flavors, and all integer plateaus of the zeroth LL in the hole-doped regime are resolved in high B in dual-gated device, respectively. In section 7.4, we discuss the determination of the LL gaps for the filling factor $\nu=-2$ and -3 states scale with B and \sqrt{B} , respectively. In section 7.5, we discuss the remote hopping term γ_4 effect in r-TLG on splitting of the orbital degeneracy of the lowest LL.

7.1: Device characterization

r-TLG sheets are mechanically exfoliated onto Si/SiO₂ wafers and selected by color contrast in an optical microscope, Raman spectroscopy^{35,36} and/or observation of weak anti-localization in small magnetic field. Suspended devices with Cr/Au [10nm/150nm] electrodes and contactless top gates as shown in figure 7.1a with 300nm height are fabricated using a combination of multi-level lithography^{37,38} and three-angle metal deposition at -45° , 0° and 45° . And then the SiO₂ layer are partially removed with HF etching. The devices are measured at $T=260\text{mK}$ using standard lock-in techniques. In these devices, the interlayer potential U_\perp and charge density n can be independently controlled, $n = (C_{bg}V_{bg} + C_{tg}V_{tg})/e$ and $U_\perp = (C_{bg}V_{bg} - C_{tg}V_{tg})d/2\epsilon_0$. Here ϵ_0 the permittivity of vacuum, $d=0.67$ nm is the distance between the outmost layers, V_{bg} and V_{tg} are the voltage applied to back gate and top gate, respectively, and C_{bg} (C_{tg}) is the capacitance per unit area between graphene and back (top) gate. The capacitance values C_{bg}/e (C_{tg}/e) are estimated from geometric consideration and/or Landau fan diagrams, and range from 1×10^{10} to 7×10^{10} cm⁻². Similar data are observed in two devices. Here we

present data from a device with length and width $\sim 1.1 \mu\text{m}$.

Figure 7.1b displays the two-terminal conductance G as a function of back gate V_{bg} before (red curve) and after (blue curve) current annealing. After annealing, the curve becomes ‘V’-shaped, with charge neutrality close to zero, drastically lower minimum conductance, and field effect mobility $42,000 \text{ cm}^2/\text{Vs}$.

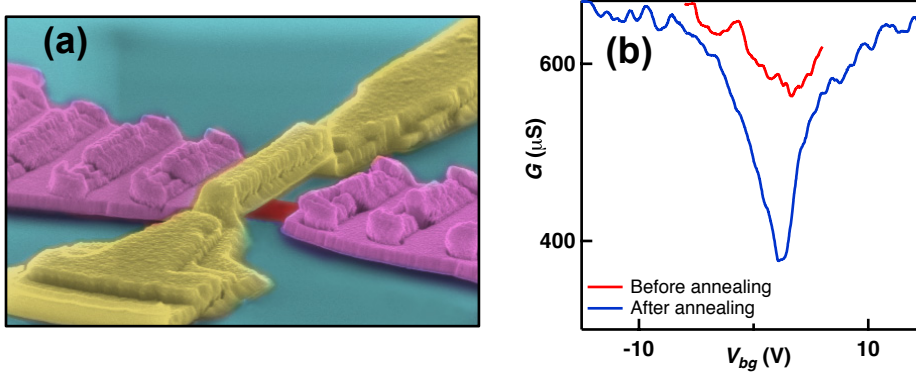


Figure 7.1: Device image and current annealing (a). SEM image of a dual-gated TLG device. (b) Device conductance G vs V_{bg} before and after current annealing.

7.2: Quantum Hall state of ABC TLG using a single gate

r-TLG is such a QH system with chiral charge carriers, and very flat bands near the charge neutrality point that result in strong electronic interactions. In the quantum

Hall regime, the LL energies are $E_N = \pm \frac{(2\hbar v_F e B)^{3/2}}{\gamma_1^2} \sqrt{N(N-1)(N-2)}$ where N is an

integer denoting the LL index, e the electron charge, $v_F \sim 10^6 \text{ m/s}$ the Fermi velocity of single layer graphene, $\gamma_1 \sim 0.3 \text{ eV}$ the interlayer hopping energy, and h Planck’s constant. The

degeneracy between the $N=0, 1$ and 2 LLs, together with the spin and valley degrees of freedom, yield the 12-fold degeneracy of the lowest LL, and give rise to plateaus at filling factors $\nu=\pm 6, \pm 10, \pm 14\dots$. This 12-fold degeneracy is expected to be lifted by interactions and/or single particle effects, leading to incompressible states at intermediate fillings^{39,40}. The order at which the degeneracy is broken reflects the underlying competing symmetries and competition between interactions and single particle effects. Prior works have reported resolution of several symmetry-broken QH states^{41,42}, albeit only in single-gated samples where the interlayer potential U_i and charge density n are not independently controlled.

High quality r-TLG devices are intrinsically insulating with a large interaction-induced gap, ~ 42 meV. This gapped insulating state is identified to be a layer antiferromagnet with broken time reversal and spin rotation symmetries⁴³. As B increases from 0, the insulating state evolves smoothly into the $\nu=0$ QH state, which is most likely as a canted antiferromagnetic phase⁴³, similar to that observed in bilayer graphene^{22,28-30}. Shubnikov-de Haas oscillations appear at B as low as 0.2T, and conductance plateaus become quantized at $B>3$ T. Figure 7.2a plots two terminal conductance $G(B, \nu)$ in units of e^2/h with top gate disconnected or grounded (these two configurations yield identical results). QH plateaus appear as vertical bands in the figure. As B increases, QH plateaus at filling factors $\nu=-5$ and -3 are resolved first, followed by -1 and -2 . This can also be seen in the line traces $G(\nu)$: only the $\nu=-3$ plateau are fully resolved at $B=4.5$ T, whereas additional plateaus at $\nu=-2$ and -1 are resolved at $B=5.5$ T as shown in figure 7.2b. This observation is consistent with the prior work using singly-gated devices⁴¹.

The spontaneous resolution of the $\nu=0$ state corresponds to the breaking of a combination of spin and valley degrees of freedom. Apart from this, six degeneracies remain in the zeroth LL in the hole-doped regime: two associated with the spin-valley flavors and three with the orbital pseudo-spin. The remaining broken symmetry QH states can be classified in terms of two sets of Hund's rule. In the first case, if the spin-valley

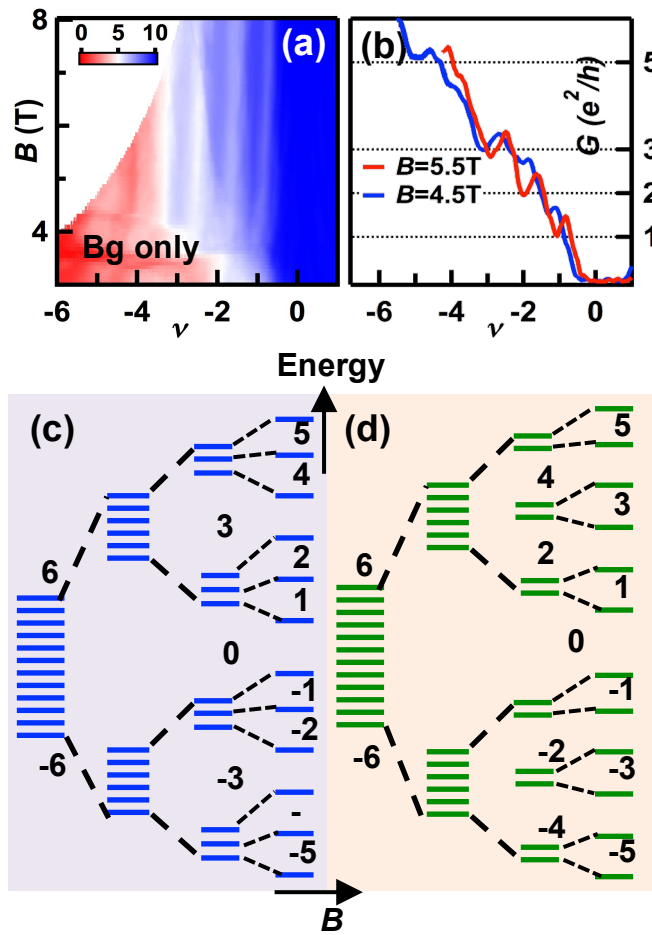


Figure 7.2: Transport data and schematics of orders of symmetry breaking (a). $G(B, \nu)$ of a r-TLG device with only back gate engaged, while top gate is disconnected or grounded. (b). Line traces $G(\nu)$ at $B=4.5$ T and 5.5 T, respectively. (c-d). Schematics of orders of symmetry breaking in r-TLG in the QH regime.

pseudo-spin is maximized before the LL orbital pseudo-spin, then $\nu=-3$ plateau should appear before $\nu=-1,-2$ or $\nu=-4,-5$ plateaus, as shown in figure 7.2c; this is also the anticipated scenario for spin and valley independent SU(4) interactions^{8,44} and appears to be supported by data from singly-gated devices in this as shown in figure 7.2a and 7.2b and prior experiments⁴¹. Conversely, if the orbital pseudospin is maximized first, then the $\nu=-3$ state should be resolved last; this second set of Hund's rule is depicted in figure 7.2d.

7.3: Quantum Hall state of ABC TLG using dual gate

In singly-gated devices, U_{\perp} is not controlled but scales with n . When both top and back gates are engaged so that both U_{\perp} and n can be independently modulated, a qualitatively different picture emerges. Figure 7.3a and 7.3b plots $G(B, \nu)$ at $U_{\perp}=0$ and -20 mV, respectively, and line traces at $B=5T$ are shown in figure 7.3c and 7.3d. In the absence of interlayer bias, the plateaus at $\nu=-6, -4$ and -2 are fully resolved at $B=5T$, while the odd integer plateaus $\nu=-3$ and -1 appear only as small shoulders even at $B=8T$ (Figure 7.3a-b). This suggests that the orbital pseudospin is maximized first, reflecting the second set of Hund's rule. At finite U_{\perp} , we find that the exact sequence of plateaus depends on U_{\perp} , thus one cannot infer the symmetries associated with intermediate fillings from singly-gated devices. For instance, at $U_{\perp}=-20$ mV, the $\nu=-3$ (but not the $\nu=-2$) state is resolved (Figure 7.3c-d), in apparent agreement with the first set of Hund's rule.

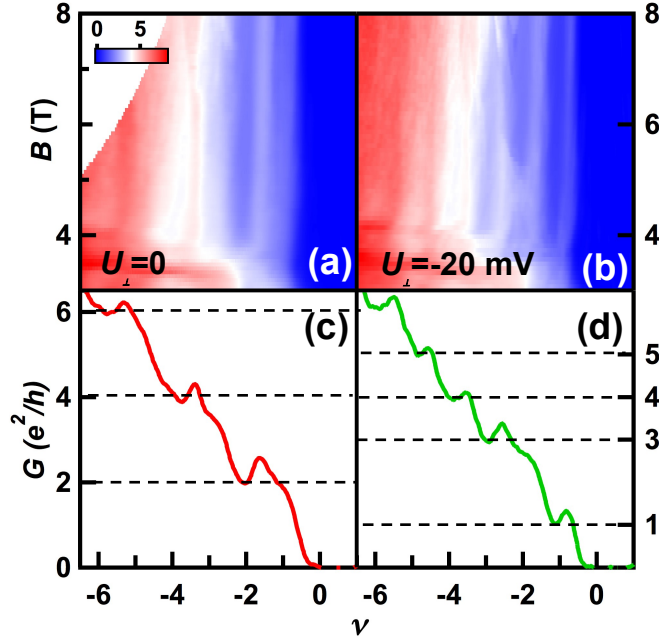


Figure 7.3: Transport data of ABC trilayer graphene device (a-c). $G(B, \nu)$ in units of e^2/h at $U_{\perp}=0$, and line traces $G(\nu)$ at $B=5T$. (b-d). Similar data at $U_{\perp}=-20$ mV.

To further investigate the plateaus' dependence on U_{\perp} we measure $G(U_{\perp}, \nu)$ at constant B . The resolved QH plateaus appear as an array of bands centered at integer values of ν , with a striking network of staggered “hexagons” as shown in figure 7.4a-b. The device conductance is properly quantized $\nu e^2/h$, *except* at certain critical $U_{\perp c}$ values that yield the horizontal “ridges” of the hexagons. For instance, at $\nu=-3$, G is quantized at $3e^2/h$ except at $U_{\perp c}=0$ and -58 mV (Figure 7.4c, blue curve); at $\nu=-2$ state, quantization is lost at $U_{\perp c} \sim \pm 18$ mV (red curve). $U_{\perp c}$ values are indicated by \blacksquare and \blacktriangle for $\nu=-2$ and -3 , respectively. Consequently, a given plateau is resolved (unresolved) if $G(\nu)$ is taken at $U_{\perp} \neq U_{\perp c}$ ($U_{\perp} = U_{\perp c}$), *e.g.* the line traces in figure 7.3b and 7.3d are effectively taken along the red and green arrows in figure 7.4b, respectively.

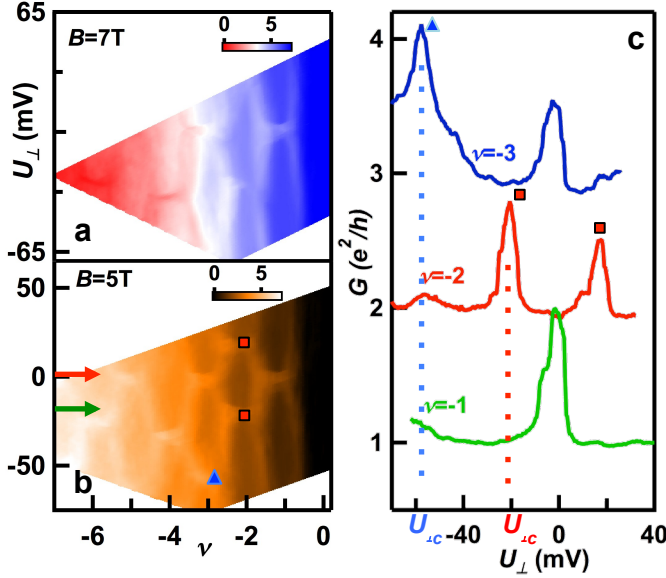


Figure 7.4: Transport data of ABC trilayer graphene device (a-b). $G(U_{\perp}, \nu)$ in units of e^2/h at $B=7T$ and $5T$, respectively. The arrows indicate line traces along which Fig. 2c and 2d would be taken. (c). Line traces $G(U_{\perp})$ at $B=5T$ and $\nu=-1, -2$, and -3 . The triangles and squares mark $U_{\perp,c}$ values at which G is not quantized.

7.4: Discussion of crossing between symmetry broken LL and energy gap

As B increases, the sizes of these hexagons grow accordingly. In figure 7.5a, the critical $U_{\perp,c}$ values for $\nu=-2$ and -3 states are plotted as a function of B . Interestingly, while $U_{\perp,c,\nu=-2}$ scales linearly with B , $U_{\perp,c,\nu=-3}$ is sub-linear in B with a \sqrt{B} -dependence. Such linear B and \sqrt{B} dependence are reminiscent of LL gaps that are expected for monolayer and bilayer graphene.

To account for the hexagon patterns, we use a simple model of crossings between symmetry-broken Landau levels⁴⁵⁻⁴⁷ whose energies depend on both U_{\perp} and B . In the two-band model, in the $N=0$ space, only the A-sublattice of the top layer and the B-sublattice of the bottom layer are relevant for low-energy considerations. We thus ignore

the contribution of the middle layer, and treat layer, valley and sublattice indices as equivalent. Hence, energies of LLs that are partially localized to the top (bottom) layer increase (decrease) with increasing U_{\perp} ; these two sets of LLs cross whenever

$$\varepsilon_{n_1,T} - \varepsilon_{n_2,B} = eU_{\perp}, \quad (7.1)$$

where $\varepsilon_{n_1,T}$ ($\varepsilon_{n_2,B}$) is the energy of the n_1 -th (n_2 -th) LL level localized to the top (bottom) layer. These multiple LL crossings, combined with LL broadening that smears the crossing points, gives rise to the observed hexagon features. Thus, G is quantized everywhere at the standard value ve^2/h , *except* at each crossing point. A schematic of the energetic diagram is shown in figure 7.5b, and the yellow highlighted numbers denote the expected conductance values. We note that based on this model, the plateau sequence at finite U_{\perp} , including those in singly-gated devices, arises at least partly from LL crossings and cannot be used to determine the symmetries associated with intermediate filling factors. In equation 7.1, we ignore any contribution of screening, by assuming that the actual interlayer potential is the same as the externally imposed potential calculated from gate voltages. This is based on the expectation that screening arising from higher ($N > 2$) LLs is suppressed in the high magnetic field limit, due to the $B^{3/2}$ scaling of LL gaps⁴⁰.

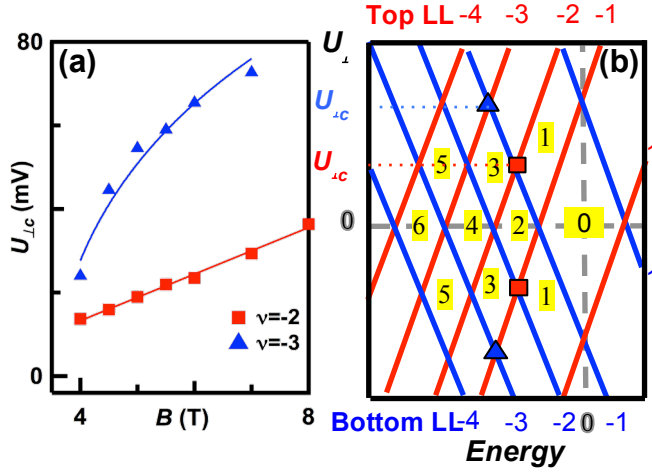


Figure 7.5: The energy gap of LLs and Schematic diagram of LL (a). Experimentally measured $U_{\perp,c}$ values as a function of B for $\nu = -2$ and -3 states, respectively. Red line: a linear fit with a slope ~ 5.6 meV/T. Blue line: a fit to Eq. (3). (b). Schematic diagram of LL energies under U_{\perp} . The red (blue) numbers indicate the indices of LLs with top (bottom) quantum numbers. The highlighted numbers denote the expected conductance values.

Using this model, we can determine LL gaps Δ from $U_{\perp,c}$ at the LL crossing points, where the differences in LL energies are compensated by electrostatic energy. For the $\nu = -2$ state, the first crossing arises from the crossing between the $n_{1,B} = -1$ and $n_{2,T} = -2$ LLs, thus the LL gap $\Delta_{\nu=-2}$ is simply the potential $U_{\perp,c,\nu=-2}$. The data points fall on a straight line as shown in figure 7.5a, yielding a best-fit slope ~ 5.6 mV/T.

For the $\nu = -3$ state, $U_{\perp,c,\nu=-3}(B)$ is markedly sublinear. In this case the first crossing at finite U_{\perp} occurs between the non-adjacent $n_{1,B} = -1$ and $n_{2,T} = -3$ LLs, as indicated by the blue triangles in figure 7.5b. Hence

$$\begin{aligned}
U_{\perp c, \nu=-3} &= \varepsilon_{n_1=-3, T} - \varepsilon_{n_2=-1, B} = \Delta_{\nu=-3} + \Delta_{\nu=-2} \\
&= \Delta_{\nu=-3} + U_{\perp c, \nu=-2}
\end{aligned} \tag{7.2}$$

and is expected to contain a linear component from the $\Delta_{\nu=-2}$ term. We therefore fit $U_{\perp c, \nu=-3}(B)$ to the equation

$$U_{\perp c, \nu=-3} = aB + c\sqrt{B - B_0} \ , \tag{7.3}$$

yielding fitting parameters $a=6.1\text{mV/T}$, $c=20\text{mV/T}^{1/2}$, and $B_0=3.9\text{T}$. The last term in equation 7.3 suggests a \sqrt{B} dependence of the $\nu=-3$ state, which in turn indicates that the $\nu=-3$ gap arises from Coulomb interactions.

To sum our experimental observations: interlay potential U_{\perp} induces crossing between symmetry-broken LLs, and conductance quantization is lost at the crossing points where the LL gaps are compensated by the electrostatic energy. As a result, the exact sequence of plateau resolution is U_{\perp} -dependent. For charge balanced r-TLG, we first resolve the $\nu=-2$ plateau whose energy gap scales linearly with B , followed by the $\nu=-3$ state whose gap appears to scale with \sqrt{B} . Our observation clearly indicates the LL(orbital) pseudospin degree of freedom is lifted before the valley pseudospin; the contrasting linear B and \sqrt{B} dependence for the $\nu=-2$ and $\nu=-3$ gaps suggest different mechanisms of gap generation, *e.g.* gaps induced by single particle effects and electronic interactions.

7.5: Discussion of the remote hopping term γ_4 effect

To account for the above observation, we note that the remote hopping term γ_4 in r-TLG, which is the interlayer hopping energy between stacked-unstacked sublattices, may lead to splitting of the orbital degeneracy of the lowest LL. Its effect can be captured in an effective two-band model⁴⁸, evaluated in the perturbation theory

$$H_{\gamma_4} = \frac{2v_4v_F}{\gamma_1} \begin{pmatrix} \pi^+\pi & 0 \\ 0 & \pi\pi^+ \end{pmatrix} \quad (7.4)$$

where $v_4 = \sqrt{3}a\gamma_1/2\hbar$, $a=0.246$ nm is the lattice constant, and $\pi=\pm p_x+ip_y$. In the presence of B , H_{γ_4} leads to a splitting of the $N=0, 1$ and 2 LL orbitals. Such splitting of the orbital pseudospin has an energy gap Δ_{γ_4} that scales linearly with B , $\sim 0.24B$ meV, and leads to QH plateaus at $\nu=\pm 2$, as observed experimentally. The larger experimental value is likely due to screening of the electric field due to residual impurities and/or partially occupied lowest LL, whose effects are not taken into account. On the other hand, the appearance of other intermediate plateaus, such as those at ± 3 , cannot be accounted for by Landau quantization alone, and must arise from electronic interactions.

The valley pseudospin gap Δ_V is estimated to be $\beta \frac{e^2}{\epsilon l_B} + \frac{U_{\perp}}{2}$, where $\beta \sim \sqrt{\pi/2}$, ϵ is the dielectric constant of the environment, and l_B is the magnetic length^{40,44}. For suspended graphene, $\Delta_V \sim 56\sqrt{B}$ meV. The \sqrt{B} -scaling is consistent with our experimental results.

Taken together, our data strongly suggest that the $\nu=-2$ and -4 QH states are orbital pseudospin polarized canted antiferromagnetic states, whereas the $\nu=-1, -3$ and -5 states are layer/spin polarized.

Conclusion

In conclusion, we demonstrate that in the zeroth LL of charge-balanced r-TLG, the LL orbital pseudospin degeneracy is broken before the valley pseudospin, leading to the appearance of QH states at filling factors at even integers prior to those at odd integers. We also demonstrate that energy gaps of QH states can in principle be determined from LL crossing points. Finally, our results shed light on other layered 2D systems such as bilayer graphene and double-layer QH systems.

References

- 1 Zhang, Y. B., Tan, Y. W., Stormer, H. L. & Kim, P. Experimental observation of the quantum Hall effect and Berry's phase in graphene. *Nature* **438**, 201-204 (2005).
- 2 Novoselov, K. S. *et al.* Two-dimensional gas of massless Dirac fermions in graphene. *Nature* **438**, 197-200 (2005).
- 3 Das Sarma, S., Adam, S., Hwang, E. H. & Rossi, E. Electronic transport in two dimensional graphene. *Rev. Mod. Phys.* **83**, 407 (2011).
- 4 Fuhrer, M. S., Lau, C. N. & MacDonald, A. H. Graphene: Materially Better Carbon. *MRS Bull.* **35**, 289-295 (2010).
- 5 Peres, N. M. R., Guinea, F. & Castro Neto, A. H. Electronic properties of two-dimensional carbon. *Annals Of Physics* **321**, 1559-1567 (2006).
- 6 Castro Neto, A. H., Guinea, F., Peres, N. M. R., Novoselov, K. S. & Geim, A. K. The electronic properties of graphene. *Rev. Mod. Phys.* **81**, 109-162, doi:[10.1103/RevModPhys.81.109](https://doi.org/10.1103/RevModPhys.81.109) (2009).
- 7 Nomura, K. & MacDonald, A. H. Quantum Hall ferromagnetism in graphene. *Phys. Rev. Lett.* **96**, 256602 (2006).
- 8 Barlas, Y., Cote, R., Nomura, K. & MacDonald, A. H. Intra-Landau-level cyclotron resonance in bilayer graphene. *Phys. Rev. Lett.* **101**, 097601, doi:[10.1103/PhysRevLett.101.097601](https://doi.org/10.1103/PhysRevLett.101.097601) (2008).
- 9 Abanin, D. A., Parameswaran, S. A. & Sondhi, S. L. Charge 2e Skyrmions in Bilayer Graphene. *Phys. Rev. Lett.* **103**, 076802, doi:[10.1103/PhysRevLett.103.076802](https://doi.org/10.1103/PhysRevLett.103.076802) (2009).
- 10 Cote, R., Jobidon, J. F. & Fertig, H. A. Skyrme and Wigner crystals in graphene. *Phys. Rev. B*, 085309-085301-085313, doi:[10.1103/PhysRevB.78.085309](https://doi.org/10.1103/PhysRevB.78.085309) (2008).
- 11 Cote, R., Luo, W. C., Petrov, B., Barlas, Y. & MacDonald, A. H. Orbital and interlayer skyrmion crystals in bilayer graphene. *Phys. Rev. B* **82**, 245307, doi:[10.1103/PhysRevB.82.245307](https://doi.org/10.1103/PhysRevB.82.245307) (2010).
- 12 Doucot, B., Goerbig, M. O., Lederer, P. & Moessner, R. Entanglement skyrmions in multicomponent quantum Hall systems. *Phys. Rev. Lett.* **78**, 195327, doi:[10.1103/PhysRevB.78.195327](https://doi.org/10.1103/PhysRevB.78.195327) (2008).

- 13 Lu, C.-K. & Herbut, I. F. Zero Modes and Charged Skyrmions in Graphene Bilayer. *Phys. Rev. Lett.* **108**, 266402, doi:[10.1103/PhysRevLett.108.266402](https://doi.org/10.1103/PhysRevLett.108.266402) (2012).
- 14 Shibata, N. & Nomura, K. Fractional Quantum Hall Effects in Graphene and Its Bilayer. *J. Phys. Soc. Jpn.* **78**, 104708, doi:[10.1143/jpsj.78.104708](https://doi.org/10.1143/jpsj.78.104708) (2009).
- 15 Toke, C., Lammert, P. E., Crespi, V. H. & Jain, J. K. Fractional quantum Hall effect in graphene. *Phys. Rev. B* **74**, 235417, doi:[10.1103/PhysRevB.74.235417](https://doi.org/10.1103/PhysRevB.74.235417) (2006).
- 16 Yang, K., Sarma, S. D. & MacDonald, A. H. Collective modes and skyrmion excitations in graphene SU(4) quantum Hall ferromagnets. *Phys. Rev. B* **74**, 075423 (2006).
- 17 Cote, R., Luo, W., Petrov, B., Barlas, Y. & MacDonald, A. H. Orbital and interlayer skyrmion crystals in bilayer graphene. *Phys. Rev. B* **82**, 245307, doi:[10.1103/PhysRevB.82.245307](https://doi.org/10.1103/PhysRevB.82.245307) (2010).
- 18 Young, A. F. *et al.* Spin and valley quantum Hall ferromagnetism in graphene. *Nat. Phys.* **8**, 550-556, doi:[10.1038/nphys2307](https://doi.org/10.1038/nphys2307) (2012).
- 19 Jung, J., Zhang, F. & MacDonald, A. H. Lattice theory of pseudospin ferromagnetism in bilayer graphene: Competing interaction-induced quantum Hall states. *Phys. Rev. B* **83**, 115408, doi:[10.1103/PhysRevB.83.115408](https://doi.org/10.1103/PhysRevB.83.115408) (2011).
- 20 Min, H., Borghi, G., Polini, M. & MacDonald, A. H. Pseudospin magnetism in graphene. *Phys. Rev. B* **77**, 041407, doi:[10.1103/PhysRevB.77.041407](https://doi.org/10.1103/PhysRevB.77.041407) (2008).
- 21 Nagaosa, N., Sinova, J., Onoda, S., MacDonald, A. H. & Ong, N. P. Anomalous Hall effect. *Rev. Mod. Phys.* **82**, 1539-1592, doi:[10.1103/RevModPhys.82.1539](https://doi.org/10.1103/RevModPhys.82.1539) (2010).
- 22 Zhang, F., Jung, J., Fiete, G. A., Niu, Q. A. & MacDonald, A. H. Spontaneous quantum Hall states in chirally stacked few-layer graphene systems. *Phys. Rev. Lett.* **106**, 156801, doi:[10.1103/PhysRevLett.106.156801](https://doi.org/10.1103/PhysRevLett.106.156801) (2011).
- 23 Zhang, F. & MacDonald, A. H. Distinguishing Spontaneous Quantum Hall States in Graphene Bilayers. *Phys. Rev. Lett.* **108**, 186804 (2012).
- 24 Zhang, F., Min, H. & MacDonald, A. H. Competing ordered states in bilayer graphene. *Phys. Rev. B* **86**, 155128 (2012).

- 25 Zhang, F., Min, H., Polini, M. & MacDonald, A. H. Spontaneous inversion symmetry breaking in graphene bilayers. *Phys. Rev. B* **81**, 041402 (R), doi:[10.1103/PhysRevB.81.041402](https://doi.org/10.1103/PhysRevB.81.041402) (2010).
- 26 Nandkishore, R. & Levitov, L. Quantum anomalous Hall state in bilayer graphene. *Phys. Rev. B* **82**, 115124, doi:[10.1103/PhysRevB.82.115124](https://doi.org/10.1103/PhysRevB.82.115124) (2010).
- 27 Nandkishore, R. & Levitov, L. Polar Kerr Effect and Time Reversal Symmetry Breaking in Bilayer Graphene. *Phys. Rev. Lett.* **107**, 097402 (2011).
- 28 Velasco, J. *et al.* Transport spectroscopy of symmetry-broken insulating states in bilayer graphene. *Nature Nanotechnol.* **7**, 156 (2012).
- 29 Maher, P. *et al.* Evidence for a spin phase transition at charge neutrality in bilayer graphene. *Nat. Phys.* **9**, 154-158 (2013).
- 30 Kharitonov, M. Canted antiferromagnetic phase of the $\nu=0$ quantum Hall state in bilayer graphene. *Phys. Rev. Lett.* **109**, 046803 (2012).
- 31 Checkelsky, J. G., Li, L. & Ong, N. P. Zero-energy state in graphene in a high magnetic field. *Phys. Rev. Lett.* **100**, 206801, doi:[10.1103/PhysRevLett.100.206801](https://doi.org/10.1103/PhysRevLett.100.206801) (2008).
- 32 Bolotin, K. I. *et al.* Ultrahigh electron mobility in suspended graphene. *Sol. State Commun.* **146**, 351-355 (2008).
- 33 Du, X., Skachko, I., Barker, A. & Andrei, E. Y. Approaching ballistic transport in suspended graphene. *Nat. Nanotechnol.* **3**, 491-495 (2008).
- 34 Dean, C. R. *et al.* Boron nitride substrates for high-quality graphene electronics. *Nat Nano* **5**, 722-726 (2010).
- 35 Lui, C. H. *et al.* Imaging stacking order in few-layer graphene. *Nano Lett.* **11**, 164-169 (2011).
- 36 Ferrari, A. C. *et al.* Raman spectrum of graphene and graphene layers. *Phys. Rev. Lett.* **97**, 187401 (2006).
- 37 Liu, G., Velasco, J., Bao, W. Z. & Lau, C. N. Fabrication of graphene p-n-p junctions with contactless top gates. *Appl. Phys. Lett.* **92**, 203103 (2008).
- 38 Velasco, J., Liu, G., Bao, W. Z. & Lau, C. N. Electrical transport in high-quality graphene pnp junctions. *New J. Phys.* **11**, 095008, doi:[09500810.1088/1367-2630/11/9/095008](https://doi.org/10.1088/1367-2630/11/9/095008) (2009).

- 39 Cote, R., Rondeau, M., Gagnon, A.-M. & Barlas, Y. Phase diagram of insulating crystal and quantum Hall states in ABC-stacked trilayer graphene. *Phys. Rev. B* **86**, 125422, doi:[10.1103/PhysRevB.86.125422](https://doi.org/10.1103/PhysRevB.86.125422) (2012).
- 40 Barlas, Y., Cote, R. & Rondeau, M. Quantum Hall to Charge-Density-Wave Phase Transitions in ABC-Trilayer Graphene. *Phys. Rev. Lett.* **109**, 126804, doi:[10.1103/PhysRevLett.109.126804](https://doi.org/10.1103/PhysRevLett.109.126804) (2012).
- 41 Elferen, H. J. v. *et al.* Fine structure of the lowest Landau level in suspended trilayer graphene. *Phys. Rev. B* **88**, 121302 (R) (2013).
- 42 Bao, W. Z. *et al.* Magnetoconductance oscillations and evidence for fractional quantum Hall states in suspended bilayer and trilayer graphene. *Phys. Rev. Lett.* **105**, 246601, doi:[10.1103/PhysRevLett.105.246601](https://doi.org/10.1103/PhysRevLett.105.246601) (2010).
- 43 Lee, Y. *et al.* Giant Interaction-Induced Gap and Electronic Phases in Rhombohedral Trilayer Graphene. *preprint*, arXiv:1402.6413 (2014).
- 44 Zhang, F., Tilahun, D. & MacDonald, A. H. Hund's rules for the N=0 Landau levels of trilayer graphene. *Phys. Rev. B* **85**, 165139, doi:[10.1103/PhysRevB.85.165139](https://doi.org/10.1103/PhysRevB.85.165139) (2012).
- 45 Zhang, X., Faulhaber, D. & Jiang, H. Multiple Phases with the Same Quantized Hall Conductance in a Two-Subband System. *Phys. Rev. Lett.* **95**, 216801, doi:[10.1103/PhysRevLett.95.216801](https://doi.org/10.1103/PhysRevLett.95.216801) (2005).
- 46 Sanchez-Yamagishi, J. D. *et al.* Quantum Hall Effect, Screening, and Layer-Polarized Insulating States in Twisted Bilayer Graphene. *Phys. Rev. Lett.* **108**, 076601, doi:[10.1103/PhysRevLett.108.076601](https://doi.org/10.1103/PhysRevLett.108.076601) (2012).
- 47 Lee, K. *et al.* Chemical potential and quantum Hall ferromagnetism in bilayer graphene mapped using double bilayer heterostructures. *preprint*, arXiv:1401.0659 (2014).
- 48 Zhang, F., Sahu, B., Min, H. K. & MacDonald, A. H. Band structure of ABC-stacked graphene trilayers. *Phys. Rev. B* **82**, 035409, doi:[10.1103/PhysRevB.82.035409](https://doi.org/10.1103/PhysRevB.82.035409) (2010).

Chapter 8 : Spectroscopy measurement of Landau Level Gaps in Bilayer and Trilayer Graphene

Quantum Hall effect, in which a two-dimensional samples's Hall conductivities become quantized in multiple of conductance quantum, normally only appears in strong magnetic field. However, it may also appear spontaneously at zero magnetic field in samples with strong electronic interaction. An example is charge-neutral bilayer and ABC trilayer graphene that is unstable to a variety of gapped spontaneous quantum Hall states. Spontaneous Hall states can be explored by taking advantage of their adiabatic connection to QH states at integer filling factors within bilayer graphene's eightfold degenerate $N=0$ Landau levels (LLs). Our prior work¹ has shown that the LL gaps in dual-gated devices with controlled layer polarization are different from those in singly-gated devices. In this chapter, we discuss transport spectroscopy¹⁻³ to study high-quality dual-gated suspended BLG devices at $\nu=\pm 2$ ³⁻¹¹ as a function of magnetic field (B) and out-of-plane electric field (E_z). Chapter 8.1 introduces several gapped spontaneous quantum Hall (QH) state due to chiral-symmetry breaking. Chapter 8.2 presents two distinct $\nu=\pm 2$ QH states: (1). Phase I is fully resolved only near $E_z=0$ and large B , and has a relatively small gap that extrapolates to 0 at $B=0$. This phase is expected⁸ to be spontaneously spin-polarized and to have coherence between valleys (layers), *i.e.* with Kekulé valley order¹²⁻¹⁴. (2). Phase II appears only at finite E_z , but can be stabilized at a much smaller B and has a much larger gap with a finite $B=0$ intercept, suggesting that this state survives to anomalously weak B . Chapter 8.3 describes the technique of

transport spectroscopy as a spectroscopic tool to measure Landau level gap.. Chapter 8.4 discusses the nature of two distinct $\nu=\pm 2$ QH states. Chapter 8.5 briefly discusses the spectroscopy of ABC-stacked trilayer graphene.

8.1 Spontaneous quantum Hall states

Because of its large density-of-states and the 2π Berry phase near its low-energy band-contact points¹⁵⁻²⁰, neutral bilayer graphene (BLG) at zero magnetic field is susceptible to chiral-symmetry breaking, leading to several gapped spontaneous quantum Hall (QH) states distinguished by valley and spin-dependent quantized Hall conductivities²¹⁻⁴⁸. In these states, each spin-valley flavor spontaneously transfers charge between layers^{10,11}. When spin is ignored only two classes of gapped states can be distinguished: (i) ones in which electrons in opposite valleys are polarized to opposite layers, producing a quantum anomalous Hall (QAH) state with broken time-reversal symmetry and orbital magnetization²¹⁻²³, and (ii) states in which electrons in opposite valleys are polarized to the same layer, yielding a quantum valley Hall (QVH) state with broken inversion symmetry and Hall conductivity $\sigma_H=0$ ⁷⁻⁹. For spinful electrons, symmetry-broken states further include the layer antiferromagnetic state (LAF) and the quantum spin Hall state with two-terminal conductivity 0 and $4e^2/h$, respectively. An additional competing state is the Kekulé order with spontaneous coherence between valleys. Electronic configurations of these states are summarized in Table 8.1. (Here T and B indicate the top and bottom layers, respectively).

So far only the LAF state, which has QVH states with opposite layer polarization signs for opposite spins^{9,10,26,27,34,35,37,38,28,29} and appear to be the thermodynamic ground state^{2,3,49}, and (at finite interlayer electric field E_{\perp}) the layer polarized state, which has QVH states with spin-independent layer polarization, have been observed experimentally.^{2,3,6,49} Other spontaneous QH states, and competing states with Kekulé order, have eluded experimental observation (though prior work on singly-gated devices has shown that the $\nu=4$ and $\nu=0$ QH states can persist to very small B ⁸). The experiments we describe are motivated by the sensitivity of the competing orders in BLG to both E_{\perp} and B fields.

Table 8.1: Schematic diagram of electronic configurations of the states stabilized by electric field and magnetic field.

	K \uparrow	K \downarrow	K' \uparrow	K' \downarrow	G (e^2/h)	Layer polarization
Quantum Anomalous Hall (QAH)	T	T	B	B	4	No
Layer Antiferromagnet (LAF)	T	B	T	B	0	No
Quantum Spin Hall	T	B	B	T	4	No
Quantum Valley Hall (QVH)	T	T	T	T	0	Yes
$\nu=2$ QH state	T	T	B	T	2	Yes
Kekulé order (at finite B)	T	T&B	B	T&B	2	No

T and B indicate the top and bottom layers, respectively.

8.2 Realization of two distinct $\nu=\pm 2$ QH states.

Suspended dual-gated devices in figure 8.2 with mobilities as high as $150,000 \text{ cm}^2\text{V}^{-1}\text{s}^{-1}$ were measured in He^3 refrigerators. Here we present data from two different devices (device 1 and 2) with field effect mobilities $80,000$ and $40,000 \text{ cm}^2\text{V}^{-1}\text{s}^{-1}$, respectively. (Similar data are observed in two additional devices). All measurements were taken at temperature $T=260\text{mK}$.

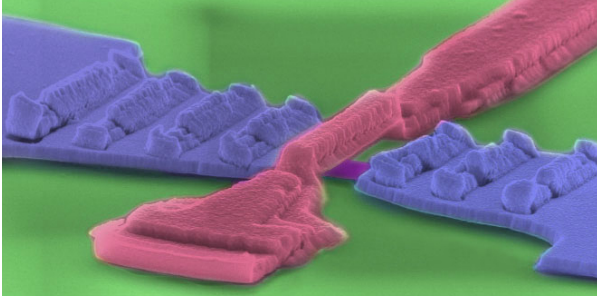


Figure 8.1: SEM image of a dual-gated device

Figure 8.2a plots the 2-terminal differential conductance G of device 1 in units of e^2/h at $B=3.5\text{T}$ as a function of charge density n and out-of-plane electric field E_z . The QH plateaus at $\nu=0, \pm 1, \pm 2$ and ± 4 appear as blue, green, yellow, and brown color bands, respectively. Most interestingly, the resolution of $\nu=\pm 2$ QH states depends on E_z . This can be seen in the $G(\nu)$ traces in figure 8.2b: near $E_z=0$, only the QH plateaus at $\nu=0$ and ± 4 are fully resolved; in contrast, at larger $E_z=-21 \text{ mV nm}^{-1}$, the $\nu=\pm 2$ plateaus are clearly visible. The resolution of the $\nu=\pm 2$ states is abrupt: at $\nu=2$, $G(E_z)$ stays at $4e^2/h$ for small E_z , but drops sharply to a $2e^2/h$ plateau at a well-defined critical value $E_{z,c}$. This critical $E_{z,c}$

is $\sim 10 \text{ mV nm}^{-1}$ at 8T, and is only weakly dependent on B , with a slope $\sim 0.72 \text{ mV nm}^{-1}\text{T}^{-1}$ as shown in figure 8.2c.

The above observations reflect unprecedented sample quality, but agree with previous studies in which the $\nu=2$ state is fully resolved only in when E_{\perp} is non-zero either in a controlled fashion in dual-gated devices^{3,6} or inadvertently in singly-gated devices^{2,7,10,49}. This suggests that the $\nu=2$ state observed at $B=3.5\text{T}$ is layer polarized. The intriguing possibility of a $\nu=2$ state at $E_{\perp}=0$ in higher quality samples or in stronger fields has not been demonstrated previously. Figure 8.2d displays $G(\nu)$ for device 2. As in the case of Device 1, for B less than 20T the $\nu=2$ state is resolved only in the presence of finite E_{\perp} . At $E_{\perp}=0$, the state is fully resolved for $B>24\text{T}$.

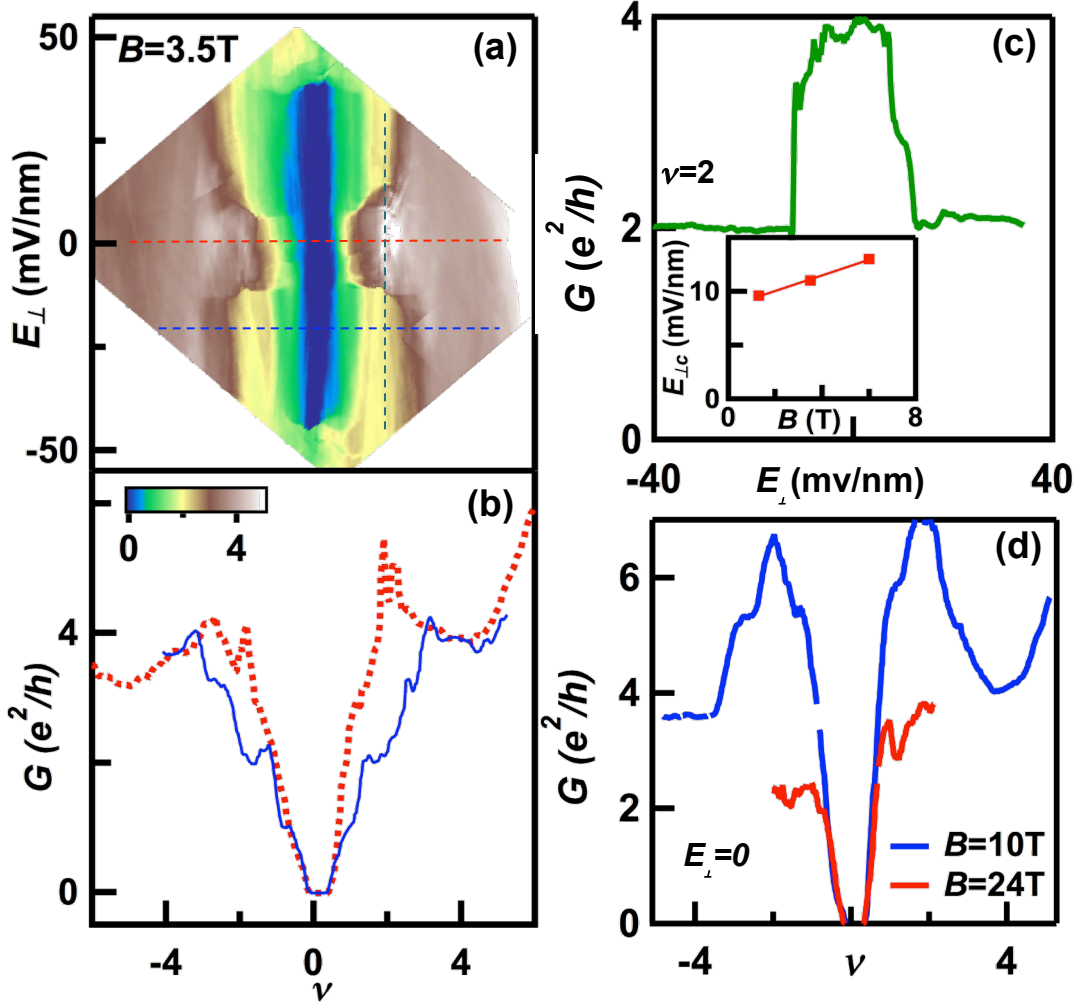


Figure 8.2: Magnetotransport data (a) $G(E_{\perp}, n)$ of Device 1 at $B=3.5\text{T}$. (b) Line traces $G(n)$ at $B=3.5\text{T}$ and $E_{\perp}=0$ (red dotted line) and $E_{\perp}=-21\text{ mV/nm}$ (blue solid line), respectively. (c) Line trace $G(E_{\perp})$ at $B=3.5\text{T}$ and filling factor $\nu=2$ (density $n=1.7\times 10^{10}\text{ cm}^{-2}$). Inset: Critical electric field $E_{\perp,c}$ vs. B and linear fit to the data points with slope $\sim 0.72\text{ mV/nm/T}$. (d) $G(n)$ of device 2 at $E_{\perp}=0$ and $B=10\text{T}$ and 24T , respectively.

8.3 Transport spectroscopy technique

As described above, two distinct QH states at $\nu=2$ are observed experimentally:

Phase I is only fully resolved at $E_{\perp}=0$ and large B , and phase II is resolved at large E_{\perp} and

relatively small B . To further explore these two distinct $\nu=2$ QH states, we perform transport spectroscopy by using the source-drain bias V as a spectroscopic tool^{1,2}.

When the zero-bias conductance is at the center of the QH plateau, BLG's Fermi level is pinned between the highest filled and the next unfilled LLs as shown in figure 8.3a. Charges are carried by edge states, which are separated from the gapped bulk by a gap on the order of the LL gap. Hence electrons are injected into the edge states and can tunnel into the bulk, yielding features that resemble tunneling spectroscopy. Increasing bias raises the source's Fermi level, which eventually aligns with the next unfilled LL in figure 8.3b and allows additional charge transport through the bulk, thereby leading to increased conductance. As a result, the device displays a conductance valley at $V = 0$. Conversely, when G is between the plateaus, the electrodes' Fermi level is aligned with the highest filled LL as shown in figure 8.3c, thus allowing transport through the extended states in the bulk. Increasing bias detunes from the LL and disallows bulk transport at the Fermi level of the source contact, yielding lower conductance at large V , and thus an overall conductance peak at $V = 0$. This model assumes nonequilibrium of charges between the edge states and the bulk, which is reasonable considering the small dimension of the samples ($\sim 1-1.4 \mu\text{m}$). We also note that a crucial component of the model is the high device quality. Indeed, for devices with lower mobility, the diamond features are smeared or absent altogether.

Based on this simple model, we can spectroscopically resolve LL gaps by examining the $G(V)$ curves at the center of a QH plateau. The conductance at $V=0$ yields

the edge state contribution, whereas the full width of the conductance valley yields $2D$, where D is the gap between the filled and unfilled LLs.

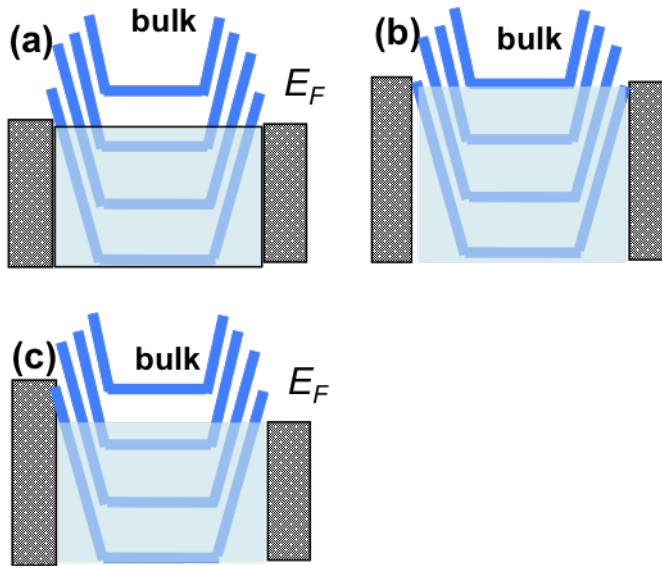


Figure 8.3: Model of transport across the device in the quantum Hall regime (a) At $V=0$, Fermi levels of the source (S) and drain (D) electrodes are located between the highest occupied Landau level and an unoccupied level. The bulk is gapped and transport occurs via edge states. (b) Similar to (a), except that a bias V is applied between S and D. (c) At $V=0$, Fermi levels of the electrodes are aligned with the occupied Landau level. Transport occurs via the bulk.

8.3 Characterization of the two distinct $\nu=\pm 2$ QH states.

Figure 8.4a-b display $G(V, \nu)$ from Device 1 at $B=3.5\text{T}$ and $E_L=0$ and -14.4 mV/nm, respectively. At $E_L=-14.4$ mV nm⁻¹, the diamond at $\nu=-2$ is significantly larger than that at $E_L=0$, demonstrating an enlarged LL gap. Such difference in gap sizes can be seen more clearly in line traces in figure 8.4c, which are taken from figure 8.4a and figure 8.4b at $\nu=-2$, respectively. Similar traces at $B=6\text{T}$ are shown in figure 8.4d. At $E_L=-14\text{mV}$

nm^{-1} , prominent zero-bias valleys appear in $G(V)$ traces as shown in figure 8.4c-d, red lines), indicating that the $\nu=-2$ state (phase II) is fully resolved. In contrast, at $E_{\perp}=0$, the $G(V)$ traces display only small conductance dips superimposed on a peak at zero bias as shown in figure 8.4c-d, blue traces, suggesting that phase I is only partially resolved.

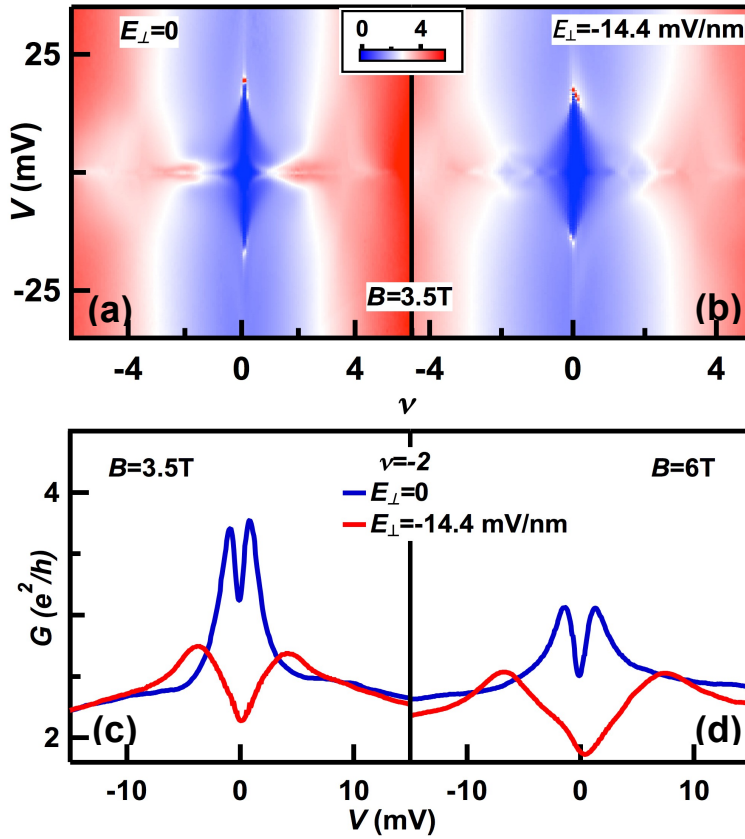


Figure 8.4: Transport spectroscopy data from Device 1. (a-b) $G(V, n)$ at $E_{\perp}=0$ and -14.4 mV/nm, respectively. Both data are taken at $B=3.5$ T. (c) Line trace $G(V)$ at $\nu=-2$ and $B=3.5$ T. Blue and red traces are taken at $E_{\perp}=0$ and -14.4 mV/nm, respectively. (d) Similar data taken at $B=6$ T.

The measured values of $\Delta_{\nu=-2}$ are shown in figure 8.5a. At $E_{\perp}=0$, the LL gap for phase I is $\Delta_I \sim 0.17$ meV T^{-1} with a zero intercept at $B=0$; in contrast, at $E_{\perp}=-14.4$ mV nm^{-1}

¹, the gap for phase II is larger by more than a factor of 5, $\Delta_{II} \sim 1.0 \text{ meV T}^{-1}$, with a non-vanishing $B=0$ intercept.

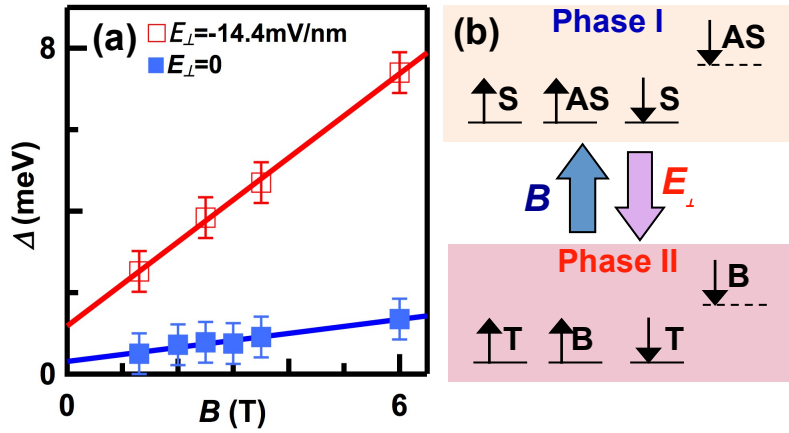


Figure 8.5: Transport spectroscopy data from Device 1 (a) Measured LL gap $\Delta(B)$ at $\nu=2$ and $E_{\perp}=0$ and -14.4 mV/nm , respectively. (b) Schematics of transitions between Phase I and Phase II at $\nu=2$. (T: top layer; B: bottom layer; S: symmetric state $|S\rangle=|T\rangle+|B\rangle$; $|AS\rangle$:antisymmetric state $|T\rangle-|B\rangle$)

8.4 Discussion of nature of two $\nu=2$ QH states

We now discuss the nature of these two distinct $\nu=2$ QH states. Phase I is only fully resolved at $E_{\perp}=0$ and large B , with a vanishing LL gap at $B=0$. The fact that a large B is required to stabilize this phase has been anticipated in BLG QH ferromagnetism theory^{19,22,36}. In the absence of interactions, the zero-energy LLs are 8-fold degenerate and QH effects only exhibit at $\nu=\pm 4$; thus interactions are necessary to induce phase I. Since the valley K and K' states in the $N=0$ subspace are localized at the top and bottom layers, respectively, the valley pseudospin and layer pseudospin coincide. At $E_{\perp}=0$, there

is an electrostatic energy cost of valley (or equivalently layer) polarization, and it is energetically favorable to achieve a gap at $\nu=2$ by establishing coherence between the valleys/layers. This is what is observed experimentally: as phase I is only observed in the absence of E_z , it is evidently not layer polarized but a symmetric linear combination of the top and bottom layers. Such a state is also a valley symmetric state, i.e., a valley-Kekulé order in the presence of B due to electron-electron interactions. This Kekulé order appears at large B , even though it is absent at $B=0$. Accordingly, our experiments demonstrate that the stability of the Kekulé state, as measured by its gaps, disappears as B goes to zero.

The valley-Kekulé order that we have observed is reminiscent of the Kekulé lattice distortion proposed for carbon nanotubes and graphene¹²⁻¹⁴, albeit here it only exists in the presence of a magnetic field. As B approaches 0, a spontaneous quantum Hall state⁸ emerges as the ground state, as observed previously³. In the absence of B fields, the inter-valley interactions in BLG are too weak to induce any valley coherence. At finite B , however, due to the equivalency of the layer and valley pseudospins, any interlayer coherence naturally leads to inter-valley coherence.

In contrast to Phase I, Phase II is observed at anomalously small B and large E_z , with a LL gap that extrapolates to a finite $B=0$ intercept. Its appearance at much smaller B than Phase I is reminiscent of the spontaneous QH states at $B=0$ ^{8,9}. This phase is adiabatically connected to the $B=0$ collinear ferromagnet ordered state with a majority spin QAH state and a minority spin QVH state^{20,22,36}. Indeed phase II is only metastable^{20,22} at $B=0$, most likely because it loses the ordering competition to the LAF

state at $E_{\perp}=0$ and to the QVH state at $E_{\perp}\neq 0$. As observed here, however, phase II can be preferred in the presence of finite B and E_{\perp} , since states with different total Hall conductivity are most stable at different carrier densities; moreover, this phase's energy is lowered by the orbital and spin coupling to B , and by the compensation of the Hartree energy cost of its layer polarization by E_{\perp} . It is partially polarized in spin, valley and layer, and is consistent with a quantum Hall ferromagnet state^{7,19,22,36}.

In terms of their layer characteristics, phase I has XY valley (layer) coherence order whereas phase II has layer-polarization Ising order. Schematic representations of these two phases are provided in figure 8.5b. Here S and AS indicate symmetry and anti-symmetric combination of the K and K' valleys, respectively. The energy differences between these two phases arise mainly from (i) the Hartree energy of layer polarization and (ii) the difference between interlayer and intralayer exchange for the occupied $N=0$ LLs. Both differences scale as $(d/l_b)*(e^2/l_b) \sim B$, in agreement with the weak linear B dependence of $E_{\perp c}$ in our BLG measurements, where the layer separation d is much smaller than the magnetic length l_b .

We also note that data from singly-gated devices are similar to those at finite E_{\perp} : due to the presence of an inadvertently induced electric field $ne/2\epsilon_0$ (here ϵ_0 is the permittivity of vacuum), the $\nu=\pm 2$ states in singly-gated devices are almost always in phase II and stabilized by E_{\perp} . Thus, Phase I has not been observed before and Phase II was observed accidentally.

Lastly, using transport spectroscopy, we explore the dependence of the LL gap on E_z . Figure 8.6a plots $G(V, E_z)$ at $\nu=2$ from Device 2. The most striking feature is the red region at the center of the plot, i.e. at small E_z , where $G \sim 4e^2/h$, surrounded by blue-white regions where $G \sim 2e^2/h$. The abrupt transition between the 2 regions as shown in figure 8.6b is the same as that observed in figure 8.2c. At $E_z=0$, $G(V)$ displays a narrow conductance dip at $V=0$, with half-width ~ 1.6 mV, corresponding to Δ_I as shown in figure 8.6c. At large $E_z = -35$ mV nm⁻¹, the $G(V)$ trace is significantly different, with much wider conductance valley and half-width of 15 meV. We thus take the half-width of wider valley to be Δ_{II} . The dependence of Δ_{II} on E_z is shown in figure 8.6d. It increases with E_z of both polarities, though with slight asymmetry. Interestingly, the wider conductance valley, which appears as the white curves superimposed on top of the blue background, extend into $|E_z| < E_{z,c}$, i.e. the narrow dip co-exists with wider valley, suggesting co-existence of both states near $E_{z,c}$.

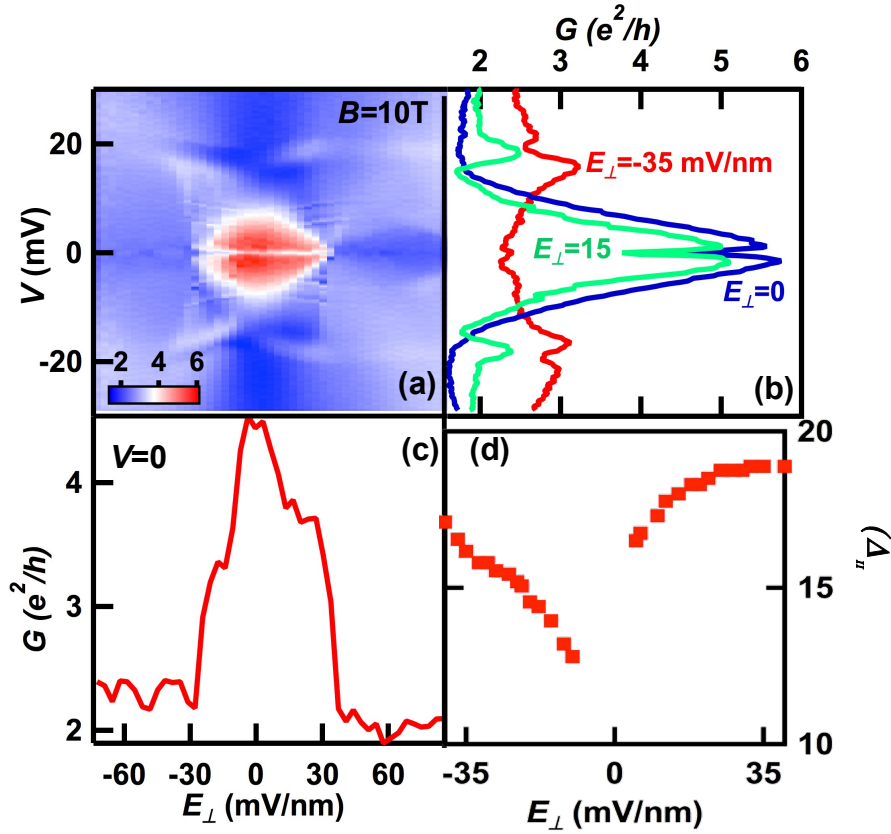


Figure 8.6: Spectroscopy data from Device 2 at $B=10T$ and $\nu=2$. (a) $G(V, E_{\perp})$ data. (b) Line traces $G(V)$ at $E_{\perp} = 0$ (blue), 15 (green) and -35 mV/nm (red). (c) $G(E_{\perp})$ at $V=0$. (d). Gap of layer polarized $\nu=2$ state vs. E_{\perp} .

8.5 Spectroscopy measurement of ABC trilayer graphene

We perform the spectroscopy measurement in ABC-stacked trilayer graphene. As discussed in chapter 7, the hexagon features appear due to multiple Landau Level crossings, combined with LL broadening that smears the crossing point. Thus, G is quantized everywhere at the standard value $\nu e^2/h$, *except* at each crossing point. For instance, at $\nu=-2$ state, quantization is lost at $U_{\perp c} \sim \pm 18$ mV (red curve) in figure 8.7b due to LL crossing. Figure 8.7c plots $G(V, U_{\perp})$ at $\nu = -2$ and $B=5T$; the LL gap is

approximately outlined by the region with white color. At $U_{\perp} = 0$ and $U_{\perp c} = \pm 18$ mV, LL gaps are 1.9 meV and 0.2 meV at $\nu = -2$, respectively. Considering LL level crossing model, the 1.9 meV gap corresponds to the maximum energy gap between adjacent two levels from top-layer and bottom-layer before crossing, whereas the 0.2 meV gap is measured at the LL level crossing point. Preliminary data at different magnetic field values and filling factors are summarized in Table 8.2. More detail study is required to understand the effect of the screening effect and LL broadening in this system.

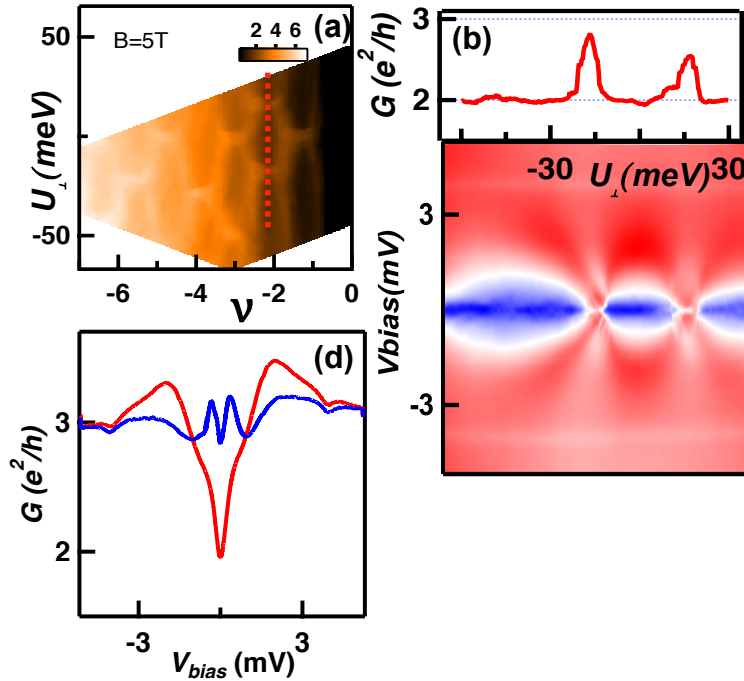


Figure 8.7: Transport and spectroscopy data at $B=5\text{T}$ and $\nu=2$. (a) $G(\nu, U_{\perp})$ data. (b) Line traces $G(U_{\perp})$ at $\nu = -2$ (red) and (c) $G(V, U_{\perp})$ at $\nu = -2$. (d) Line traces $G(V)$ at $U_{\perp} = 0$ (red) and -18mV .

Table 8.2: LL energy gap at different magnetic field and QH filling factor

B(T)	$\Delta_{\nu=2}(\text{meV})$		$\Delta_{\nu=3}(\text{meV})$		$\Delta_{\nu=4}(\text{meV})$	
	Max	Min	Max	Min	Max	Min
	4	1	1	1	1	-
5	1.9	0.25	-	-	1.75	0.46
6	2.5	0.38	2.3	0.3	2.08	0.19
7	3	0.5	2.4	0.24	2.67	0.24
8	3.8	0.47	-	-	-	-

The minimum energy gap is measured at the LL level crossing point.

8.6 Conclusion

In conclusion, we utilized high quality dual gated suspended BLG devices to explore the spontaneous symmetry breaking physics near charge neutrality. We resolved two distinct $\nu=2$ QH states: phase I is fully resolved only at $E_{\perp}=0$ and large B , and is likely a Kekulé state with inter-layer and inter-valley coherence; phase II is observed at small B and large E_{\perp} . Our measurements demonstrate that it is metastable at $B=0$. Our data represent the first spectroscopic mapping of the exotic competing orders at $\nu=\pm 2$ in BLG, and pave the way for studies of other symmetry-broken states at different filling factors in BLG or in the much less explored TLG^{22,50}. Our study also motivates future in-plane B measurements^{23,51,52} to realize more complete control of spin, layer, and orbital degrees of freedom.

Reference

- 1 Velasco Jr., J. *et al.* Transport Measurement of Landau level Gaps in Bilayer Graphene with Layer Polarization Control. *Nano Lett.* **14**, 1324-1328 (2014).
- 2 Freitag, F., Trbovic, J., Weiss, M. & Schonenberger, C. Spontaneously gapped ground state in suspended bilayer graphene. *Phys. Rev. Lett.* **108**, 076602 (2012).
- 3 Velasco, J. *et al.* Transport spectroscopy of symmetry-broken insulating states in bilayer graphene. *Nature Nanotechnol.* **7**, 156-160 (2012).
- 4 Feldman, B. E., Martin, J. & Yacoby, A. Broken-symmetry states and divergent resistance in suspended bilayer graphene. *Nat. Phys.* **5**, 889-893, doi:[10.1038/nphys1406](https://doi.org/10.1038/nphys1406) (2009).
- 5 Zhao, Y., Cadden-Zimansky, P., Jiang, Z. & Kim, P. Symmetry Breaking in the Zero-Energy Landau Level in Bilayer Graphene. *Phys. Rev. Lett.* **104**, 066801, doi:[10.1103/PhysRevLett.104.066801](https://doi.org/10.1103/PhysRevLett.104.066801) (2010).
- 6 Weitz, R. T., Allen, M. T., Feldman, B. E., Martin, J. & Yacoby, A. Broken-symmetry states in doubly gated suspended bilayer graphene. *Science* **330**, 812-816, doi:[10.1126/science.1194988](https://doi.org/10.1126/science.1194988) (2010).
- 7 van Elferen, H. J. *et al.* Field-induced quantum Hall ferromagnetism in suspended bilayer graphene. *Phys. Rev. B* **85**, 115408, doi:[11540810.1103/PhysRevB.85.115408](https://doi.org/10.1103/PhysRevB.85.115408) (2012).
- 8 Martin, J., Feldman, B. E., Weitz, R. T., Allen, M. T. & Yacoby, A. Local Compressibility Measurements of Correlated States in Suspended Bilayer Graphene. *Phys. Rev. Lett.* **105**, 256806, doi:[10.1103/PhysRevLett.105.256806](https://doi.org/10.1103/PhysRevLett.105.256806) (2010).
- 9 Bao, W. Z. *et al.* Magnetoconductance oscillations and evidence for fractional quantum Hall states in suspended bilayer and trilayer graphene. *Phys. Rev. Lett.* **105**, 246601, doi:[10.1103/PhysRevLett.105.246601](https://doi.org/10.1103/PhysRevLett.105.246601) (2010).
- 10 Jiang, Z., Zhang, Y., Stormer, H. L. & Kim, P. Quantum Hall states near the charge-neutral Dirac point in graphene. *Phys Rev Lett* **99**, 106802 (2007).
- 11 Lee, K. *et al.* Chemical potential and quantum Hall ferromagnetism in bilayer graphene mapped using double bilayer heterostructures. *preprint*, arXiv:1401.0659 (2014).
- 12 Chamon, C. Solitons in carbon nanotubes. *Phys. Rev. B* **62**, 2806-2812 (2000).

- 13 Hou, C.-Y., Chamon, C. & Mudry, C. Electron Fractionalization in Two-Dimensional Graphenelike Structures. *Phys. Rev. Lett.* **98**, 186809 (2007).
- 14 Jackiw, R. & Pi, S. Y. Chiral Gauge Theory for Graphene. *Phys. Rev. Lett.* **98**, 266402 (2007).
- 15 Novoselov, K. S. *et al.* Unconventional quantum Hall effect and Berry's phase of 2π in bilayer graphene. *Nat. Phys.* **2**, 177-180 (2006).
- 16 McCann, E. & Fal'ko, V. I. Landau-level degeneracy and quantum hall effect in a graphite bilayer. *Phys. Rev. Lett.* **96**, 086805, doi:[10.1103/PhysRevLett.96.086805](https://doi.org/10.1103/PhysRevLett.96.086805) (2006).
- 17 Castro Neto, A. H., Guinea, F., Peres, N. M. R., Novoselov, K. S. & Geim, A. K. The electronic properties of graphene. *Rev. Mod. Phys.* **81**, 109-162, doi:[10.1103/RevModPhys.81.109](https://doi.org/10.1103/RevModPhys.81.109) (2009).
- 18 Guinea, F., Castro Neto, A. H. & Peres, N. M. R. Electronic states and Landau levels in graphene stacks. *Phys. Rev. B* **73**, 245426 (2006).
- 19 Barlas, Y., Cote, R., Nomura, K. & MacDonald, A. H. Intra-Landau-level cyclotron resonance in bilayer graphene. *Phys. Rev. Lett.* **101**, 097601, doi:[10.1103/PhysRevLett.101.097601](https://doi.org/10.1103/PhysRevLett.101.097601) (2008).
- 20 Min, H., Borghi, G., Polini, M. & MacDonald, A. H. Pseudospin magnetism in graphene. *Phys. Rev. B* **77**, 041407, doi:[10.1103/PhysRevB.77.041407](https://doi.org/10.1103/PhysRevB.77.041407) (2008).
- 21 Nandkishore, R. & Levitov, L. Quantum anomalous Hall state in bilayer graphene. *Phys. Rev. B* **82**, 115124, doi:[10.1103/PhysRevB.82.115124](https://doi.org/10.1103/PhysRevB.82.115124) (2010).
- 22 Zhang, F., Jung, J., Fiete, G. A., Niu, Q. A. & MacDonald, A. H. Spontaneous quantum Hall states in chirally stacked few-layer graphene systems. *Phys. Rev. Lett.* **106**, 156801, doi:[10.1103/PhysRevLett.106.156801](https://doi.org/10.1103/PhysRevLett.106.156801) (2011).
- 23 Zhang, F. & MacDonald, A. H. Distinguishing Spontaneous Quantum Hall States in Graphene Bilayers. *Phys. Rev. Lett.* **108**, 186804 (2012).
- 24 Zhang, F., Min, H. & MacDonald, A. H. Competing ordered states in bilayer graphene. *Phys. Rev. B* **86**, 155128 (2012).
- 25 Zhang, F., Min, H., Polini, M. & MacDonald, A. H. Spontaneous inversion symmetry breaking in graphene bilayers. *Phys. Rev. B* **81**, 041402 (R), doi:[10.1103/PhysRevB.81.041402](https://doi.org/10.1103/PhysRevB.81.041402) (2010).

- 26 Kharitonov, M. Canted antiferromagnetic phase of the $\nu=0$ quantum Hall state in bilayer graphene. *Phys. Rev. Lett.* **109**, 046803 (2012).
- 27 Kharitonov, M. Antiferromagnetic state in bilayer graphene. *Phys. Rev. B* **86**, 195435 (2012).
- 28 Mayorov, A. S. *et al.* Interaction-driven spectrum reconstruction in bilayer graphene. *Science* **333**, 860-863, doi:[10.1126/science.1208683](https://doi.org/10.1126/science.1208683) (2011).
- 29 Lemonik, Y., Aleiner, I. & Fal'ko, V. I. Competing nematic, antiferromagnetic, and spin-flux orders in the ground state of bilayer graphene. *Phys. Rev. B* **85**, 245451, doi:[10.1103/PhysRevB.85.245451](https://doi.org/10.1103/PhysRevB.85.245451) (2012).
- 30 Lemonik, Y., Aleiner, I. L., Toke, C. & Fal'ko, V. I. Spontaneous symmetry breaking and Lifshitz transition in bilayer graphene. *Phys. Rev. B* **82**, 201408, doi:[10.1103/PhysRevB.82.201408](https://doi.org/10.1103/PhysRevB.82.201408) (2010).
- 31 Li, J. A., Martin, I., Buttiker, M. & Morpurgo, A. F. Topological origin of subgap conductance in insulating bilayer graphene. *Nat. Phys.* **7**, 38-42, doi:[10.1038/nphys1822](https://doi.org/10.1038/nphys1822) (2011).
- 32 Vafek, O. Interacting fermions on the honeycomb bilayer: From weak to strong coupling. *Phys. Rev. B* **82**, 205106 (2010).
- 33 Vafek, O. & Yang, K. Many-body instability of Coulomb interacting bilayer graphene: Renormalization group approach. *Phys. Rev. B* **81**, 041401, doi:[10.1103/PhysRevB.81.041401](https://doi.org/10.1103/PhysRevB.81.041401) (2010).
- 34 Cvetkovic, V., Throckmorton, R. E. & Vafek, O. Electronic multicriticality in bilayer graphene. *Phys. Rev. B* **86**, 075467, doi:[10.1103/PhysRevB.86.075467](https://doi.org/10.1103/PhysRevB.86.075467) (2012).
- 35 Throckmorton, R. E. & Vafek, O. Fermions on bilayer graphene: Symmetry breaking for $B=0$ and $\nu=0$. *Phys. Rev. B* **86**, 115447, doi:[10.1103/PhysRevB.86.115447](https://doi.org/10.1103/PhysRevB.86.115447) (2012).
- 36 Jung, J., Zhang, F. & MacDonald, A. H. Lattice theory of pseudospin ferromagnetism in bilayer graphene: Competing interaction-induced quantum Hall states. *Phys. Rev. B* **83**, 115408, doi:[10.1103/PhysRevB.83.115408](https://doi.org/10.1103/PhysRevB.83.115408) (2011).
- 37 Lang, T. C. *et al.* Antiferromagnetism in the Hubbard Model on the Bernal-Stacked Honeycomb Bilayer. *Phys. Rev. Lett.* **109**, 126402, doi:[10.1103/PhysRevLett.109.126402](https://doi.org/10.1103/PhysRevLett.109.126402) (2012).

- 38 Scherer, M. M., Uebelacker, S. & Honerkamp, C. Instabilities of interacting electrons on the honeycomb bilayer. *Phys. Rev. B* **85**, 235408, doi:[23540810.1103/PhysRevB.85.235408](https://doi.org/10.1103/PhysRevB.85.235408) (2012).
- 39 Zhu, L., Aji, V. & Varma, C. M. Ordered Loop Current States in Bilayer Graphene. *Phys. Rev. B* **87**, 035427 (2013).
- 40 Gorbar, E. V., Gusynin, V. P., Jia, J. & Miransky, V. A. Broken-symmetry states and phase diagram of the lowest Landau level in bilayer graphene. *Phys. Rev. B* **84**, 235449, doi:[23544910.1103/PhysRevB.84.235449](https://doi.org/10.1103/PhysRevB.84.235449) (2011).
- 41 Gorbar, E. V., Gusynin, V. P., Miransky, V. A. & Shovkovy, I. A. Coexistence and competition of nematic and gapped states in bilayer graphene. *Phys. Rev. B* **86**, 125439, doi:[12543910.1103/PhysRevB.86.125439](https://doi.org/10.1103/PhysRevB.86.125439) (2012).
- 42 Gorbar, E. V., Gusynin, V. P., Miransky, V. A. & Shovkovy, I. A. Broken symmetry $\nu=0$ quantum Hall states in bilayer graphene: Landau level mixing and dynamical screening. *Phys. Rev. B* **85**, 235460, doi:[23546010.1103/PhysRevB.85.235460](https://doi.org/10.1103/PhysRevB.85.235460) (2012).
- 43 Gorbar, E. V., Gusynin, V. P. & Miransky, V. A. Dynamics and phase diagram of the $\nu=0$ quantum Hall state in bilayer graphene. *Phys. Rev. B* **81**, 155451, doi:[10.1103/PhysRevB.81.155451](https://doi.org/10.1103/PhysRevB.81.155451) (2010).
- 44 Cote, R., Lambert, J., Barlas, Y. & MacDonald, A. H. Orbital order in bilayer graphene at filling factor $\nu = -1$. *Phys. Rev. B* **82**, 035445, doi:[10.1103/PhysRevB.82.035445](https://doi.org/10.1103/PhysRevB.82.035445) (2010).
- 45 Cote, R., Luo, W. C., Petrov, B., Barlas, Y. & MacDonald, A. H. Orbital and interlayer skyrmion crystals in bilayer graphene. *Phys. Rev. B* **82**, 245307, doi:[10.1103/PhysRevB.82.245307](https://doi.org/10.1103/PhysRevB.82.245307) (2010).
- 46 Shizuya, K. Pseudo-zero-mode Landau levels and collective excitations in bilayer graphene. *Phys. Rev. B* **79**, 165402 (165411 pp.), doi:[10.1103/PhysRevB.79.165402](https://doi.org/10.1103/PhysRevB.79.165402) (2009).
- 47 Kim, S., Lee, K. & Tutuc, E. Spin-Polarized to Valley-Polarized Transition in Graphene Bilayers at $\nu=0$ in High Magnetic Fields. *Phys. Rev. Lett.*, 016803 (2009).
- 48 Roy, B. Theory of integer quantum Hall effect in bilayer graphene near neutrality point. *preprint*, arXiv:1203.6340 (2012).

- 49 Veligura, A. *et al.* Transport gap in suspended bilayer graphene at zero magnetic field. *Phys. Rev. B* **85**, 155412 (2012).
- 50 Zhang, F., Tilahun, D. & MacDonald, A. H. Hund's rules for the N=0 Landau levels of trilayer graphene. *Phys. Rev. B* **85**, 165139, doi:[10.1103/PhysRevB.85.165139](https://doi.org/10.1103/PhysRevB.85.165139) (2012).
- 51 Maher, P. *et al.* Evidence for a spin phase transition at charge neutrality in bilayer graphene. *Nat. Phys.* **9**, 154-158 (2013).
- 52 Freitag, F., Weiss, M., Maurand, R., Trbovic, J. & Schönenberger, C. Spin symmetry of the bilayer graphene ground state. *Phys. Rev. B* **87**, 161402, doi:[10.1103/PhysRevB.87.161402](https://doi.org/10.1103/PhysRevB.87.161402) (2013).

Chapter 9 : Conclusion and Outlook

9.1:Conclusion

Over the past 5 years, I have explored the electrical properties of trilayer graphene (TLG) by performing low temperature transport measurements on high-quality dual-gated suspended devices. We find that the two different stacking orders in TLG lead to very different band structures, crystal symmetries and orders of symmetry breaking in the presence of magnetic field. ABA-stacked TLG consists of monolayer-like and bilayer-like branches, and the 12-fold degeneracy of the lowest Landau level is lifted by a combination of electric and magnetic fields. Transitions between different states at filling factor $\nu=0$ is observed. In ABC-stacked TLG, the symmetries from spin, valley and orbital are spontaneously broken at zero magnetic field due to the strong electronic interaction and adiabatically connected with broken-symmetry states in quantum Hall regime; evidence for Landau level crossing is observed. Finally, we also develop two different techniques to measure Landau level gaps – via transport spectroscopy by using source-drain bias as a spectroscopic tool, and via application of an interlayer potential that compensates the energy difference between Landau levels. These results provide insight into both single particle physics and many-body interaction in graphene and low-dimensional materials.

9.2: Outlook and Future Work

BLG and TLG graphene are fascinating 2D systems, and energy gaps can be created via either application of electric field or electronic interactions. Such gaps are promising for tunable electronics or optoelectronics devices. Even though the 2-3mV interaction-induced gap in BLG is too small for digital applications, it is important to note that the gap size increases by a factor of 10 in TLG. Generally, the collective state in rhombohedral-stacked graphene becomes dramatically more robust when each additional layer is added, due to the strongly enhanced density of states at very small charge density. Thus, we expect that the gap in tetra-layer or penta-layer graphene may be as large as one to a few hundred meV. In addition to the tunable gap and robustness at room temperature, such states are expected to be highly energy efficient due to the collective motion of many electrons, only a small voltage is needed to turn the state “on” and “off”.

For the future work, ABC-stacked TLG remains a fascinating venue for investigating Klein tunneling and the phase transition. Firstly, in the local top-gate geometry, we expect to observe Klein tunneling in high quality ABC TLG¹. Unlike the electrons in single layer graphene, which are Dirac fermions with Berry phase of π , the electrons in ABC TLG behaves as massive fermions with Berry phase of 3π phase. It is expected that ABC TLG is a better electron collimator, compared to single and bilayer graphene. Secondly, as we shown in chapter 6, in the absence of external fields, a charge neutral r-TLG is a LAF with broken time reversal and spin rotation symmetries. We expect that for sufficiently large electric field, all charges reside in either the top or bottom layer, giving rise to a quantum valley Hall(QVH). insulator with broken inversion

symmetry. On the other hand, as parallel magnetic field increases from 0, the competition between the Zeeman and the exchange energies tilts the electron spins, and r-TLG crosses over to the CAF phase. For very large parallel magnetic field, we expect that the electrons eventually form a ferromagnet (F) with counter-propagating edge states and conductance $\sim 6e^2/h$. Another very interesting question is how LAF state evolve in the presence of small but finite density, *e.g.* spin ordered states such as ferromagnetism or anomalous Hall effect may arise. These effects can be explored by coupling ferromagnetic electrodes such as nickel to the device, though technical issues such as stability of nickel in HF and contact between graphene and nickel need to be solved

So far Suspended device structure opens the opportunity to explore the interaction induced many-body physics for the following reasons; 1) post-fabrication current annealing yields extremely clean samples, 2) there is no added scattering from impurity or phonons from the substrate, 3) screening is minimal. However, the suspended graphene structures cannot sustain large gate voltage to reach the high carrier densities, $\sim 10^{13} \text{ cm}^{-2}$, and less amicable to Hall-bar geometry. Recently, successful fabrication of graphene on hexagonal Boron-Nitride (hBN) offers a promising alternative² as the devices are high mobility and can reach high density, high electric field regimes.. Additionally, since hBN and graphene has a small lattice mismatch, a Moire pattern or superlattice potential can be created for charge carriers in graphene, leading to the observation of Hofstadter butterfly spectrum in the quantum Hall regime. These effects are observed in single and bilayer graphene³⁻⁵, but not in TLG. It would be thus

interesting to explore transport properties of TLG in superlattice potential both in zero magnetic field and in the quantum Hall regime.

Reference

- 1 Van Duppen, B., Sena, S. & Peeters, F. Multiband tunneling in trilayer graphene. *Physical Review B* **87**, 195439 (2013).
- 2 Wang, L. *et al.* One-Dimensional Electrical Contact to a Two-Dimensional Material. *Science* **342**, 614-617, doi:10.1126/science.1244358 (2013).
- 3 Hunt, B. *et al.* Massive Dirac Fermions and Hofstadter Butterfly in a van der Waals Heterostructure. *Science* **340**, 1427-1430, doi:10.1126/science.1237240 (2013).
- 4 Dean, C. R. *et al.* Hofstadter's butterfly and the fractal quantum Hall effect in moire superlattices. *Nature* **497**, 598-602 (2013).
- 5 Ponomarenko, L. A. *et al.* Cloning of Dirac fermions in graphene superlattices. *Nature* **497**, 594-597 (2013).

Appendix A

Procedure to clean needle of Oxford fridge

Occasionally the needle valve of the Oxford fridge is blocked during cooling down usually by pump oil vapor that back streams. This usually happens if the helium level in the main bath is low and the mechanical pump pumps on the very good vacuum provided by the cold chamber. The needle valve should be cleaned as below;

1. Unscrew the drive rod completely and carefully remove the needle valve from the insert.
2. Clean the oil from threads on needle using isopropyl alcohol.
3. From the needle valve drive rod guide tube on the insert, pour in loads of isopropyl alcohol to clean the oil from the 1K pot coil. Repeat this procedure a couple of times to ensure all the oil is removed from the 1K pot line.
4. Pour hot water (temperature around 60-70 C) through needle valve drive rod guide tube. Repeat once.
5. Put a rubber bung on needle valve drive rod guide tube. Pump the 1K pot port overnight while heating 1K plate using heat gun or fan heater (temperature 60-70 C) to remove moisture from 1K circuit.
6. Put small layer of VAC grease on needle valve drive rod. Re-assemble the needle valve drive rod



Appendix B

Calculation of density of state and Fermi energy in single, bi- and trilayer graphene.

As shown in Table 1.1, the energy dispersion relations with respect to wave vector of single layer graphene (SLG), (BLG) and rhombohedral-stacked TLG (r-TLG) are simply linear, quadratic and cubic, respectively, in the low-energy approximation. I show the detail calculation process below;

$$H_{\text{mono}} = [\hbar \cdot V_F]k, \quad H_{\text{Bi}} = \frac{\hbar^2 V_F^2 k^2}{\gamma_1}, \quad H_{\text{Tri}} = \frac{\hbar^3 V_F^3 k^3}{\gamma_1^2}. \quad (\text{B-1})$$

The density of state is defined by

$$D(\varepsilon) = \int \frac{d^2k}{(2\pi)^2} \delta(\varepsilon - \varepsilon_k) \quad (\text{B-2})$$

The density of state of SLG is

$$\begin{aligned} D_{\text{SLG}}(\varepsilon) &= g \int \frac{d^2k}{(2\pi)^2} \delta(\varepsilon - \varepsilon_k) \text{ at } \varepsilon_k = [\hbar \cdot V_F]k \text{ and } g = \# \text{ of degeneracy} \\ &= g \int \frac{k dk}{2\pi} \int_0^{2\pi} \frac{d\phi}{2\pi} \delta(\varepsilon - \varepsilon_k) \text{ and let's } \varepsilon_k = u = [\hbar \cdot V_F]k \text{ and } du = [\hbar \cdot V_F]dk \\ &= g \int \frac{u du}{2\pi[\hbar \cdot V_F]^2} \delta(\varepsilon - u) \quad \text{and } g = 4 \quad (\text{B-3}) \end{aligned}$$

$$\text{Therefore } D_{\text{SLG}}(\varepsilon) = 2 \cdot \frac{\varepsilon}{\pi[\hbar \cdot V_F]^2}$$

The density of state of BLG is

$$\begin{aligned} D_{\text{BLG}}(\varepsilon) &= g \int \frac{d^2k}{(2\pi)^2} \delta(\varepsilon - \varepsilon_k) \text{ at } \varepsilon_k = \frac{\hbar^2 V_F^2 k^2}{\gamma_1} \text{ and } g = \# \text{ of degeneracy} \\ &= g \int \frac{k dk}{2\pi} \int_0^{2\pi} \frac{d\phi}{2\pi} \delta(\varepsilon - \varepsilon_k) \text{ and let's } \varepsilon_k = u = \frac{\hbar^2 V_F^2 k^2}{\gamma_1} \text{ and } du = \frac{2\hbar^2 V_F^2}{\gamma_1} k dk \\ &= g \int \frac{\gamma_1 du}{4\pi\hbar^2 V_F^2} \delta(\varepsilon - u) \end{aligned}$$

$$= g \frac{\gamma_1}{4\pi\hbar^2 V_F^2} = \frac{2m}{\pi\hbar^2} \text{ at } m = \gamma_1/2v^2 \text{ and } g=4 \quad (\text{B-4})$$

The density of state of r-ABC TLG is

$$\begin{aligned} D(\varepsilon) &= g \int \frac{d^2k}{(2\pi)^2} \delta(\varepsilon - \varepsilon_k) \text{ at } \varepsilon_k = \frac{\hbar^3 V_F^3 k^3}{\gamma_1^2} \text{ and } g = \# \text{ of degeneracy} \\ &= g \int \frac{k dk}{2\pi} \int_0^{2\pi} \frac{d\phi}{2\pi} \delta(\varepsilon - \varepsilon_k) \text{ and let's } \varepsilon_k = u = \frac{\hbar^3 V_F^3 k^3}{\gamma_1^2} \text{ and } du = \frac{3\hbar^3 V_F^3 k^2}{\gamma_1^2} k^2 dk \\ &= g \int \frac{u^{-1/3} du}{6\pi a^{2/3}} \delta(\varepsilon - u) \text{ with } a = \frac{\hbar^3 V_F^3}{\gamma_1^2} \\ &= g \frac{\varepsilon^{-1/3}}{6\pi a^{2/3}} = \frac{2\gamma_1^{4/3}}{3\pi(\hbar V_F)^2} \cdot \varepsilon^{-1/3} \text{ at } g=4 \end{aligned} \quad (\text{B-5})$$

Finally from the relation between charge carrier density and the density of state, we can get the Fermi energy as a function of charge carrier density.

$$n = \frac{N}{A} = \int_0^{\varepsilon_f} D(\varepsilon) d\varepsilon \quad (\text{B-6})$$

Fermi energy of SLG is

$$\begin{aligned} n &= \int_0^{\varepsilon_f} D(\varepsilon) d\varepsilon = \int_0^{\varepsilon_f} 2 \cdot \frac{\varepsilon}{\pi[\hbar \cdot V_F]^2} d\varepsilon \text{ at } D(\varepsilon) = 2 \cdot \frac{\varepsilon}{\pi[\hbar \cdot V_F]^2} \\ &= \frac{\varepsilon_f^2}{\pi[\hbar \cdot V_F]^2} \end{aligned}$$

$$\varepsilon_f = \hbar \cdot V_F \sqrt{n\pi}. \quad (\text{B-7})$$

Fermi energy of bilayer graphene is

$$\begin{aligned} n &= \int_0^{\varepsilon_f} D(\varepsilon) d\varepsilon = \int_0^{\varepsilon_f} \frac{2m}{\pi\hbar^2} d\varepsilon \text{ at } D(\varepsilon) = \frac{2m}{\pi\hbar^2} \\ &= \frac{2m}{\pi\hbar^2} \varepsilon_f \end{aligned}$$

$$\varepsilon_F = \frac{\pi \hbar^2}{2m} \cdot n. \quad (\text{B-7})$$

Finally Fermi energy of r-trilayer graphene is

$$\begin{aligned} n &= \int_0^{\varepsilon_f} D(\varepsilon) d\varepsilon = \int_0^{\varepsilon_f} \frac{2\gamma_1^{4/3}}{3\pi(\hbar V_F)^2} \cdot \varepsilon^{-1/3} d\varepsilon \quad \text{at } D(\varepsilon) = \frac{2\gamma_1^{4/3}}{3\pi(\hbar V_F)^2} \cdot \varepsilon^{-1/3} \\ &= \frac{\gamma_1^{4/3}}{\pi(\hbar V_F)^2} \cdot \varepsilon_F^{2/3} \\ \varepsilon_F &= \frac{(\hbar V_F)^3}{\gamma_1^2} (n\pi)^{3/2} \quad (\text{B-8}) \end{aligned}$$

Appendix C

Current annealing summary table

Device Name	Fridge	# of layer	Length (μm)	Width (μm)	Mobility (cm^2/Vs)	I (mA)	I (mA)/(μm)	I (mA/ $\mu\text{m}/\text{layer}$)
ySGT6	Oxford	2	1.33	0.75	15,000	0.55	0.73	0.36
ySGT45	Oxford	3	1.266	1.67	50,000	1.72	1.02	0.34
ySGT12	Oxford	3	1.3	1.6	4,600	1.6	1	0.33
ySGT35	SCM	3	1.3	1.7	6,000	1.15	0.67	0.22
ySGT571	SCM	3	1.182	0.86	15,000	1.67	1.94	0.64
ySGT84	SCM	3	1.066	0.859	55,000	1.35	1.57	0.52
ySGT85	SCM	3	1.1	1.069	7,000	1.16	1.08	0.36
ySGT86	SCM	3	1.13	1.74	6,600	1.85	1.06	0.35
SGT95	SCM	3	1.32	1.392	20,000	1.53	1.09	0.36
SGT97	SCM	3	1.32	1.62	30,000	1.7	1.04	0.34
ySGT97t	SCM	3	1.1	1.13	40,000	1.37	1.21	0.40
ySGT97b	SCM	3	1.06	1.489	50,000	2.39	1.60	0.53
kSGT15	Cell9	3	1.126	1.169	40,000	1.67	1.42	0.47
kSGT16	Cell9	3	1	1	48,000	1.75	1.75	0.58
ySGT106	Cell9	3	1.1	1.74	90,000	2.33	1.3	0.44
ySGT126	Cell9	3	1.1	2.07	8,000	2.61	1.26	0.42
ySGT127	Cell9	4	1.1	2.1		3.75	1.786	0.44
ySGT2	Cell9	2	1.3	2	20,000	1.42	0.71	0.35
ySGT44	Cell9	3	1.3	1.4	45,000	1.2	0.85	0.28

KSGB 6a	Janis	2	1.09	1.55	15,000	1.1	0.70	0.35
ySGT9 5	Janis	3	1.12	1.16	35,000	1.88	1.62	0.54
ySGT9 0	Janis	3	1.07	3.342	60,000	3.5	1.04	0.34
ySGT7 2	Janis	3	1.218	1.578	40,000	1.75	1.10	0.36